

Prediction of Fatigue Crack Growth and Damage Directionality in Non-Conventional Fibre Metal Laminates

MSc Thesis

R.F.H. van Maris

Technische Universiteit Delft

Prediction of Fatigue Crack Growth and Damage Directionality in Non-Conventional Fibre Metal Laminates

MSc Thesis

by

R.F.H. van Maris

to obtain the degree of Master of Science
at the Delft University of Technology,
to be defended publicly on Friday July 19, 2019 at 09:30 AM.

Student number: 4229304
Project duration: January 7, 2019 – July 19, 2019
Thesis committee: Dr. ir. R.C. Alderliesten TU Delft, supervisor
Ir. J. Sinke TU Delft, additional member
Dr. B. Chen TU Delft, external member

An electronic version of this thesis is available at <http://repository.tudelft.nl/>.

Preface

This report presents the research performed during my master thesis and concludes the last step before obtaining the degree Master of Science at the faculty of Aerospace Engineering at Delft University of Technology. The research described in this thesis is preceded by a literature study [1] from which the most relevant parts are repeated in Chapter 2, making this thesis a stand-alone document.

This thesis topic appealed to me due to my interest in fatigue and damage tolerance of fibre metal laminates which originated during my internship at Airbus. However, being interested into a subject is as equally important as having a good supervisor. I would like to take this opportunity to thank my supervisor, René Alderliesten, for his guidance throughout the past 10 months. Your knowledge and advice provided me a lot of insights and understanding of the subject matter. Moreover, I appreciated that you always made time for my questions.

This thesis provided me the opportunity to design, manufacture and test my own specimens which gave me practical insights; something you can only gain by doing it yourself. I could not have done this without the support from the technicians at the Delft Aerospace Structures and Materials Laboratory. In particular a thank you to Cees Paalvast, Gertjan Mulder, Berthil Grashof and Johan Boender.

Finishing my master marks the end of my life as a student which has been a great experience due to the people I met along the way. I would like to thank you all for the great memories. Finally, I would like to thank my friends and family for always supporting me and providing me with advice when most needed.

*R.F.H. van Maris
Delft, July 8, 2019*

Summary

This thesis presents a model that is able to predict fatigue crack growth and damage directionality in non-conventional Fibre Metal Laminates (FMLs) in Centre-Cracked Tension (CCT) specimens. Non-conventional FMLs encompass all FMLs other than standardised ones such as GLARE. FMLs can be made non-conventional by using multiple fibre types, any fibre orientation, multiple alloy types or thicknesses, or a combination thereof. These characteristics provide much more tailorability than standardised FMLs and thereby extend the applicability of FMLs to, for example, door corner reinforcements [2] and wing structures [3]. Contrary to standardised FMLs, the damage in non-conventional FMLs is non-uniform, necessitating the ability to compute the crack growth rate in the metal layers and the delamination at the metal-fibre interfaces separately.

One of the greatest assets of FMLs is known as fibre bridging, which lowers the stress intensity at the crack tip and slows down the crack growth as a result. In order to compute the fibre bridging stress, compatibility at each metal-fibre interface is enforced at the delamination boundary. Since fibres can have an arbitrary orientation in non-conventional FMLs, compatibility is enforced in longitudinal and in transverse direction in order to compute the bridging stress in longitudinal and transverse direction, respectively. The longitudinal fibre bridging component restrains a mode I crack from opening further, while the transverse fibre bridging component does the same for a mode II crack.

The mode I and mode II stress intensity factors are treated independently and are used as input for the computation of the fracture angle (the angle between the horizontal and the crack; hence damage directionality). Combining the two stress intensity factors facilitates the computation of the crack growth rate by making use of the Paris relation. In addition to crack growth, the delamination grows as well and is determined using the strain energy release rate.

The model works with an iterative process, meaning that the damage parameters calculated in one iteration are used as inputs for the next iteration. By setting a small maximum crack and delamination extension per iteration, the output becomes more accurate. However, the total computational time increases then as well.

The model has been verified by comparing the outcome of a standardised FML (GLARE) with the outcome of a model built for the prediction of fatigue crack growth in such laminates. In addition to comparing legacy test data with the model's prediction, validation is done by performing tests which included unbalanced laminates, asymmetric laminates and constant and variable amplitude loading. In general, the model's prediction and tests show a good resemblance.

The model, as presented in this thesis, provides a good estimate concerning the fatigue crack growth and the fracture angle within a relatively short computational time. Other advantages are (1) the derivation from first principles of mechanics such that correction factors are omitted and (2) its modularity, which accommodates the model to be extended to other crack configurations or coupled to other modules that calculate fatigue crack initiation or residual strength for example.

Contents

Preface	iii
Summary	v
List of Figures	ix
List of Tables	xiii
List of Symbols	xv
List of Abbreviations	xvii
1 Introduction	1
2 Fibre Metal Laminates	3
2.1 Concept and Development	3
2.2 Standardised FMLs and Current Use	5
2.3 Future Applications	6
2.4 Current Fatigue Crack Growth Models	6
2.4.1 Model of Alderliesten	7
2.4.2 Model of Wilson	9
2.4.3 Model of Khan	10
2.4.4 Model of Spronk	11
2.4.5 Model of Gupta	12
2.4.6 Models' Overview	13
2.5 Research Goal	14
3 Model	15
3.1 Model Overview	15
3.1.1 Definitions and Conventions	15
3.1.2 Model Assumptions	16
3.1.3 Model Flow Diagram	17
3.2 Inputs and Initialisation	18
3.2.1 Model Inputs	18
3.2.2 Classical Laminate Theory	19
3.2.3 Induced Shear Stress	19
3.2.4 Discretisation	20
3.2.5 Initialisation	21
3.3 Bridging Load Determination	22
3.3.1 Longitudinal Fibre Bridging Component	22
3.3.2 Transverse Fibre Bridging Component	26
3.3.3 Bridging Angle	29
3.4 Strain Energy Release Rate	29
3.5 Damage Growth	30
3.5.1 Crack Growth	30
3.5.2 Delamination Growth	32
3.6 Fracture Angle	32
3.7 Differences between CA and VA Loading	33
3.7.1 Assumptions	33
3.7.2 Inputs	33
3.7.3 Computations	33
3.7.4 Flow Diagram	35

4	Testing and Results	37
4.1	Design of Test	37
4.1.1	Fracture Angle	37
4.1.2	Variable Amplitude Loading	38
4.1.3	Unbalanced and Asymmetric Laminates	38
4.2	Laminate Manufacturing	39
4.3	Test Set-Up	39
4.4	Post-Test Inspection	41
4.5	Results	41
4.5.1	Test 1 & 2	41
4.5.2	Test 3	42
4.5.3	Test 4 & 5	43
4.5.4	Test 6	45
5	Verification and Validation	47
5.1	Verification	47
5.1.1	Unit Tests	47
5.1.2	System Tests	47
5.2	Validation	49
5.2.1	Legacy Test Data	49
5.2.2	Current Test Data	56
6	Discussion	61
6.1	Model Discussion	61
6.2	Limit of Validity	62
6.2.1	Laminate	62
6.2.2	Initial Damage Size	62
6.2.3	Loading	62
6.3	Practical Use of Model	63
6.3.1	Convergence	63
6.3.2	Computational Parameters	64
6.3.3	Shortcomings	65
6.4	Extensibility	65
6.4.1	Fatigue Crack Initiation	65
6.4.2	Residual Strength	65
6.4.3	Crack Configurations	66
6.4.4	Fracture Angle	66
6.4.5	Applied Shear Stress	66
6.4.6	Smearred Properties	66
7	Conclusions and Recommendations	67
7.1	Conclusions	67
7.2	Recommendations	67
	Bibliography	69
A	Test Reports	73
B	Additional Validation on Gonesh Data	79
B.1	Gonesh Data References	79
B.2	Initial Notch Size	80
B.3	GLARE 3 and GLARE 4B - Other Angles	80
C	Metal Laminates	81

List of Figures

2.1	Example of a fibre metal laminate	3
2.2	The principle of fibre bridging; (a) fatigue through crack, (b) surface crack	4
2.3	Comparison between the crack growth curves of Al2024-T3 and GLARE 3 and 4B	4
2.4	Equal delamination discretisation	8
2.5	Effect of an overload on the crack length	11
2.6	Schematic stress distribution and plastic zone formation at the crack tip after an overload	11
2.7	The concept of superpositioning the different SIFs	12
2.8	Overview analytical models related to FCI, FCP and damage directionality	13
3.1	Model coordinate system	16
3.2	Fracture modes: (I) opening; (II) in-plane shear; (III) transverse shear	16
3.3	Model flow diagram for constant amplitude loading	18
3.4	Tension-shear coupling in unbalanced laminates under the effect of (a) free ends and (b) clamped ends	20
3.5	Biased delamination discretisation using a Chebyshev distribution	21
3.6	Idealisation of shear into bridging stress at the delamination boundary	24
3.7	Segment definition at a given bar element	24
3.8	Contribution of a metal layer with a smaller crack to the bridging material of a metal layer with a larger crack (fibre layer in between is not shown for clarity)	25
3.9	Visualisation of the actual damage growth (orange) and the modelled damage growth (blue). Dimensions are for illustration purposes.	32
3.10	Plastic zone sizes used in YZ model	34
3.11	Coordinate and parameter definition ahead of the crack tip	34
3.12	Model flow diagram for variable amplitude loading	36
4.1	Test specimen geometry (all dimension in mm)	39
4.2	Test set-up (front view)	40
4.3	Test set-up sketch (top view)	40
4.4	Different steps in specimen preparation for DIC	40
4.5	Crack length definitions	41
4.6	Test 1 crack size and orientation after 250 kcycles (blue arrows indicate crack tip)	42
4.7	Test 1 crack growth data of specimen front side	42
4.8	Test 2 crack size and orientation after 28 kcycles	42
4.9	Test 2 crack growth data of specimen front and rear side	42
4.10	Test 3 crack size and orientation after 200 kcycles	43
4.11	Test 3 crack growth data of specimen front and rear side	43
4.12	Test 3 strain field in longitudinal direction after 200 kcycles	43
4.13	Test 3 delamination contour after 200 kcycles (front side after etching)	43
4.14	Test 4 crack size and orientation after 250 kcycles	44
4.15	Test 5 crack size and orientation after 160 kcycles	44
4.16	Test 4 strain field in longitudinal direction after 250 kcycles	44
4.17	Test 5 strain field in longitudinal direction after 160 kcycles	44
4.18	Test 4 delamination contour after 250 kcycles (front side after etching)	44
4.19	Test 5 delamination contour after 160 kcycles (front side after etching)	44
4.20	Test 4 and 5 crack growth data of specimen front and rear side	45
4.21	Test 6 crack size and orientation after 250 kcycles (front side)	45
4.22	Test 6 crack size and orientation after 250 kcycles (rear side)	45
4.23	Test 6 strain field in longitudinal direction after 250 kcycles	46
4.24	Test 6 delamination contour after 250 kcycles (front side after etching)	46

4.25 Test 6 crack growth data of specimen front and rear side	46
5.1 Crack growth rate prediction of the original model for GLARE 2A-4/3-0.4 under $S_{max} = 100$ MPa and $R = 0.05$ at $OAA = 0^\circ$	48
5.2 Crack growth rate prediction of the modified model for GLARE 2A-4/3-0.4 under $S_{max} = 100$ MPa and $R = 0.05$ at $OAA = 0^\circ$	48
5.3 Crack growth rate prediction of the original model for GLARE 4B-4/3-0.4 under $S_{max} = 100$ MPa and $R = 0.05$ at $OAA = 0^\circ$	48
5.4 Crack growth rate prediction of the modified model for GLARE 4B-4/3-0.4 under $S_{max} = 100$ MPa and $R = 0.05$ at $OAA = 0^\circ$	48
5.5 Fracture angle comparison between test data and prediction for GLARE 3-4/3-0.4	49
5.6 Fracture angle comparison between test data and prediction for GLARE 4B-4/3-0.4	50
5.7 Fracture angle comparison between test data and prediction for GLARE 2A-4/3-0.4	50
5.8 Specimen geometry tested by Gonesh	51
5.9 Comparison between crack growth test data and crack growth prediction for GLARE 3-4/3-0.4 at $OAA = 45^\circ$	51
5.10 Comparison between crack growth rate test data and crack growth rate prediction for GLARE 3-4/3-0.4 at $OAA = 45^\circ$	51
5.11 Comparison between crack growth test data and crack growth prediction for GLARE 4B-4/3-0.4 at $OAA = 45^\circ$	52
5.12 Comparison between crack growth rate test data and crack growth rate prediction for GLARE 4B-4/3-0.4 at $OAA = 45^\circ$	52
5.13 Comparison between crack growth test data and crack growth prediction for GLARE 5-4/3-0.4 at $OAA = 45^\circ$	52
5.14 Comparison between crack growth rate test data and crack growth rate prediction for GLARE 5-4/3-0.4 at $OAA = 45^\circ$	52
5.15 Comparison between crack growth test data and different methods to predict crack growth for GLARE 2A-4/3-0.4 under $S_{max} = 120$ MPa and $R = 0.05$ at $OAA = 45^\circ$	53
5.16 Delamination around the crack of a GLARE 2A specimen under $S_{max} = 140$ MPa and $R = 0.05$ at $OAA = 45^\circ$	53
5.17 Comparison between crack growth test data and crack growth prediction for GLARE 2A-4/3-0.4 at $OAA = 45^\circ$	53
5.18 Comparison between crack growth test data and crack growth prediction for GLARE 2A-4/3-0.4 under $S_{max} = 100$ MPa and $R = 0.05$ at $OAA = 22.5^\circ$	53
5.19 Comparison between crack growth test data and crack growth prediction for AI-4/0-0.4 under $S_{max} = 100$ MPa and $R = 0.05$	54
5.20 The specimen lay-ups used by Rensma	54
5.21 Comparison between crack growth rate test data and crack growth rate prediction (laminates A and B-T700)	55
5.22 Comparison between crack growth rate test data and crack growth rate prediction (laminates B-T800 and D)	55
5.23 Comparison between crack growth rate test data and crack growth rate prediction (laminates C and C2)	56
5.24 Comparison between crack growth rate test data and crack growth rate prediction (laminates E and E2)	56
5.25 Delamination indicated in red for all interfaces in specimen C after 64 kcycles	56
5.26 Crack growth comparison between test 1 data and prediction	57
5.27 Crack growth comparison between test 2 data and prediction	57
5.28 Crack growth comparison between test 3 data and prediction	58
5.29 Delamination comparison between test 3 data and prediction	58
5.30 Crack growth comparison between test 4 data and prediction	58
5.31 Crack growth comparison between test 5 data and prediction	58
5.32 Delamination comparison between test 4 data and prediction	59
5.33 Delamination comparison between test 5 data and prediction	59
5.34 Crack growth comparison between test 6 data and prediction	60
5.35 Delamination comparison between test 6 data and prediction (front side)	60

5.36 Delaminations test specimen 6	60
6.1 Crack growth prediction for GLARE 3-4/3-0.4 under $S_{max} = 100$ MPa and $R = 0.05$ at $OAA = 45^\circ$ for various mesh sizes	63
6.2 Crack growth rate prediction for GLARE 3-4/3-0.4 under $S_{max} = 100$ MPa and $R = 0.05$ at $OAA = 45^\circ$ for various mesh sizes	63
6.3 Fracture angle prediction for GLARE 3-4/3-0.4 under $S_{max} = 100$ MPa and $R = 0.05$ at $OAA = 45^\circ$ for various mesh sizes	64
6.4 Crack growth prediction for Laminate 1 under $S_{max} = 140$ MPa and $R = 0.05$ at $OAA = 0^\circ$ for various mesh sizes	64
6.5 Crack growth prediction for Laminate 2 under $S_{max} = 140$ MPa and $R = 0.05$ at $OAA = 0^\circ$ for various mesh sizes	64
B.1 Comparison between crack growth test data and crack growth prediction for GLARE 3-4/3-0.4 under $S_{max} = 100$ MPa and $R = 0.05$ at $OAA = 45^\circ$	80
B.2 Comparison between crack growth test data and crack growth prediction for GLARE 4B-4/3-0.4 under $S_{max} = 80$ MPa and $R = 0.05$ at $OAA = 45^\circ$	80
B.3 Comparison between crack growth test data and crack growth prediction for GLARE 3-4/3-0.4 under $S_{max} = 100$ MPa and $R = 0.05$ at $OAA = 22.5^\circ$	80
B.4 Comparison between crack growth test data and crack growth prediction for GLARE 3-4/3-0.4 under $S_{max} = 140$ MPa and $R = 0.05$ at $OAA = 35^\circ$	80
B.5 Comparison between crack growth test data and crack growth prediction for GLARE 4B-4/3-0.4 under $S_{max} = 100$ MPa and $R = 0.05$	80
B.6 Comparison between crack growth test data and crack growth prediction for GLARE 4B-4/3-0.4 under $S_{max} = 140$ MPa and $R = 0.05$ at $OAA = 35^\circ$	80

List of Tables

2.1	Standardised ARALL and GLARE grades	5
3.1	Required model inputs	19
4.1	Geometrical and loading parameters of test specimens	37
4.2	Overview relating (legacy) test data to the characteristics of non-conventional FMLs	38
4.3	Measured fracture angles of test specimens	41
5.1	Input system test verification	48
5.2	Fracture angle comparison between data from test 1 and 2 test and prediction	57
5.3	Fracture angle comparison between data from test 3 test and prediction	58
5.4	Fracture angle comparison between data from test 4 and 5 test and prediction	59
5.5	Fracture angle comparison between data from test 6 test and prediction	60
6.1	Mesh size comparison for GLARE 3-4/3-0.4 under $S_{max} = 100$ MPa and $R = 0.05$ at $OAA = 45^\circ$	64
B.1	Gonesh data reference	79
C.1	Model comparison for various laminate configurations	81

List of Symbols

Symbol	Unit	Description
a	[mm]	Half crack length
a_0	[mm]	Half starter crack length
a_i	[mm]	Transition half crack length
b	[mm]	Half delamination length
C_b	[-]	Correction for shear deformation of small delamination lengths
C_{br}	[1/MPa]	Fibre bridging compliance
C_{cg}	[mm · (MPa√mm) ^{-n_{cg}}]	Paris constant in crack growth relation
C_d	[mm · (MPa√mm) ^{-n_d}]	Paris constant in delamination growth relation
C_P	[-]	Constant in the yield zone model
C_u	[1/MPa]	Transverse bridging displacement compliance
C_v	[1/MPa]	Longitudinal bridging displacement compliance
C_τ	[1/MPa]	Shear compliance
da/dN	[mm/cycle]	Crack growth rate
db/dN	[mm/cycle]	Delamination growth rate
E	[MPa]	Modulus of elasticity
F_{br}	[N/mm]	Bridging load
F^d	[MPa · mm]	Work
G_d	[MPa · mm]	Strain energy release rate for delamination
G	[MPa]	Shear modulus
K	[MPa√mm]	Stress intensity factor
L	[mm]	Specimen length
M	[N]	Line moment
m	[-]	Wheeler exponent
N	[N/mm]	Line load
n	[-]	Number of layers
n_{cg}	[-]	Paris constant in crack growth relation
n_d	[-]	Paris constant in delamination growth relation
P	[N]	Unit point load in longitudinal direction
Q	[N]	Unit point load in transverse direction
R_K	[-]	Ratio between the minimum and maximum SIF at the crack tip
r_p	[mm]	Radius plastic zone (elastic-plastic stress redistribution)
r_y	[mm]	Radius plastic zone (elastic stress distribution)
S	[MPa]	Stress
s	[mm]	Half saw-cut length
T	[°]	Temperature
t	[mm]	Thickness
u	[mm]	Crack opening in transverse direction
U^d	[MPa · mm]	Strain energy
v	[mm]	Crack opening in longitudinal direction
W	[mm]	Specimen width

w	[mm]	Bar element width
x	[mm]	Coordinate parameter
x_p	[mm]	Location of point load P
y	[mm]	Coordinate parameter
z	[mm]	Coordinate parameter
Δb_S	[mm]	Height of bridging segment S
δ	[mm]	Displacement
ϵ	[-]	Strain
θ	[°]	Ply orientation angle
θ_{br}	[°]	Bridging angle
κ	[1/mm]	Curvature
ν	[-]	Poisson ratio
σ	[MPa]	Stress
σ_Y	[MPa]	Yield stress
τ	[MPa]	Shear stress
Φ	[°]	Fracture angle

Subscript	Description
<i>al</i>	aluminium
<i>bot</i>	below
<i>br</i>	bridging
<i>cur</i>	curing
<i>eff</i>	effective
<i>f</i>	fibre
<i>int</i>	internal
<i>max</i>	maximum
<i>min</i>	minimum
<i>OL</i>	overload
<i>pp</i>	prepreg
<i>tip</i>	at the crack tip
<i>top</i>	above
<i>x</i>	in x-direction
<i>y</i>	in y-direction
0	location of point load
I	Mode I
II	Mode II
∞	far field

List of Abbreviations

Abbreviation	Description
ARALL	Aramid Reinforced ALuminium Laminate
CA	Constant Amplitude
CC	Crack Closure
CCT	Centre Cracked Tension
CLT	Classical Laminate Theory
CORPUS	Computation Of Retarded Propagation Under Spectrum loading
CTE	Coefficient of Thermal Expansion
DASML	Delft Aerospace Structures and Materials Laboratory
DENT	Double-Edge-Notched Tension
DIC	Digital Image Correlation
FCI	Fatigue Crack Initiation
FCP	Fatigue Crack Propagation
FEM	Finite Element Method
FML	Fibre Metal Laminate
FWCF	Finite Width Correction Factor
GLARE	GLAss REinforced aluminium
LDA	Linear Damage Accumulation
LEFM	Linear Elastic Fracture Mechanics
ML	Metal Laminate
NA	Neutral Axis
NLM	Neutral Line Model
OAA	Off-Axis Angle
POV	Point Of View
RS	Residual Strength
SERR	Strain Energy Release Rate
SIF	Stress Intensity Factor
UD	Uni-Directional
VA	Variable Amplitude
YZ	Yield Zone

Introduction

Fibre Metal Laminates (FMLs) are developed as a structural material concept at Delft University of Technology by the faculty of Aerospace Engineering in collaboration with partners as, amongst others, Airbus. Development of this new material concept started in the 1970's and reached an important milestone in 2005 through the application as a skin material on the Airbus A380 fuselage [4]. The type of FML used on the A380, GLARE, is known for its superior fatigue and damage tolerant behaviour compared to monolithic metal.

Due to the lower and nearly constant crack growth rates of FMLs, Airbus is currently looking into designing door corner reinforcements (doublers) with this material in several aircraft of their fleet [2]. Next to Airbus, Embraer¹ recently manufactured and tested an FML demonstrator panel for the lower wing cover. For both concepts tailorability of the material is desired and can be provided by multiple fibre types, any fibre orientation, multiple alloy types or thicknesses, or a combination thereof. An FML where such tailorability is possible, thereby deviating from the standardised FMLs, is called a non-conventional FML.

In analogy to the life of a monolithic metal structure, the life of an FML structure can be divided into two different phases: Fatigue Crack Initiation (FCI) and Fatigue Crack Propagation (FCP). The research in this thesis is focused on FCP and both on the crack growth rate as on the direction in which the cracks grow to be more precise. The research performed on FCP in FMLs until date can be placed into three categories: models based on either a phenomenological approach, an analytical² approach or Finite Element Method (FEM). The phenomenological models, which are mostly developed for dedicated GLARE grades, are due to their simplistic approach not suitable for non-conventional FMLs [5]. Models based on FEM are impractical during design studies when results need to be obtained quickly. Pre-processing activities, such as meshing and the long computational time are two obstacles in providing a quick answer. Due to their wide applicability, the analytical models, based on failure mechanisms and sequences in order to provide an accurate prediction, are preferred over the other approaches.

Various analytical models have been developed, with each model focusing on different aspects. Two models in particular, one which is able to predict the fatigue crack growth rate for each metal layer separately in FMLs with varying metal thicknesses, and the other, which is able to calculate the direction the crack grows to for FMLs with arbitrary fibre orientations, are presumed to contain the elements for creating a model, capable of predicting fatigue crack growth and damage directionality in non-conventional FMLs. Since the purposes of the two aforementioned models are different (crack growth against damage directionality) and the two models need to be combined, the following question is raised:

How to predict the fatigue crack growth rate and damage directionality for non-conventional FMLs?

¹D.F.N.R. da Silva. Embraer: Manufacturing of a Fiber Metal Laminate Lower Wing Cover Demonstrator, FML Outlook: Nov 2 – 3, 2017 Delft, The Netherlands (<https://www.tudelft.nl/en/ae/fml-outlook/speakers/20412/>) - Consulted on 05/11/18

²Phenomenological approaches are strictly speaking also analytical. However, the term *analytical approach* is often used in literature for approaches which are based on first principles of mechanics.

This report is structured as follows: Chapter 2 provides a brief overview of relevant literature concerning fibre metal laminates, ending with detailed research questions arising from the literature review. In Chapter 3 the model to predict fatigue crack growth and its directionality is outlined in detail. In order to find the limits of the model's predicting capabilities, six tests are performed which are described in Chapter 4. Model verification and validation, both on the test data presented in Chapter 4 as on legacy test data, is discussed in Chapter 5. The functionality of the model and its operational limits are outlined in Chapter 6. Finally, in Chapter 7, conclusions are presented and recommendations are made for future research.

2

Fibre Metal Laminates

Fibre metal laminates went through an entire development process, from first bonding metal sheets together till the current-day application of GLARE (a standardised FML) in the fuselage skin of the Airbus A380 [4]. In this chapter the development of FMLs (Section 2.1), the different types and current applications (Section 2.2), as well as future applications (Section 2.3) are described. The different models developed to predict fatigue crack growth are discussed in Section 2.4, where the limits of these models are highlighted as well. Finally, the research goals for this thesis are presented in Section 2.5.

2.1. Concept and Development

The origins of fibre metal laminates lie at De Havilland, the first aircraft manufacturer to bond metal parts [4]. These bonded metal sheets are known as Metal Laminates (MLs). Next to the cost advantage, MLs have superior damage tolerant behaviour in comparison to monolithic sheet metal. Schijve et al. [6] observed that crack growth in MLs is slower than in its monolithic counterpart due to the delayed crack propagation through the thickness provided by the adhesive layers, resulting in the restraint of crack opening by the remaining uncracked metal layers [7].

Over the years more research has been performed on this topic, both on bonding metal sheets together, as on laminates where fibres are embedded in the adhesive [4]. The latter instance, where fibres are embedded in the adhesive, is referred to as fibre metal laminates of which an example is depicted in Figure 2.1. Characteristics, such as the number of layers, the materials, the layers' thicknesses, the stacking sequence and the fibre orientation provide the ability to tailor the structure. Non-conventional FMLs are defined as FMLs which contain multiple fibre types, any fibre orientation, multiple alloy types or thicknesses, or a combination thereof.

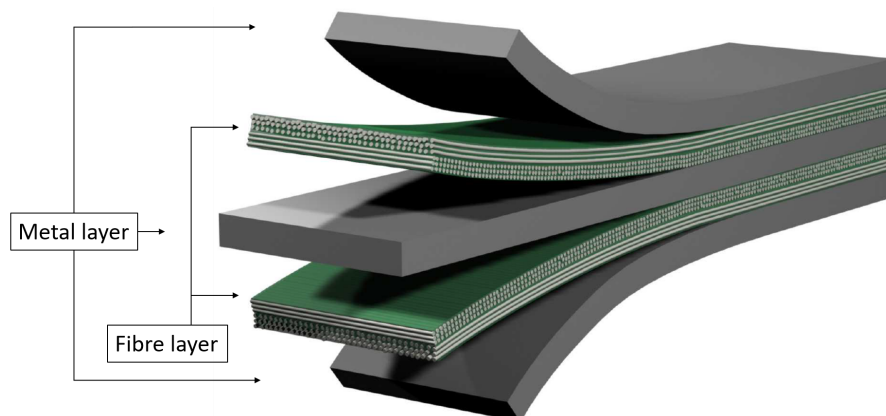


Figure 2.1: Example of a fibre metal laminate [8]

A considerable advantage of an FML over a ML, is the fibre bridging mechanism, which is observed in FMLs if a crack is present in one or more metal layers [9–11]. Loads can still be transferred through the fibres and thereby limit the crack opening in the metal layer as shown in Figure 2.2. This yields a lower Stress Intensity Factor (SIF) at the crack tip of the metal layer [12].

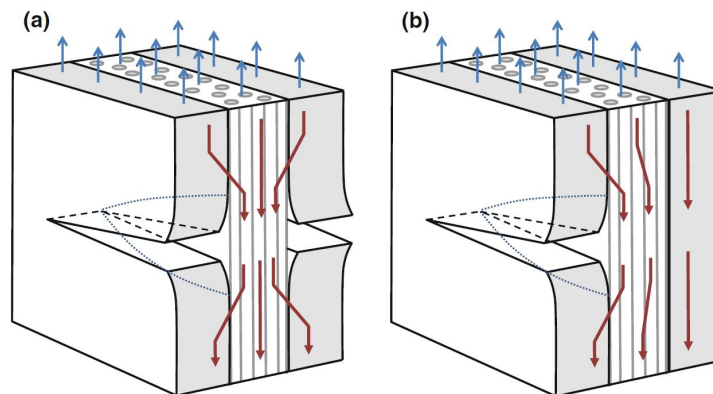


Figure 2.2: The principle of fibre bridging; (a) fatigue through crack, (b) surface crack [9]

The crack growth observed in FMLs is different from monolithic metals due to fibre bridging. Instead of an exponential-like crack growth, a constant growth is observed as depicted in Figure 2.3 [4]. One requirement for fibre bridging to work is the presence of delamination around the crack [12]. This may seem counterintuitive since delaminations in composites are undesirable; however, for FMLs delamination around the crack is beneficial for the following reason: in the occurrence of a crack, the adjacent fibres locally elongate due to crack opening. If the cracked metal layer and the fibre layer are delaminated, the elongation of the fibres around the crack is distributed over a longer length compared to when no delamination is present. Hence, the strain in the fibres is less and the failure strain is not exceeded. However, if large delaminations are present, the elongation is distributed over an even longer distance, reducing the strain further resulting in a reduction of the bridging stress and thus an increase in the stress intensity at the crack tip [12]. Hence, delaminations are beneficial only within certain limits.

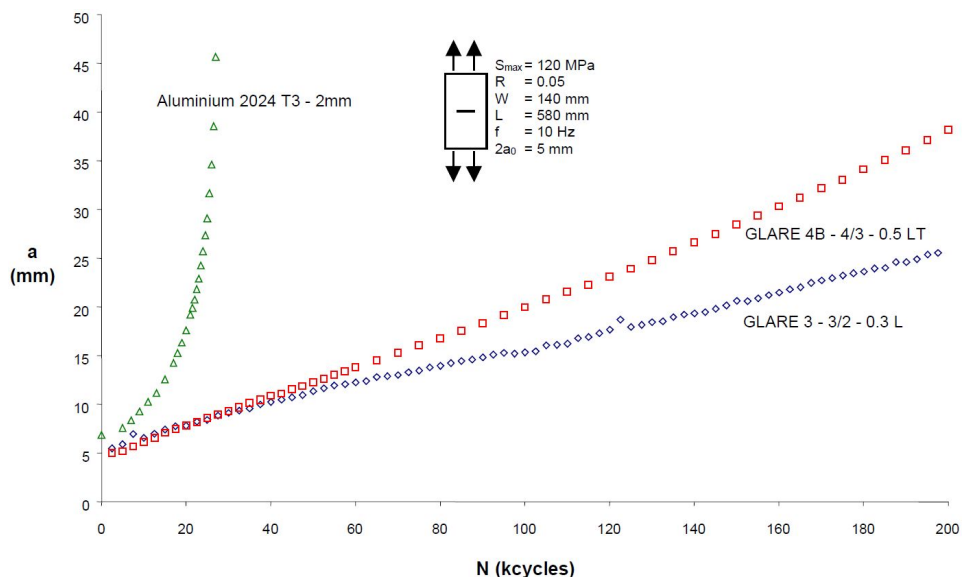


Figure 2.3: Comparison between the crack growth curves of Al2024-T3 and GLARE 3 and 4B [4]

In addition to the superior fatigue characteristics, other properties are enhanced as well. Firstly, the laminated prepreg and metal layers respectively act as a barrier against corrosion and moisture absorption [4]. Secondly, in case of a fire, the different layers delaminate and thereby create an insulating layer which results in a higher fire resistance [4]. Lastly, composites are favourable for their ability to

tailor the properties; however, damage caused by impact is difficult to detect. Tailoring the material is possible with FMLs, as well as detecting impact damage due to dents in the metal sheets [4]. Although it can not be regarded as a general rule, these examples suggest that FMLs combine the advantages of metal and composites structures [4].

2.2. Standardised FMLs and Current Use

FMLs can have numerous compositions with metal and fibre layers; however, some FMLs have been standardised. The first developed FML to have been certified for aerospace applications was ARALL (Aramid Reinforced ALuminium LAMinate). Several wing hatches and access holes of the Fokker 50 were made of this material. Due to the high manufacturing costs (8-10 times more expensive than aluminium) and the unsatisfying fatigue properties, it was never used in the large structures it was originally designed for (e.g. lower wing panels) [4, 9]. It is peculiar that ARALL has poor fatigue properties as FMLs are developed for their damage tolerance. The problem with ARALL is that, under a small or negative stress ratio, the fibres fail due to the compressive instability of aramid together with the adhesion characteristics between fibre and epoxy [9].

To overcome these poor fatigue properties, the development of GLARE (GLASS REinforced aluminium) was initiated. This FML type contains S2 glass fibres instead of aramid fibres [4]. With the interest of both Boeing and Airbus, GLARE was further developed to a viable product and is currently used, amongst others, as fuselage skin panels on the Airbus A380 and frame flange straps on the Airbus A400M [4, 9, 13]. The implementation of GLARE in a primary structural element was preceded by a long development process, existing of many small development steps and applications in secondary structures as is traditionally done with new materials in order to broaden the knowledge about the material and evaluate it in a real life, aerospace application [7, 14]. If results are promising, as has been the case for GLARE, it can be used in primary structures.

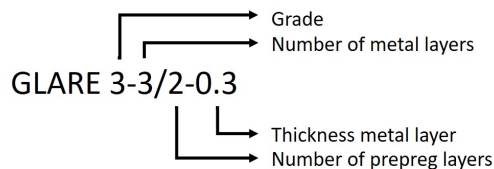
The standardised grades of ARALL and GLARE, listed in Table 2.1, were developed with each grade having its own benefits [4]. It must be noted that the earlier discussed ability to tailor the material is limited in these grades since only Uni-Directional (UD) fibres or cross-ply are used. Additionally, only one type of alloy with a constant thickness is used in combination with a single fibre type. This shows that the possibilities of FMLs have not yet been fully exploited.

Table 2.1: Standardised ARALL and GLARE grades [4, 9, 14]

Grade	Aluminium Alloy	Thickness metal [mm]	Orientation fibres [°]	Epoxy	Main benefits
ARALL-1	7075-T6	0.3	0/0	AF163-2	Fatigue, strength
ARALL-2	2024-T3	0.3	0/0	AF163-2	Fatigue, formability
ARALL-3	7475-T761	0.3	0/0	AF163-2	Fatigue, strength
ARALL-4	2024-T81	0.3	0/0	AF191	Fatigue, high temperature
GLARE 1	7075-T6	0.3-0.4	0/0	FM94	Fatigue, strength, σ_Y
GLARE 2A	2024-T3	0.2-0.5	0/0	FM94	Fatigue, strength
GLARE 2B	2024-T3	0.2-0.5	90/90	FM94	Fatigue, strength
GLARE 3	2024-T3	0.2-0.5	0/90	FM94	Fatigue, impact
GLARE 4A	2024-T3	0.2-0.5	0/90/0	FM94	Fatigue, strength in 0°
GLARE 4B	2024-T3	0.2-0.5	90/0/90	FM94	Fatigue, strength in 90°
GLARE 5	2024-T3	0.2-0.5	0/90/90/0	FM94	Impact
GLARE 6A	2024-T3	0.2-0.5	+45/-45	FM94	Shear, off-axis properties
GLARE 6B	2024-T3	0.2-0.5	-45/+45	FM94	Shear, off-axis properties
HSS GLARE 3	7475-T761	0.2-0.5	0/90	FM906	High static strength
HSS GLARE 4A	7475-T761	0.2-0.5	0/90/0	FM906	High static strength in 0°
HSS GLARE 4B	7475-T761	0.2-0.5	90/0/90	FM906	High static strength in 90°

The fibre orientations in Table 2.1 refer to the orientation of the fibres with respect to the rolling direction of the aluminium sheets; i.e. fibres under a 0° angle are aligned with the longitudinal rolling direction and fibres under a 90° angle are in line with the transverse rolling direction [4].

The GLARE grade defines the lay-up but does not indicate the number of plies or the thickness of the metal layers. A coding system is used to specify the lay-up and is defined as follows [15]:



FML types with different metal constituents such as titanium, magnesium or stainless steel or with different fibre types such as carbon or polymer fibres have been developed [9]. However, due to various reasons these FMLs have never found an application in the aerospace industry [9].

In another endeavour to implement FMLs in lower wing panels, CentrAl was developed. Creating thick GLARE panels, i.e. a lot of different plies, gives manufacturing issues and is therefore undesirable. In order to avoid this, CentrAl uses GLARE as a core material on which thicker aluminium sheets are bonded on each side. CentrAl is considered to be a non-conventional FML since the thickness of the aluminium layers is varied and asymmetry can be present [16].

2.3. Future Applications

The fact that GLARE is currently used in the Airbus A380 does not mean that development concerning FMLs has stopped. On the contrary, Airbus is currently exploring options to implement FMLs in applications other than fuselage skins for the A380. Doublers located at door corners are considered to be a suitable application for non-conventional FMLs and can be desirable in terms of weight savings [2].

Embraer recently looked into manufacturing lower wing covers of the wing box structure made from FML¹. A similar application for FMLs is discussed by Alderliesten [9], which constitutes the use of fibres with different stiffnesses and different angle orientations [3]. The most important load case of a wing is bending, therefore a unidirectional laminate would be preferable when taking weight savings into account. However, the need for some resistance against torsion exists as well. The idea is to use stiffer fibres (e.g. carbon fibres) under an angle close to the laminates mid-plane to tailor the shear stiffness. Designing the wing box with this material will allow to tailor the bending and torsional resistance separately [9]. Wilson [17] points out that by varying the thickness of the metal layers and the stacking sequence in an FML, one can choose in which layer the longest crack will grow. For example, in the lower wing panel of a wing box, it is favourable to have the longest crack on the outside for inspection.

These applications serve as good examples to demonstrate the growing need of non-conventional FMLs. However, before these non-conventional FMLs can be implemented, an accurate predictive model must be developed.

2.4. Current Fatigue Crack Growth Models

Many studies have been performed on the prediction of fatigue crack growth in FMLs, of which several make use of phenomenological approaches. The shortcoming of a phenomenological approach is that the complexity of the damage mechanisms in FMLs cannot be described by the proposed methods. Also, the fitting parameters which come into play, make it difficult to apply the model over a wide range of conditions and thus extensive testing is required every time the material or geometry is altered [15].

This urges the need for a model which does not depend on these fitting parameters, as is the case for an analytical model. Having a thorough understanding of how the different damage mechanisms work enables the creation of a model that is able to predict certain damage parameters, such as the fatigue crack growth rate. Multiple attempts have been made to capture the damage propagation in FMLs using an analytical approach, with each research focusing on different aspects.

¹D.F.N.R. da Silva. Embraer: Manufacturing of a Fiber Metal Laminate Lower Wing Cover Demonstrator, FML Outlook: Nov 2 – 3, 2017 Delft, The Netherlands (<https://www.tudelft.nl/en/ae/fml-outlook/speakers/20412/>) - Consulted on 05/11/18

2.4.1. Model of Alderliesten

Alderliesten [5, 11] developed an analytical method to predict fatigue crack growth in GLARE and builds further on the models of Marissen [12] and Guo and Wu [18, 19]. In order to put the model of Alderliesten into perspective, the models of Marissen and Guo and Wu are first briefly introduced.

Marissen [12] introduces the concept of fibre bridging to predict fatigue crack growth analytically in ARALL. The stress intensity at the crack tip is calculated by superposition of the SIFs in the metal layer (crack opening) and the fibre layer (crack closing):

$$K_{tip} = K_{\infty} - K_{br} \quad (2.1)$$

The SIF is determined at the minimum and maximum value of each load cycle to obtain ΔK_{tip} . After correcting ΔK_{tip} for the stress ratio (R-ratio) effect, the crack growth rate can be determined using the Paris relation

$$\frac{da}{dN} = C_{cg} \Delta K_{eff}^{n_{cg}} \quad (2.2)$$

Two other important assumptions are made by Marissen [12] to mathematically describe fibre bridging. Firstly, the delamination around the crack is assumed to have a fixed, elliptical shape. The delamination extension is calculated by determining the delamination growth at the centre line using the Strain Energy Release Rate (SERR), after which the delamination shape is interpolated. Tests performed in later research on other types of FMLs have shown that this assumption is invalid [11, 19]. Secondly, the bridging load along the delamination shape is assumed to be equally distributed. Guo and Wu [19] proved that this assumption is not realistic because the bridging stresses have a peak towards the crack tip. Despite the invalid assumptions, the groundwork for future models was established.

Guo and Wu [18, 19] used the basis of Marissen [12] for their research on fatigue crack growth in GLARE with the distinction that the delamination is divided into different bar elements to calculate the bridging stress in each bar element. This is an improvement compared to the equally distributed bridging stress of Marissen. Despite this improvement, the model of Guo and Wu displays several shortcomings. Firstly, the model uses the laminate stiffness instead of the metal layer stiffness in the computation of the bridging stress, which may lead to unconservative predictions due to overestimation of the bridging stress [11]. Additionally, using the laminate stiffness ignores the residual stresses in the different layers due to curing. Finally, a fixed triangular delamination shape is used, which is calculated in a similar manner as Marissen's elliptical shape.

Before developing his model for crack growth prediction in GLARE, Alderliesten [11] identified the shortcomings of the previous models. The non-constant delamination growth is therefore one of the aspects to be added to the model. Alderliesten [11] requires his method to be (1) physical realistic, i.e. all the relations cannot contain fitting parameters and must be based on a physical mechanism; (2) accurate, i.e. over a wide range of conditions the predictions of the model must be reasonably close to test results; (3) and robust, i.e. initial values for delamination size and shape and crack length are not allowed to influence the predictions. Furthermore, the main assumptions of this model are the same as those of Marissen: (1) the crack growth can be described by Linear Elastic Fracture Mechanics (LEFM) and (2) the Paris relation is also valid for the aluminium layers in the laminate.

Alderliesten assumed through-the-thickness similarity, i.e. equal crack growth in the different metal layers and equal delamination growth at the interfaces, which simplifies the computations. To compute K_{br} in Equation 2.1, the bridging stress (S_{br}) is required. The bridging stress is determined by making use of compatibility

$$v_{\infty}(x) - v_{br}(x) = \delta_f(x) + \delta_{pp}(x) \quad (2.3)$$

where v_{br} and δ_f are functions of the bridging stress. Equation 2.3 states that, at the delamination boundary, the crack opening due to far field stresses (v_{∞}) and the crack closing due to fibre bridging stresses (v_{br}) must be equal to the elongation (δ_f) and deformation (δ_{pp}) of the prepreg layers. One could argue that the metal in the delaminated area has been deformed, however, this deformation is

negligible in comparison to the other terms [18]. The crack opening in the metal due to the far field stresses (v_∞) is calculated in the same manner as for monolithic aluminium [11]

$$v_\infty(x) = 2 \frac{S_{al}}{E_{al}} \sqrt{a^2 - x^2} \quad (2.4)$$

where S_{al} represents the stress in the aluminium layer, E_{al} the stiffness of the aluminium, a the crack length and x the location along the crack length. The displacement due to the bridging stress (v_{br}) is calculated by making a summation of all point loads along crack length a

$$v_{br}(x) = \int_s^a v(x, x_p) dx_p \quad (2.5)$$

where x is the position of the crack opening displacement and x_p is the position where the point load is applied which is approximated by

for $|x| < x_p$:

$$v(x, x_p) = \frac{4S_{br}(x_p)dx_p}{\pi E} \left[\tanh^{-1} \left(\sqrt{\frac{a^2 - x_p^2}{a^2 - x^2 + b(x)^2}} \right) + \frac{0.5(1 + \nu)b(x)^2}{x_p^2 - x^2 + b(x)^2} \sqrt{\frac{a^2 - x_p^2}{a^2 - x^2 + b(x)^2}} \right] \quad (2.6)$$

and for $|x| > x_p$:

$$v(x, x_p) = \frac{4S_{br}(x_p)dx_p}{\pi E} \left[\tanh^{-1} \left(\sqrt{\frac{a^2 - x^2}{a^2 - x_p^2 + b(x)^2}} \right) + \frac{0.5(1 + \nu)b(x)^2}{x^2 - x_p^2 + b(x)^2} \sqrt{\frac{a^2 - x^2}{a^2 - x_p^2 + b(x)^2}} \right] \quad (2.7)$$

where ν is the Poisson ratio and $b(x)$ the height of the delamination at position x . Equation 2.6 and 2.7 are approximations since the exact solution is not given by Tada et al. [20]. Alderliesten combined the solutions for the displacement due to point loads on the centre line above and below the crack flanks and due to point loads on the crack flanks located left and right from the centre line [5].

The integral in Equation 2.5 does not have a closed-form solution due to the bridging stress S_{br} as a function of x_p . Alternatively, the delamination is discretised in bar elements such that the bridging stress is solved numerically. The discretisation is shown in Figure 2.4 with w_i being the width of bar element i , b_i the height and x_i the centre.

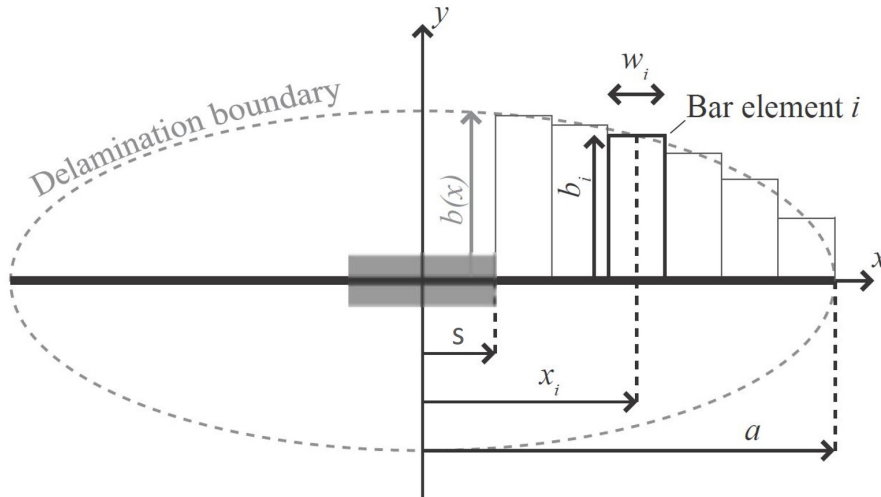


Figure 2.4: Equal delamination discretisation [17]

The left hand side of the compatibility equation (Equation 2.3) has been identified. The terms on the right hand side are defined by Alderliesten [11] as

$$\delta_f = \frac{S_f + S_{br}(x)}{E_f} b(x) \quad (2.8)$$

and

$$\delta_{pp} = C_b S_{al} t_{al} \frac{t_{fi}}{G_{fi}} \sqrt{\left(\frac{G_{f1}}{t_{f1}} + \frac{G_{f2}}{t_{f2}}\right) \left(\frac{1}{2F_{al}} + \frac{1}{F_{f1} + F_{f2}}\right)} \quad (2.9)$$

where C_b in Equation 2.9 is a correction factor for small delamination lengths. F represents the stiffness of a component and is formulated by $F = Etn$ with n being the number of layers of a specific material. The subscripts al , $f1$ and $f2$ denote the aluminium, the first and second layer in the cross-ply, respectively. The subscript fi becomes $f1$ or $f2$ depending on the fibres adjacent to the interface are parallel or perpendicular to the loading [5]. Equation 2.9 is specifically for cross-plies, a similar equation can be formulated for a uni-directional ply.

Substituting the expressions from Equations 2.4 - 2.9 into Equation 2.3, allows the computation of the bridging stress (S_{br}). The bridging stress is a stress acting in the fibre layers and needs to be converted to the equivalent bridging stress for an aluminium layer ($S_{br,al}$), which is done by multiplying S_{br} with the volume fraction of the fibre layers with respect to the metal layers. Next, $S_{br,al}$ is used as an input for K_{br}

$$K_{br} = 2 \sum_{i=1}^N \frac{S_{br,al}(x_i) w_i}{\sqrt{\pi a}} \frac{a}{\sqrt{a^2 - x_i^2 + b_i^2}} \left(1 + \frac{1}{2}(1 + \nu) \frac{b_i^2}{a^2 - x_i^2 + b_i^2}\right) \quad (2.10)$$

Again, this is not an exact solution, but an approximation found in the same manner as Equation 2.6 and 2.7. With K_{br} identified and K_∞ computed as is done for a monolithic metal, Equation 2.1 is evaluated such that the crack growth rate can be determined by Equation 2.2.

Next to the crack growth, the delamination growth is computed. It is assumed that the delamination growth, which grows in loading direction, can be approximated by a 1-D configuration. This simplifies the delamination growth to a closed-form expression. The delamination growth is determined by a Paris-like Equation [11, 21]

$$\frac{db}{dN} = C_d \left(\sqrt{G_{d,max}} - \sqrt{G_{d,min}}\right)^{n_d} \quad (2.11)$$

where G_d represents the SERR. The square roots in Equation 2.11, as identified by Rans et al. [22], are necessary to keep similitude under different loading conditions. The constants C_d and n_d are known for GLARE [23]. The strain energy release rate is given by

$$G_d = \frac{n_f t_f}{2j E_f} \left(\frac{n_{al} t_{al} E_{al}}{n_{al} t_{al} E_{al} + n_f t_f E_f}\right) (S_f + S_{br}(x))^2 \quad (2.12)$$

in which j and n represent the number of aluminium/fibre interfaces and the number of layers, respectively. Once this cycle of determining the crack and delamination extension has been done, it is repeated until the crack growth prediction has reached a certain, specified length.

2.4.2. Model of Wilson

Although Wilson's model is discussed in detail in Chapter 3, a brief summary is given here to demonstrate the differences with Alderliesten's model. The model of Alderliesten [11] meets its requirements; however, when deriving the different components of Equation 2.3, additional assumptions are made which limit the model to GLARE and is therefore not applicable to another type of FML. Wilson [10, 17, 24] establishes the key aspects that need to change in the model of Alderliesten such that it becomes applicable to any type of FML: (1) the crack lengths in the metal layers are equal; (2) the delaminations between the layers are all of equal size; (3) the bridging distribution is assumed to be the same in each delamination. This assumption has an intrinsic contradiction: how can the displacement

in all metal layers be the same if internal metal layers are bridged by two layers whereas external metal layers are only bridged by one layer?; (4) the metal layers within the laminate are of the same alloy and of equal thickness, and the fibre layers are of the same fibre type and limited to 0 and 90 degrees; (5) the load case is tension or compression, no bending.

Wilson uses the same framework for his model as Alderliesten and even though the use of multiple fibre types and an arbitrary fibre orientation are not yet incorporated in Wilson's model, he is able to eliminate the other restrictions stated above. A combined tension-bending load case yields accurate results, in contrast to the pure bending load case in which the performance is poor. The main differences with Alderliesten's model are listed here:

1. Compatibility equation at every delamination: When creating a model which is applicable to FMLs other than GLARE, the delamination at every interface and crack growth rate in every metal layer must be evaluated separately. Therefore, Equation 2.3 must hold at every interface through the thickness [10].
2. Delamination shape discretisation: The results of Alderliesten [11] and Guo and Wu [18] show that the bridging stress changes rapidly near the crack tip. Hence, it makes sense to have an increasing number of bar elements in the vicinity of that location. Wilson [10] makes use of a Chebyshev distribution to bias the number of elements towards the crack tip.
3. Different expressions for compatibility equation terms
 - (a) v_{∞} and v_{br} : Wilson uses the Westergaard stress functions to obtain an exact solution for the crack opening due to far field stresses and the crack closing due to fibre bridging stresses, while Alderliesten uses an approximation [10].
 - (b) δ_{pp} : Wilson determines δ_{pp} by setting the bridging load equal to the shear stress of the bar element, whereas Alderliesten bases his equation on the far field stress [10].
 - (c) δ_f : Since the different layers can all have different crack lengths and, as a consequence different delamination sizes at the interfaces, every bar element is split up into segments. The segment borders are located at the delamination tips. The purpose of these segments is to determine which part of the laminate can be seen as bridging material. The metal layer is seen as bridging material as long as it has one non-delaminated interface [10].
4. Different SERR determination: The strain energy release rate determined by Alderliesten in Equation 2.12 is too specific since it is based on the assumption of through-the-thickness similarity. Since Wilson treats every layer separately, the SERR must be evaluated for every delamination individually at the minimum and maximum value of a load cycle. The derived expression starts from the energy balance and is able to meet the aforementioned requirement.

2.4.3. Model of Khan

The models described so far are based on a Constant Amplitude (CA) loading. Khan [8] built a model to predict the fatigue crack growth for GLARE under Variable Amplitude (VA) loading. CA and VA loading differ in the interaction of load cycles. Interaction in CA is of a constant nature, whereas in VA loading the different loads have a different effect on the crack growth rate. This is illustrated in Figure 2.5 where in region I, when the overload has just been applied, the crack growth rate increases [25]. Due to the overload, a plastic zone ahead of the crack tip has been formed, as is visualised in Figure 2.6. The plastic zone around the crack tip consists of compressive residual stresses. These stresses cause a reduction in the crack tip driving force, resulting in a reduced fatigue crack growth rate which is observed in region II of Figure 2.5. In region III of Figure 2.5 the crack growth rate increases again to the crack growth rate before the application of the overload [25].

Several models exist to predict fatigue crack growth rate under VA loading in metals. Khan [8] evaluated three of these models under several VA load cycles for GLARE 3 to examine whether their applicability can be extended. Due to the fibre bridging effect, the plastic zone and thus the favourable compressive stresses might not be as large when compared to monolithic metals.

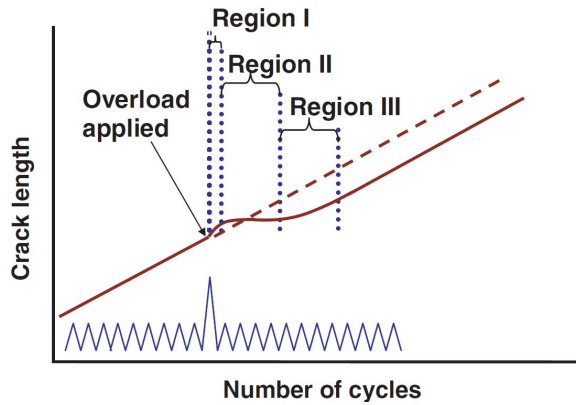


Figure 2.5: Effect of an overload on the crack length [25]

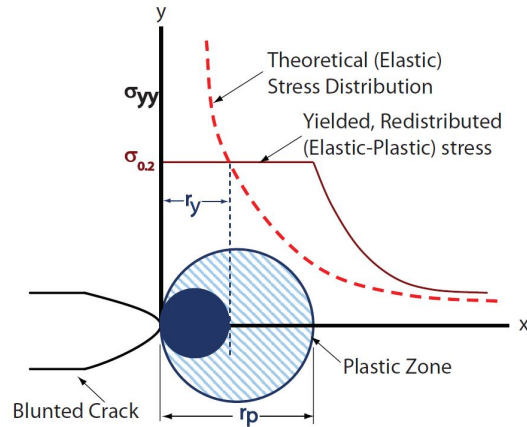


Figure 2.6: Schematic stress distribution and plastic zone formation at the crack tip after an overload [8]

The three models Khan [8] investigated are the Linear Damage Accumulation (LDA) model, the Yield Zone (YZ) model and the Crack Closure (CC) model. The LDA model is a so-called non-interaction model, i.e. it does not take fatigue crack growth acceleration and retardation due to VA loading into account when calculating the crack growth rate. The crack growth is simply a summation of the cycle-by-cycle prediction. The advantage of this model is that it is relatively simple, thus requiring less computational time. Comparing the predictions of this model to experimental data shows that, when distinct load sequences are present, the prediction is not accurate. However, when more random load cycles are present, such as in a flight spectrum, the model's prediction resembles the experimental results.

The YZ model developed by Khan [8] is based on the previous LDA model, although it differs concerning the presence of a retardation module to implement the interaction. It is assumed that little interaction is present due to fibre bridging, however, it will hopefully resolve poor prediction of the LDA model regarding the loading types where retardation is pronounced. The retardation module is based on the Wheeler yield zone model [26], which calculates the crack growth rate differently than Equation 2.2:

$$\frac{da}{dN} = C_p C_{cg} \Delta K_{eff}^{n_{cg}} \quad (2.13)$$

In Equation 2.13 C_p is a value between 0 and 1 depending on the crack tip location in an earlier-formed plastic zone due to an overload (the blue shaded area in Figure 2.6) [8]. Khan [8] discovered that, in general, the yield zone model predicts the crack growth accurately for most spectra with limited load variation.

The last model researched by Khan [8] is the CC model which is based on the CORPUS (Computation Of Retarded Propagation Under Spectrum loading) model, developed by De Koning [27] to predict the crack growth under flight spectra. However, when comparing the predictions and the experimental data, the crack closure model predicts the influence of an overload well, but poorly for the flight spectra. Comparing the three models (LDA, YZ and CC), Khan [8] concluded that the yield zone model performs best.

2.4.4. Model of Spronk

The previously presented models only provide information concerning the crack growth, and not regarding the entire life of an actual structure. The latter can be predicted by the model developed by Spronk [13]. Spronk's research focused on making an accurate prediction of the fatigue crack initiation and propagation of frames with GLARE straps attached to the flanges in the Airbus A400M. This tool allowed Spronk to design alternatives to the current design (benchmark) and quickly evaluate the initiation and propagation behaviour of the alternatives.

For the fatigue crack initiation the model of Homan [28] is used. This model is coupled to the model of Wilson [17] and Alderliesten [5] to add the fatigue propagation part such that the entire life of a

structure can be estimated. If GLARE is taken as input material, the model of Alderliesten is used due to the shorter computational time; in any other case, the model of Wilson is used. These models are based on CA loading, whereas an aircraft frame experiences VA loading. To account for the effects of VA loading, the model of Khan [8] is added as well.

To further complete his model, Spronk added a static strength module in order to determine whether the laminate can sustain limit load. This provides an indication of the Residual Strength (RS), however, an actual residual strength module, providing an accurate residual strength prediction, as developed by Rodi [29] for example, is not present in Spronk's [13] model.

2.4.5. Model of Gupta

With his research on the directionality of crack growth in GLARE under off-axis loading, Gupta [30, 31] explored yet another domain in the research on FMLs. Damage directionality is caused by fibre bridging in the off-axis direction and laminate orthotropy. Similarly to the models described so far, the model of Gupta is based on the superposition of SIFs [31]. Different to the laminates discussed by Alderliesten [5] and Wilson [17] is that off-axis loading creates not only a longitudinal, but also a transverse SIF. In addition to the axial load, a lateral load is present due to clamping an unbalanced laminate. Figure 2.7 illustrates the dissection of the load cases and modes.

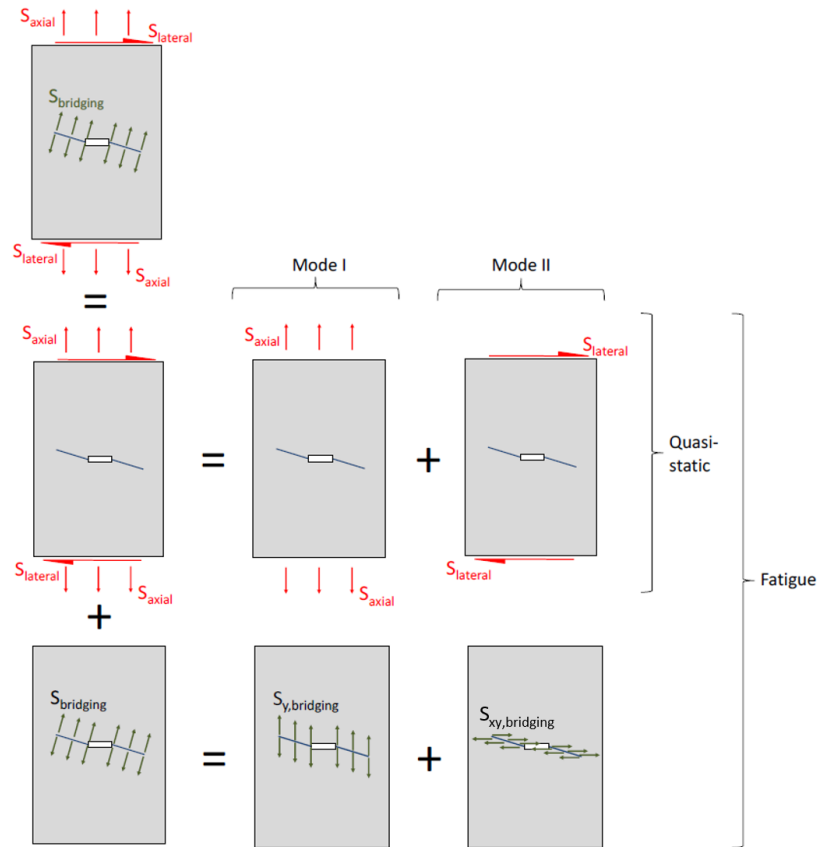


Figure 2.7: The concept of superpositioning the different SIFs [31]

Gupta makes use of Alderliesten's model and derives the transverse SIF in a similar manner Alderliesten did for the longitudinal SIF. Erdogan and Sih [32] discovered that the fracture angle (ϕ) is related to mode I and II in the following manner

$$\cos \frac{\phi}{2} [K_{effI} \sin \phi + K_{effII} (3 \cos \phi - 1)] = 0 \quad (2.14)$$

where K_{effI} and K_{effII} are respectively the effective SIFs for mode I (opening mode) and mode II (in-plane shear mode). Since the delamination around the crack grows in a transverse direction to it, a mode III delamination is present when the fracture angle is other than 0° [17].

2.4.6. Models' Overview

Sections 2.4.1 to 2.4.5 have pointed out that, although considerable research has been carried out to predict fatigue crack growth in standardised FMLs, the research regarding non-conventional FMLs is not as developed. The full advantage of tailoring a material, as is done in composites, is not (yet) exploited by FMLs, amongst others because of the non-existence of an analytical model to quickly predict fatigue crack growth in non-conventional FMLs. Figure 2.8 presents an overview of the previously discussed analytical models and shows that many steps have preceded to come towards a more generalised model. In blue the key points of every model are listed, in black the type of FML for which the model is validated and in white the type of load case the model is built for. The model of Spronk [13], which includes the models of Alderliesten [11], Wilson [10], Khan [8] and Homan [28], is used in the design toolbox of Airbus for the A400M. This demonstrates the importance of Spronk's model, including the value of the individual models it comprises.

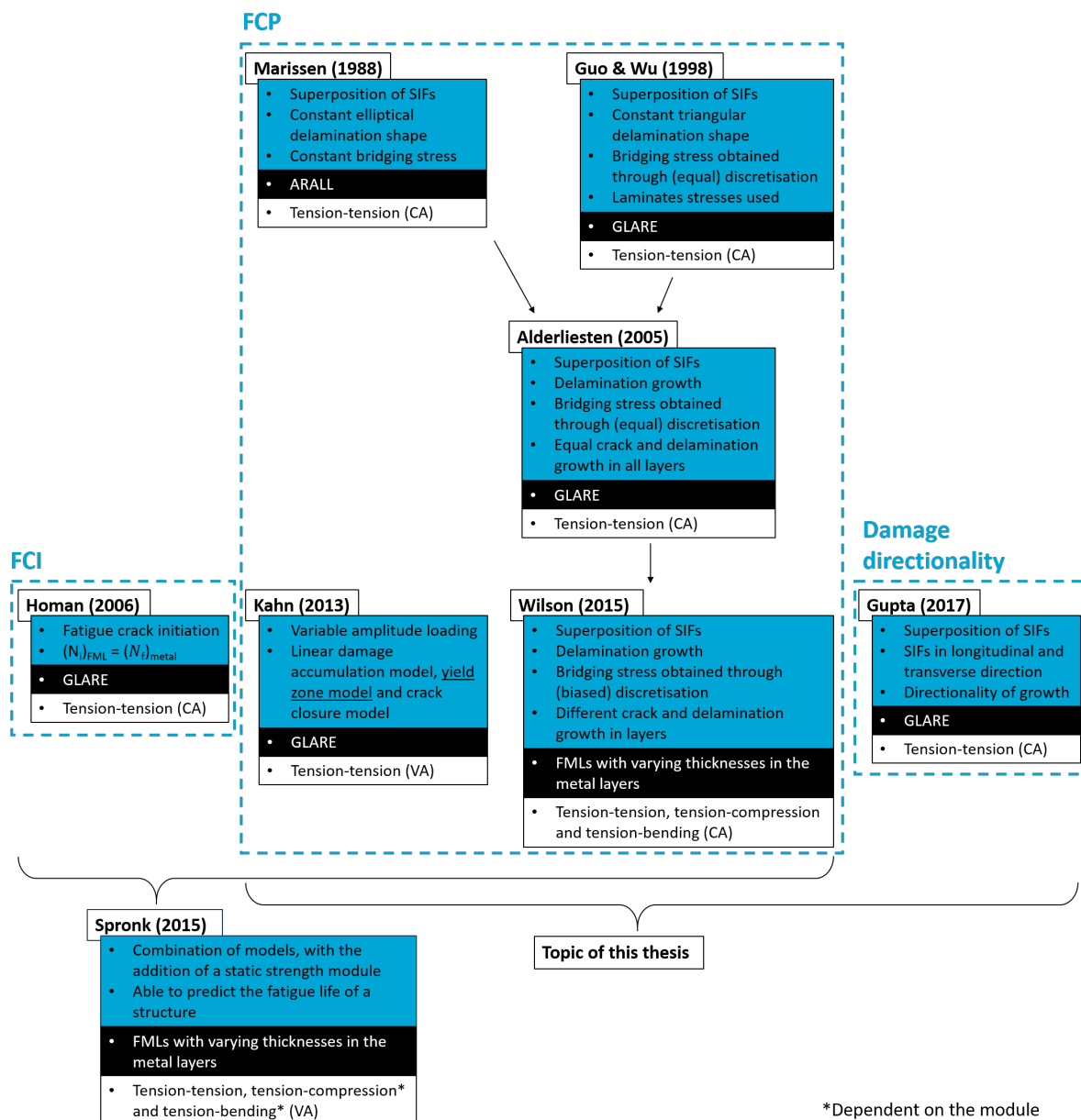


Figure 2.8: Overview analytical models related to FCI, FCP and damage directionality

2.5. Research Goal

With the growing interest in predicting capabilities for non-conventional FMLs, this research is focused on combining the findings from the research presented in Section 2.4 in order to be able to predict the crack growth rate and damage directionality in non-conventional FMLs. To be more specific: the model made by Wilson is used as the foundation and extended by the transverse SIF, which Gupta used for damage directionality prediction, to describe the damage mechanisms in FMLs under off-axis loading. It is presumed that with the implementation of Gupta's theory into the model of Wilson, a model is created that can predict the crack growth rate of FMLs with a varying thickness and an arbitrary fibre orientation. With the applications stated in Section 2.3 in mind, a VA loading must be able to be inserted.

This research topic is indicated in Figure 2.8 in a graphical manner. In analogy with the other models where the main elements are pointed out, the resulting model will include:

- Superposition of SIFs (longitudinal and transverse)
- Delamination growth
- Different crack and delamination growth in layers
- Non-conventional FMLs
- Tension-tension loading

The process to go from analytical GLARE models towards a general FML model consists of many steps. The question rises as to what is needed in order to further develop the current models. This yields the main research question:

How to predict the fatigue crack growth rate and damage directionality for non-conventional FMLs under CA and VA loading?

Before this question can be answered, several sub-questions, each contributing to the main question, need to be answered. The first sub-question relates to the validation of Wilson's model since it has only been validated for laminates with one fibre type. The first sub-question therefore is:

1. To what extent is the model of Wilson valid for FMLs with multiple fibre types?

The second sub-question is related to the arbitrary fibre orientation, which results in off-axis loading and thus a longitudinal and transverse SIF. Due to in-axis loading, Wilson only takes the longitudinal SIF into account. The transverse SIF is used by Gupta to predict damage directionality. This raises the following questions:

2. How to add off-axis loading to the current model?
 - (a) To what extent is it valid to use the SIF in transverse direction, as proposed by Gupta, into the model of Wilson to predict fatigue crack growth under off-axis loading?
 - (b) Under what conditions can a mode III delamination be neglected?

Another difference when modelling non-conventional FMLs is the possibility of having a metal-adhesive-metal configuration instead of the conventional metal-prepreg-metal configuration. This raises the following question:

3. How to model a metal-adhesive-metal configuration?

The main research question also includes the type of loading, being VA. The model of Khan is validated for GLARE which leads to the last sub-question:

4. To what extent is the VA loading module of Khan also valid for non-conventional FMLs?

3

Model

This chapter describes the model to predict fatigue crack growth in non-conventional fibre metal laminates, starting in Section 3.1 with a concise overview; followed by the inputs and initialisation of the model in Section 3.2. Section 3.3 elaborates on the computation of the bridging load, after which the strain energy release rate computation is explained in Section 3.4. In Section 3.5 the bridging load and SERR are used as inputs to compute the crack and delamination growth respectively. The direction in which this damage propagates is elaborated on in Section 3.6. The last section, Section 3.7, highlights the differences between CA and VA loading.

3.1. Model Overview

In order to avoid confusion when discussing the model, definitions and conventions are described in Section 3.1.1. The assumptions are listed in Section 3.1.2 and in the last section, Section 3.1.3, a flow diagram is presented, demonstrating how the work of Gupta [31], where transverse bridging is introduced to predict the fracture angle, is incorporated in the model of Wilson [17] to enable the prediction of individual crack and delamination growth in an FML with an arbitrary lay-up.

3.1.1. Definitions and Conventions

Coordinate System

The coordinate system used in this chapter is defined in Figure 3.1a. The origin is located at the centre of the laminate with the y -axis pointing in the longitudinal direction and the x -axis in the transverse direction. The z -axis is then, by definition of the right-handed coordinate system, pointing upwards. The relevant loads are also indicated in Figure 3.1a and drawn in their positive direction. The fibre angles in the FML are defined with respect to the loading direction, i.e. the y -axis and are positive when rotated clockwise as indicated by the angle θ in Figure 3.1b. The fracture angle (ϕ), hole diameter (D), initial notch size ($2s$) and crack length ($2a$) are also shown in this figure.

Stress Notation

This report follows the convention defined by Schijve [33], meaning that S is used when indicating the applied stress and σ when indicating a local stress. The subscripts further specify the type and direction of loading.

Damage modes

Different failure modes can be distinguished in cracks and delaminations. As depicted in Figure 3.2, mode I is the opening mode, mode II the in-plane shear (or sliding) and mode III the transverse shear (or scissoring) [9]. As an example: the cracks in Figure 2.2a are both mode I, while the delaminations are mode II. If the delamination grows in another direction than parallel to the y -axis but still in-plane, it is defined as a mode III delamination. This type of delamination is observed in off-axis loaded specimens [17, 34]. A pure mode I delamination cannot occur in the configuration of Figure 2.2a because the specimen is loaded in-plane. However, the delamination in Figure 2.2b is a mixed-mode delamination

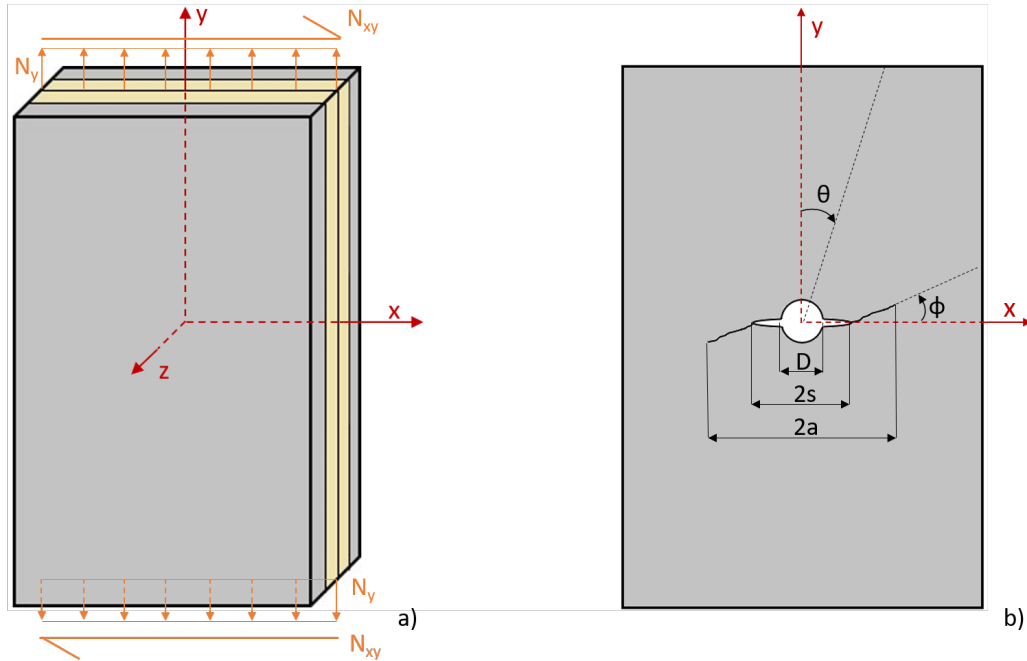


Figure 3.1: Model coordinate system

of mode I and II. A mode I delamination is present due to the shifting of the Neutral Axis (NA) caused by the delamination. This shift induces a misalignment between the neutral axis and the line where the load is applied, resulting in a secondary moment which causes the outer metal layer to deform out-of-plane. Internal delaminations are restrained by the adjacent layers to deform out-of-plane, limiting this phenomenon merely to the outer layers [35].

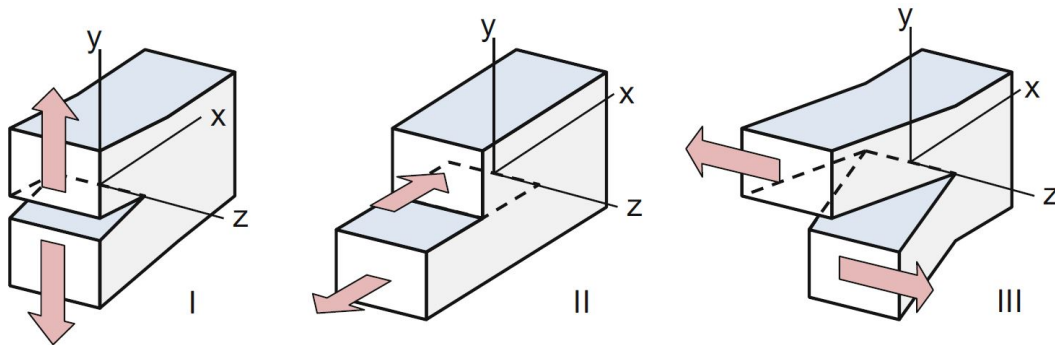


Figure 3.2: Fracture modes: (I) opening; (II) in-plane shear; (III) transverse shear [9]

3.1.2. Model Assumptions

This section lists the main assumptions made in the model. Assumption 1 - 10 are the assumptions made before the model is explained, whereas assumptions 11 - 17 are explained during the derivation and stated here as well with the purpose of providing a complete list of assumptions.

1. The applied stress is assumed to be a uniform applied stress, eliminating any load introduction effects.
2. The initial delamination shape is assumed to be parabolic. Previous models with this assumption have shown this is a valid assumption [11].
3. The effect of anisotropy of the metal plies on the mechanical and fatigue properties is ignored.

4. The crack growth behaviour of the metal plies is assumed to be described by linear elastic fracture mechanics, implying that the stress intensity factor is used to compute the crack growth rate.
5. The experimentally determined Paris constants for thin monolithic sheets are assumed to be representative for thin layers laminated in an FML.
6. The SERR is assumed to be the driver for delamination growth and is subsequently used as an input for a Paris-like equation to determine the delamination growth.
7. Plane stress conditions are assumed for crack growth.
8. Plane strain conditions are assumed for delamination growth.
9. If multiple curing cycles are utilised to manufacture the laminate, it is assumed that these are performed at the same elevated temperature such that the temperature difference between testing and curing is equal in all layers.
10. The stresses and strains in the individual layers are determined by the Classical Laminate Theory (CLT). This involves the following assumptions:
 - (a) The ply thicknesses are small in comparisons to the laminate's width and length such that each ply is in a state of plane stress.
 - (b) Each ply is considered to be a homogeneous layer and orthotropic.
 - (c) The plies in the laminate are bonded perfectly to each other such that strain is continuous through the thickness.
 - (d) The deformations in the laminate follow the Kirchhoff - Love assumptions for bending and stretching of thin plates, which imply that the normals to the mid-plane do not change in length and that the normals to the mid-plane remain straight and normal to the mid-plane, even after deformation.
11. The stress intensity factors of mode I and mode II are superimposed and treated independently.
12. The deformation of the metal in the delaminated area is assumed to be negligible in comparison to the other terms in the compatibility equation and is therefore excluded.
13. The resulting fibre bridging load is always in fibre direction. This implies that, once delaminated, the fibres can rotate to a different angle than defined in the lay-up.
14. It is assumed that the fibre bridging angle at minimum load can be set equal to the fibre bridging angle computed at maximum load since fibre bridging is more pronounced at maximum load.
15. In case the crack has a fracture angle other than 0, it is still modelled as if it would grow under 0 degrees. This assumption simplifies the delamination growth by neglecting a mode III component.
16. Small fracture angles have a negligible influence on the Westergaard stress functions for horizontal cracks.
17. It is assumed that a value of 2 for the Wheeler model exponent (m) is also valid for non-conventional FMLs.

3.1.3. Model Flow Diagram

A flow diagram of the model is presented in Figure 3.3, showing the required inputs and how these inputs are used to start the calculation loop. The boxes highlighted in blue are the steps which are added to the model of Wilson. In parallel to the mode I computation, a mode II computation is performed, after which the two are superimposed as illustrated in Figure 2.7. In order to have an accurate prediction, the calculation loop is repeated once the maximum increment (Δa or Δb), defined by the calculation parameters, has been reached.

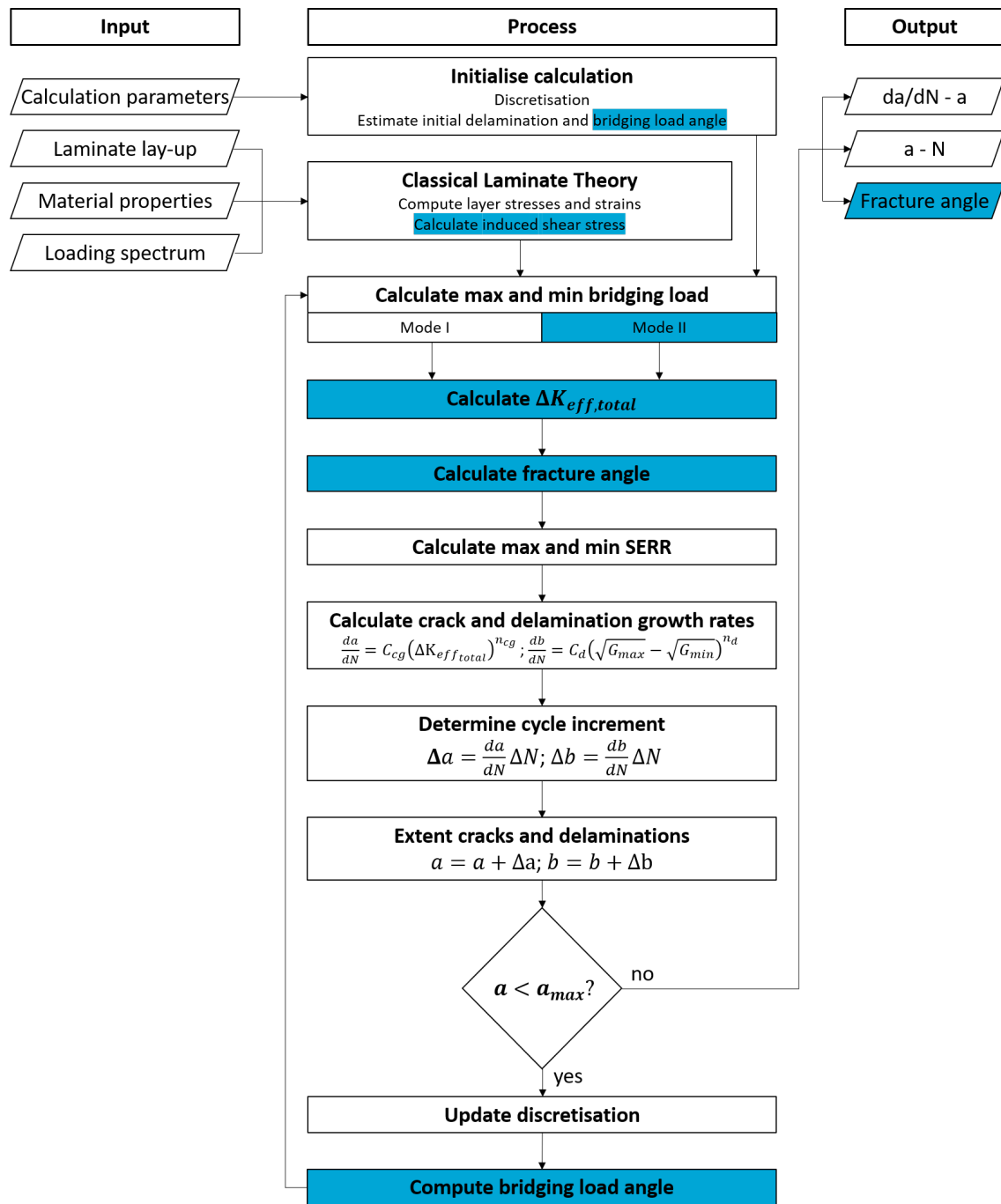


Figure 3.3: Model flow diagram for constant amplitude loading

3.2. Inputs and Initialisation

The required inputs for the model are stated in Section 3.2.1, from which the laminate properties are determined by the CLT in Section 3.2.2. The laminate properties allow the computation of the induced shear stress as discussed in Section 3.2.3. Finally, the model is initialised by discretising the delamination geometry as explained in Section 3.2.4.

3.2.1. Model Inputs

Figure 3.3 shows that the inputs are split up in four categories: calculation parameters, laminate lay-up, material properties and spectrum loading. The calculation parameters contain information concerning

the specimen (width, length, half saw-cut length, curing and testing temperature) and computational parameters such as the final crack length and the maximum width of the bar elements. More information concerning the last parameter is given in Section 3.2.4. The laminate lay-up defines per ply the thickness, the fibre orientation, the material type and the half crack length. The required mechanical and fatigue properties for every material type are listed in Table 3.1. Note that fibre and adhesive layers do not have C_{cg} and n_{cg} , whereas metal layers do not have C_d and n_d . Finally, the spectrum loading can be given for a constant or variable amplitude loading.

Table 3.1: Required model inputs

Symbol	Description	Unit
Calculation parameters		
W	Width of the specimen	[mm]
L	Length of the specimen	[mm]
s	Half length saw-cut	[mm]
T_{cur}	Curing temperature	[°C]
T_{test}	Testing temperature	[°C]
w_{max}	Maximum bar element width	[mm]
a_{max}	Final half crack length	[mm]
Laminate lay-up (per ply i)		
t_i	Thickness	[mm]
θ_i	Ply orientation angle	[°]
ID	Material type	[-]
a_i	Half crack length	[mm]
Material properties		
E_{11}	Modulus of elasticity in 0° direction	[MPa]
E_{22}	Modulus of elasticity in 90° direction	[MPa]
ν_{12}	In-plane Poisson's ratio	[-]
G_{12}	In-plane shear modulus	[MPa]
CTE_1	Coefficient of thermal expansion in 0° direction	[1/°C]
CTE_2	Coefficient of thermal expansion in 90° direction	[1/°C]
C_{cg}	Paris crack growth rate coefficient	[mm · (MPa√mm) ^{-n_{cg}}]
n_{cg}	Paris crack growth rate exponent	[-]
C_d	Delamination growth rate coefficient	[mm · (MPa√mm) ^{-n_d}]
n_d	Delamination growth rate exponent	[-]

3.2.2. Classical Laminate Theory

The laminate lay-up together with the material properties allow the computation of the individual ply stresses and strains under the applied loads given by the spectrum. The classical laminate theory is an often used method for composites to compute these stresses and strain and is also suitable for FMLs. The CLT is not derived here, but can be consulted in literature [36]. Not only on ply-level information is provided by the CLT, but also on laminate-level such as the laminate strains and curvatures. Lastly, the laminate stiffness and compliance matrix are used to calculate the induced shear stress.

3.2.3. Induced Shear Stress

When applying a tension force to an unbalanced laminate, the laminate not only elongates but also shears due to the tension-shear coupling these laminates possess. This phenomenon is depicted in Figure 3.4a [37]. However, this shear deformation is inhibited due to the clamped ends of a specimen in the test machine. Therefore, instead of a shear deformation, a shear stress is present as displayed in Figure 3.4b [37]. Pagano et al. [37] analytically derived the magnitude of this shear stress. Pindera et al. [38] used the derivation from Pagano et al. [37] and simplified it to

$$S_{xy} = -\frac{6\left(\frac{W}{2L}\right)^2 \frac{S_{16}}{S_{11}}}{1 + 6\left(\frac{W}{2L}\right)^2 \frac{S_{66}}{S_{11}}} \cdot S_y \quad (3.1)$$

where W and L are respectively the specimen's width and length. The S -terms with numbers as subscript are the laminate's compliance terms, whereas the S -terms with alphabetical characters as subscript represent stresses. Equation 3.1 is different from what Gupta [31] suggests, where S_{xy} is given by

$$S_{xy} = \frac{S_{16}}{S_{66}} \cdot S_y \quad (3.2)$$

Firstly, the sign is different, meaning that the stress acts in opposite direction. The sign in Equation 3.1 seems to be more appropriate since the shear stress counterbalances the shear deformation, hence the minus sign. Secondly, Equation 3.1 is a scaled version of Equation 3.2 by a factor $\frac{F}{1+F}$ with $F = 6\left(\frac{W}{2L\sqrt{S_{11}}}\right)^2$. This factor can be seen as a finite width correction factor regarding the CLT. Testing a specimen with a larger width will result in a larger S_{xy} compared to a specimen with a smaller width.

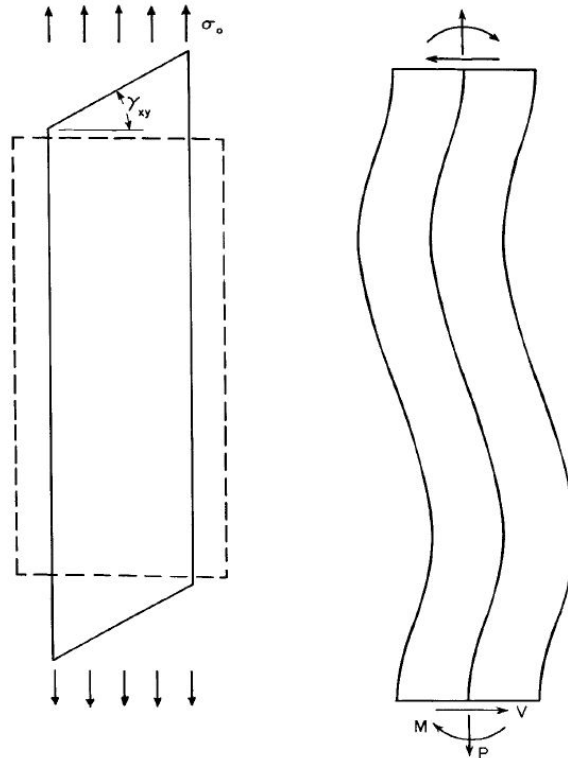


Figure 3.4: Tension-shear coupling in unbalanced laminates under the effect of (a) free ends and (b) clamped ends [37]

3.2.4. Discretisation

The delamination is discretised in bar elements as depicted in Figure 3.5. Wilson [17] mentions that the bridging load is fairly stable over the entire crack length, except near the crack tip, where first an increase followed by a drop in bridging stress is experienced. Due to this phenomenon, it is reasonable to increase the number of bar elements towards the crack tip. Each bar element contains one node which is located at the delamination boundary in the middle of such a bar element (x_i, b_i). Although the different delaminations through the thickness of the laminate are calculated independently and thus not necessarily equal in size, the bar element positions must be the same through the thickness, as the bridging material elongation (δ_{br}) is computed separately for each bar element [17].

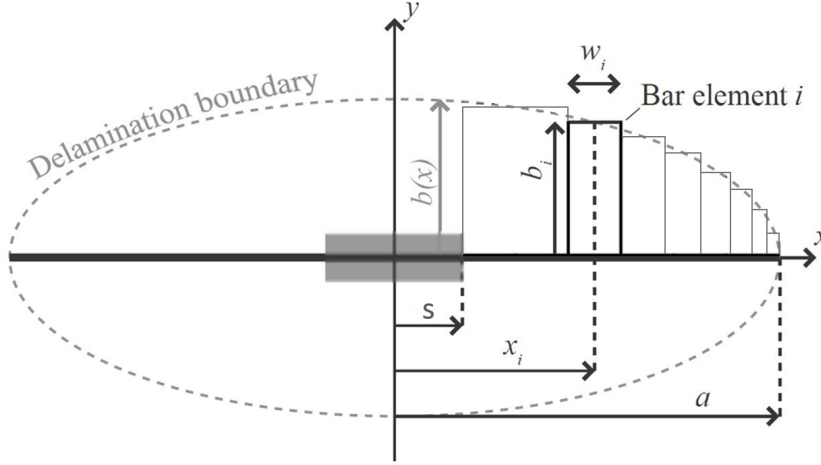


Figure 3.5: Biased delamination discretisation using a Chebyshev distribution

Wilson makes use of a Chebyshev distribution to bias the number of elements towards the crack tip. Since the location of the bar element must be the same at every delamination interface, the crack lengths are sorted in increasing order while leaving out the duplicates. The sorted crack lengths are denoted by \tilde{a} and the intervals between the crack length are called q . The nodes of the first interval are computed as follows:

$$x_j = s + (\tilde{a}_1 - s) \sin\left(\frac{\pi 2j - 1}{4 n_1}\right), \quad j = 1, \dots, n_1 \quad (3.3)$$

while nodes in the other intervals are determined by

$$x_{j+\sum_{i=1}^q n_i} = \tilde{a}_q + (\tilde{a}_{q+1} - \tilde{a}_q) \sin\left(\frac{\pi 2j - 1}{4 n_{q+1}}\right), \quad j = 1, \dots, n_{q+1} \text{ and } q = 1, \dots, N_c - 1 \quad (3.4)$$

where N_c is the number of unique cracks. With the node locations defined, the widths of the bar elements are calculated by taking the derivative of the node locations

$$w_j = \frac{\pi}{2n_1} (\tilde{a}_1 - s) \cos\left(\frac{\pi 2j - 1}{4 n_1}\right), \quad j = 1, \dots, n_1 \quad (3.5)$$

$$w_{j+\sum_{i=1}^q n_i} = \frac{\pi}{2n_{q+1}} (\tilde{a}_{q+1} - \tilde{a}_q) \cos\left(\frac{\pi 2j - 1}{4 n_{q+1}}\right), \quad j = 1, \dots, n_{q+1} \text{ and } q = 1, \dots, N_c - 1 \quad (3.6)$$

The number of nodes in an interval (n_q) is defined by the user input, which sets a limit on the maximum bar element width (w_{max}). The value of n_q is increased until $w_{tip,q} \leq w_{max}$. A smaller w_{max} provides a more accurate computation, but also results in a longer computational time.

With Equation 3.5 and 3.6 in mind, it is possible that the bar element widths are not constantly decreasing in magnitude towards the crack tip as illustrated in Figure 3.5. Figure 3.5 holds when all cracks have the same length. However, when this is not the case, a decrease in element width will be seen, followed by a sudden increase due to the crack tip of the smallest crack and again a decrease until the next crack tip.

3.2.5. Initialisation

The bridging calculation, discussed in Section 3.3, depends on the delamination shape and the bridging angle, therefore an initial estimate must be made. The shape of the initial delamination does not have a large influence on the end result, since the delamination converges within a small number of iterations [11]. Nevertheless, a parabolic delamination shape is chosen based on experiments

$$B_{j,p} = b_{0,k} \cdot \sqrt{1 - \frac{x_j - s}{a_k - s}} \quad (3.7)$$

where $b_{0,k}$ is initial maximum delamination height and typically estimated to be $b_{0,k} = 0.5 \cdot (a_0 - s)$. The subscript k indicates the cracked metal layer and p the delamination interface. Every node has a coordinate in the 3-D reference system, defined in Figure 3.1 in the form of $(x_j, B_{j,p}, z_{int,p})$.

The initial value for the bridging angle is set to zero since in general the bridging angle is rather small. After one iteration this value is adjusted, based on the bridging loads, and used for the next iteration.

3.3. Bridging Load Determination

The model developed by Gupta [31] is based on the same principles as Alderliesten's model [11] for crack propagation in GLARE, being through-the-thickness similarity, which simplifies the problem, but also limits the predicting capabilities to equal crack and delamination growth in all layers. Wilson [10, 17] on the other hand has made a model for a more general FML and therefore makes use of other equations. As a consequence, the terms derived by Gupta cannot be used directly into the model of Wilson. In Section 3.3.2 equivalent terms are derived for the transverse fibre bridging terms, in analogy to the longitudinal ones in Section 3.3.1.

3.3.1. Longitudinal Fibre Bridging Component

This section presents the determination of the bridging load in the longitudinal direction by Wilson [10, 17] and is merely a brief summary of the most important parts as to clarify the entire model. The compatibility equation in longitudinal direction is formulated as

$$v_{\infty}(x, b(x)) - v_{br}(x, b(x))|_{z_{int}} = \delta_{brl}(x)|_{z_{int}} + \delta_{ppi}(x) \quad (3.8)$$

in which it is stated that, at the delamination boundary, the crack opening due to far field stresses ($v_{\infty}(x, b(x))$) and the crack closing due to fibre bridging stresses ($v_{br}(x, b(x))$) must be equal to the bridging material elongation ($\delta_{br}(x)$) and the deformation of the prepreg layers ($\delta_{pp}(x)$) [17]. Equation 3.8 is the same as the compatibility equation used by Alderliesten (Equation 2.3) with the distinction that Equation 3.8 is enforced at every interface (indicated by z_{int}). The metal in the delaminated area also has been deformed, however, this deformation is negligible in comparison to the other terms [19]. In the remainder of this section, an expression for every term in Equation 3.8 (of which some are a function of the bridging load) is derived in order to compute the bridging load.

Crack Opening: $v_{\infty} - v_{br}$

The Westergaard stress functions are used to obtain the exact solutions for v_{∞} and v_{br} [20, 39]. The displacement for a mode I crack due to the far field stress, v_{∞} , assuming plane stress, is defined as

$$v_{\infty}(x) = \frac{1 - \frac{\nu}{1+\nu}}{G} \text{Im}(\bar{Z}_{\infty I}) - \frac{y}{2G} \text{Re}(Z_{\infty I}) - \frac{1}{2G} \frac{3-\nu}{1+\nu} \frac{-3}{2} \frac{\sigma_y}{2} y \quad (3.9)$$

with

$$Z_{\infty I} = \frac{\sigma_y}{\sqrt{1 - \left(\frac{a}{z}\right)^2}} \quad (3.10)$$

$$\bar{Z}_{\infty I} = \sigma_y \sqrt{z^2 - a^2} \quad (3.11)$$

where σ_y is the stress in y -direction of the metal layer with crack length a . In Equation 3.10 and 3.11 $z = x + iy$ where x and y are the coordinates of the location where the compatibility equation is evaluated. The bridging displacement (v_{br}) is defined as¹

$$v_{br}(x_i, b_i, F_{brl}) = \sum_{j=1}^N \frac{v(x_i, b(x_i), x_j, b(x_j)) w_j}{Pt_j} F_{brl}(x_j) \quad (3.12)$$

where

¹Equation 3.12 and 3.16 are different from the equations stated in Wilson's PhD dissertation [17] considering the units in those equations do not match and the inconsistency with the equations used in the code.

$$v(x_i, b(x_i), x_j, b(x_j)) = \frac{1 - \frac{\nu}{1+\nu}}{G} \text{Im}(\bar{Z}_{brl}) - \frac{y}{2G} \text{Re}(Z_{brl}) \quad (3.13)$$

with

$$Z_{brl} = \frac{P}{\pi \sqrt{1 - \left(\frac{a}{z}\right)^2}} \left[\frac{\sqrt{a^2 - z_0^2}}{z^2 - z_0^2} + \frac{\sqrt{a^2 - \bar{z}_0^2}}{z^2 - \bar{z}_0^2} - \alpha y_0 \left(\frac{-iz_0}{(z^2 - z_0^2)\sqrt{a^2 - z_0^2}} + 2iz_0 \frac{\sqrt{a^2 - z_0^2}}{(z^2 - z_0^2)^2} \right. \right. \\ \left. \left. + \frac{i\bar{z}_0}{(z^2 - \bar{z}_0^2)\sqrt{a^2 - \bar{z}_0^2}} - 2i\bar{z}_0 \frac{\sqrt{a^2 - \bar{z}_0^2}}{(z^2 - \bar{z}_0^2)^2} \right) \right] + \frac{P}{\pi} \left[\frac{-y_0}{(z - x_0)^2 + y_0^2} - \frac{y_0}{(z + x_0)^2 + y_0^2} \right. \\ \left. + \alpha y_0 \left(\frac{(z - x_0)^2 - y_0^2}{((z - x_0)^2 + y_0^2)^2} + \frac{(z + x_0)^2 - y_0^2}{((z + x_0)^2 + y_0^2)^2} \right) \right] \quad (3.14)$$

$$\bar{Z}_{brl} = \frac{P}{\pi} \left[\tan^{-1} \left(\frac{\sqrt{z^2 - a^2}}{\sqrt{a^2 - z_0^2}} \right) + \tan^{-1} \left(\frac{\sqrt{z^2 - a^2}}{\sqrt{a^2 - \bar{z}_0^2}} \right) - \alpha y_0 \left(\frac{iz_0}{z^2 - z_0^2} \frac{\sqrt{z^2 - a^2}}{\sqrt{a^2 - z_0^2}} \right. \right. \\ \left. \left. - \frac{i\bar{z}_0}{z^2 - \bar{z}_0^2} \frac{\sqrt{z^2 - a^2}}{\sqrt{a^2 - \bar{z}_0^2}} \right) - i \tanh^{-1} \left(\frac{z}{z_0} \right) + i \tanh^{-1} \left(\frac{z}{\bar{z}_0} \right) + \alpha y_0 \left(\frac{z}{z_0^2 - z^2} + \frac{z}{\bar{z}_0^2 - z^2} \right) \right] \quad (3.15)$$

In Equation 3.14 and 3.15, P represents a point load defined as $P = F_{brl}(x_j) \cdot w_j$ and is applied at the coordinates $z_0 = x_0 + iy_0$. As stated in the Section 3.1.2, the crack growth is assumed to be under plane stress conditions, which defines α to be $\alpha = 0.5(1 + \nu)$ [10, 20]. For later use, it is useful to define the compliance of the bridging displacement as

$$C_{vij} = \frac{v(x_i, b(x_i), x_j, b(x_j)) w_j}{Pt_j} \quad (3.16)$$

Prepreg Shear Deformation: δ_{ppI}

Wilson [17] derived the prepreg shear deformation by setting the bridging load equal to the shear stress of the bar element. This principle is depicted in Figure 3.6, from which the following expression for the prepreg shear deformation is derived

$$\delta_{ppI} = F_{brl} C_b \frac{t_2}{G_{2y}} \sqrt{\frac{G_{2y}}{t_2} \left(\frac{1}{t_1 E_1} + \frac{1}{t_2 E_{2y}} \right)} \quad (3.17)$$

The subscripts 1 and 2 in Equation 3.17 denote the different layers of Figure 3.6. When fibres are oriented in 0° or 90° , the respective modulus of this orientation is taken in Wilson's model. By this logic, when the fibres are orientated at an arbitrary angle, the stiffness with respect to the loading direction should be taken, denoted by subscript y .

Correction factor C_b in Equation 3.17 accounts for the reduction in shear deformation for small delamination lengths. Alderliesten [5] derives the corrections factor for a UD ply to be

$$C_b = 1 - \cosh(\sqrt{\alpha b}) - \tanh(\sqrt{\alpha b}) \sinh(\sqrt{\alpha b}) \quad (3.18)$$

with

$$\alpha = \frac{G_f}{t_f^2 E_f} \quad (3.19)$$

The prepreg shear compliance is required at a later stage in this section and is defined as

$$C_{\tau_{ij}} = C_b \frac{t_j}{G_{jy}} \sqrt{\frac{G_{jy}}{t_j} \left(\frac{1}{t_i E_i} + \frac{1}{t_j E_{jy}} \right)} \quad (3.20)$$

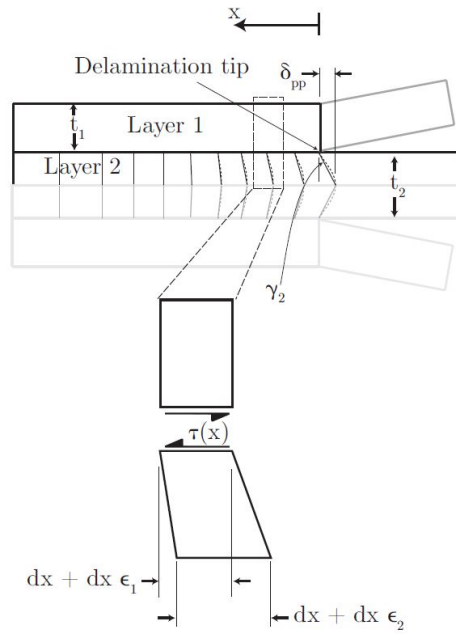


Figure 3.6: Idealisation of shear into bridging stress at the delamination boundary [17]

Bridging Material Elongation: δ_{brl}

The crack length is not necessarily equal in every metal layer and as a consequence different delamination sizes at the interfaces can be present. To determine which part of the laminate is considered as bridging material, every bar element is divided into vertical segments. The segment borders are set at the delamination tips as illustrated in Figure 3.7. The metal layer is considered to be bridging material as long as it has one non-delaminated interface as is the case in segment B and C of Figure 3.7.

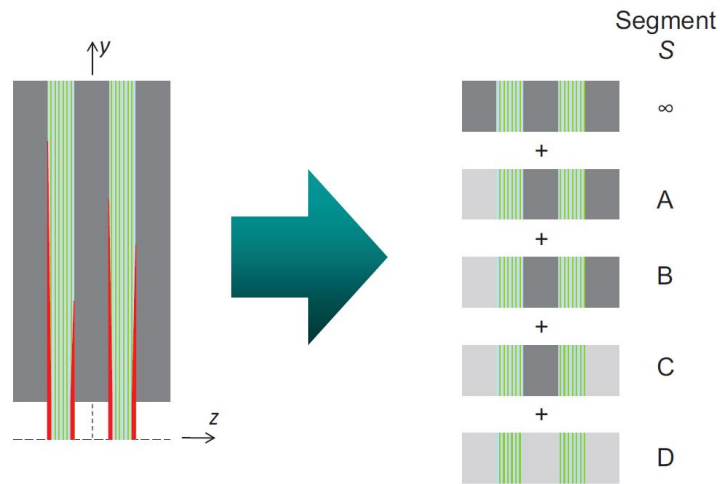


Figure 3.7: Segment definition at a given bar element [17]

The bridging material elongation, $\delta_{brl}(x)$, as derived by Wilson [10] is given by

$$\delta_{brl}(x, b(x, n), z_n) = \epsilon_{\infty}(z_n)b(x, n) + \sum_{m:b(x, m) \geq b(x, n)} F_{brl_m} C_{brl} \quad (3.21)$$

with

$$C_{brl} = \sum_{S:y(S) \leq b(x, n)} \Delta b_S (a_{S_{br11}} + b_{S_{br11}}(z_n + z_m) + d_{S_{br11}} z_n z_m) \quad (3.22)$$

where Δb_S is the difference in delamination length (i.e. the height of one segment), a , b and d are compliance components of the ABD-matrix for segment S and the subscript m refers to the interface subjected to a line load at interface n in segment S .

Since the crack growth rate in the different metal layers is not necessarily equal, one could argue that part of the metal layer which contains the smaller crack, bridges the metal layer with the larger crack as depicted in Figure 3.8 [17]. Running the model with and without this contribution does not deliver sound results whether it is an improvement. For this reason and the fact that it increases the computational time, it is decided, similar to Wilson [17], to not include this term in Equation 3.21.

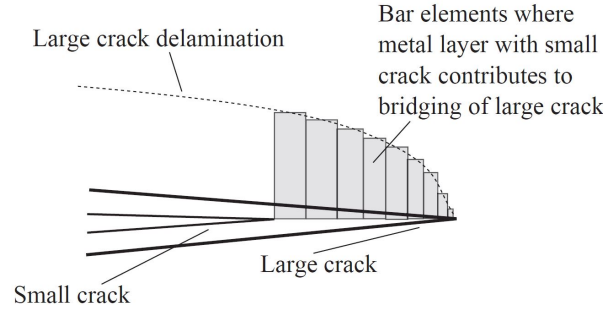


Figure 3.8: Contribution of a metal layer with a smaller crack to the bridging material of a metal layer with a larger crack (fibre layer in between is not shown for clarity) [17]

Bridging Load

Every term in Equation 3.8 has been identified and substituting the different expression into that equation yields

$$v_{\infty i,p} - \sum_{j=1}^{N_k} \left[C_{v_{i,j,p}} F_{br_{i,j,p}} + C_{v_{i,j,op}} F_{br_{i,j,op}} \right] = \epsilon_{\infty p} b_{i,p} + \sum_{m: b_{i,m} \geq b_{i,p}} F_{br_{i,m}} C_{br_{i,m}} + F_{br_{i,p}} C_{\tau_{i,p}} \quad (3.23)$$

The subscripts i and j denote the bar element where the displacement is measured and the bar element where the bridging load is applied, respectively. The subscript k refers to a crack metal layer, which has one (external layers) or two (internal layer) delaminations. The delamination of interest is denoted with subscript p and the opposing delamination of layer k is denoted with subscript op . The op -terms for an external layer are by this logic excluded. Rewriting Equation 3.23 with the unknown $F_{br_{i,p}}$ on one side gives

$$\sum_{j=1}^{N_k} \left[C_{v_{i,j,p}} F_{br_{i,j,p}} + C_{v_{i,j,op}} F_{br_{i,j,op}} \right] + \sum_{m: b_{i,m} \geq b_{i,p}} F_{br_{i,m}} C_{br_{i,m}} + F_{br_{i,p}} C_{\tau_{i,p}} = v_{\infty i,p} - \epsilon_{\infty p} b_{i,p} \quad (3.24)$$

The right hand side of Equation 3.24 is placed in a vector \mathbf{Q}_I with dimensions $\sum_{p=1}^D N_p \times 1$ (N_p is the number of bar elements in delamination p and D the number of delaminations). Similarly, the bridging load $F_{br_{i,p}}$ is placed in a vector \mathbf{F}_I with the same dimensions as vector \mathbf{Q}_I . The other terms are placed in a matrix \mathbf{H}_I with dimensions $\sum_{p=1}^D N_p \times \sum_{p=1}^D N_p$. The bridging load is solved by²

$$\mathbf{F}_I = \mathbf{H}_I^{-1} \mathbf{Q}_I \quad (3.25)$$

where

²While it is not mentioned in Wilson's PhD dissertation [17], the deformation due to residual stress in the metal layers is subtracted from the crack opening in Equation 3.27 in the implementation of the model. The reasoning behind this is that the residual stress is released once the aluminium delaminates. It is not added as a separate term in Equation 3.8 since that equation stems from previous research and is seen as the 'base' equation.

$$\mathbf{F}_I = F_{brl_{i,p}}; \quad i = 1, \dots, N_p; \quad p = 1, \dots, D \quad (3.26)$$

$$\mathbf{Q}_I = v_{\infty_{i,p}} - \epsilon_{\infty_p} b_{i,p}; \quad i = 1, \dots, N_p; \quad p = 1, \dots, D \quad (3.27)$$

$$\mathbf{H}_I = \delta_{pq} C_{v_{i,j,p}} + (\delta_{k_p k_q} - \delta_{pq}) C_{v_{i,j,q}} + \delta_{ij} C_{brl} + \delta_{mn} C_{\tau_{l,p}}; \quad i, j = 1, \dots, N_p; \quad p, q = 1, \dots, D \quad (3.28)$$

The δ -terms in Equation 3.28 represent the Kronecker delta which equals 1 if the two subscript have the same index number, otherwise it equals 0. Subscripts p and q denote the delamination where the displacement is examined and the delamination whose bridging loads are considered, respectively. Subscripts k_p and k_q represent the cracked metal layers which are adjacent to delaminations p and q . The subscripts m and n are related to p and q by

$$m = \sum_{l=1}^p N_l + i \quad (3.29) \quad n = \sum_{l=1}^q N_l + j \quad (3.30)$$

3.3.2. Transverse Fibre Bridging Component

This section outlines the derivation of the transverse bridging load, which is done analogously to the longitudinal component. Similarly to Section 3.3.1, compatibility is enforced at the delamination boundary. For the transverse direction, compatibility is given by

$$u_{\infty}(x, b(x)) - u_{br}(x, b(x))|_{z_{int}} = \delta_{br_{II}}(x)|_{z_{int}} + \delta_{pp_{II}}(x) \quad (3.31)$$

where $u_{\infty}(x, b(x))$ is the crack opening in x -direction due to the far field shear load and $u_{br}(x, b(x))$ represents the crack closure due to fibre bridging. The other terms, $\delta_{br_{II}}(x)$ and $\delta_{pp_{II}}(x)$, are still the bridging material elongation and the prepreg shear deformation, respectively, but in transverse direction instead of in longitudinal direction as in Equation 3.8.

Crack Opening: $u_{\infty} - u_{br}$

The Westergaard stress functions for in-plane shear are taken from Tada et al. [20] to calculate u_{∞} and u_{br} . The crack opening due to the far field load is given by

$$u_{\infty}(x) = \frac{1 - \nu}{G} \text{Im}(\bar{Z}_{\infty_{II}}) + \frac{y}{2G} \text{Re}(Z_{\infty_{II}}) \quad (3.32)$$

with

$$Z_{\infty_{II}} = \frac{\tau_{xy}}{\sqrt{1 - \left(\frac{a}{z}\right)^2}} \quad (3.33)$$

$$\bar{Z}_{\infty_{II}} = \tau_{xy} \sqrt{z^2 - a^2} \quad (3.34)$$

Equation 3.33 and 3.34 are similar to Equation 3.10 and 3.11 with the distinction that the shear stress of the metal layers (τ_{xy}) in a mode II fracture is of interest instead of the stress in y -direction as is the case in a mode I fracture. The crack closure is defined as

$$u_{br}(x_i, b_i, F_{br_{II}}) = \sum_{j=1}^N \frac{u(x_i, b(x_i), x_j, b(x_j)) w_j}{Qt_j} F_{br_{II}}(x_j) \quad (3.35)$$

where

$$u(x_i, b(x_i), x_j, b(x_j)) = \frac{1 - \nu}{G} \text{Re}(\bar{Z}_{br_{II}}) - \frac{y}{2G} \text{Im}(Z_{br_{II}}) \quad (3.36)$$

with

$$\begin{aligned}
Z_{brII} = & \frac{Q}{\pi \sqrt{1 - \left(\frac{a}{z}\right)^2}} \left[\frac{\sqrt{a^2 - z_0^2}}{z^2 - z_0^2} + \frac{\sqrt{a^2 - \bar{z}_0^2}}{z^2 - \bar{z}_0^2} + \alpha y_0 \left(\frac{-iz_0}{(z^2 - z_0^2)\sqrt{a^2 - z_0^2}} + 2iz_0 \frac{\sqrt{a^2 - z_0^2}}{(z^2 - z_0^2)^2} \right. \right. \\
& \left. \left. + \frac{i\bar{z}_0}{(z^2 - \bar{z}_0^2)\sqrt{a^2 - \bar{z}_0^2}} - 2i\bar{z}_0 \frac{\sqrt{a^2 - \bar{z}_0^2}}{(z^2 - \bar{z}_0^2)^2} \right) \right] + \frac{Q}{\pi} \left[\frac{-y_0}{(z - x_0)^2 + y_0^2} - \frac{y_0}{(z + x_0)^2 + y_0^2} \right. \\
& \left. - \alpha y_0 \left(\frac{(z - x_0)^2 - y_0^2}{((z - x_0)^2 + y_0^2)^2} + \frac{(z + x_0)^2 - y_0^2}{((z + x_0)^2 + y_0^2)^2} \right) \right] \quad (3.37)
\end{aligned}$$

$$\begin{aligned}
\bar{Z}_{brII} = & \frac{Q}{\pi} \left[\tan^{-1} \left(\frac{\sqrt{z^2 - a^2}}{\sqrt{a^2 - z_0^2}} \right) + \tan^{-1} \left(\frac{\sqrt{z^2 - a^2}}{\sqrt{a^2 - \bar{z}_0^2}} \right) + \alpha y_0 \left(\frac{iz_0}{z^2 - z_0^2} \frac{\sqrt{z^2 - a^2}}{\sqrt{a^2 - z_0^2}} \right. \right. \\
& \left. \left. - \frac{i\bar{z}_0}{z^2 - \bar{z}_0^2} \frac{\sqrt{z^2 - a^2}}{\sqrt{a^2 - \bar{z}_0^2}} \right) - i \tanh^{-1} \left(\frac{z}{z_0} \right) + i \tanh^{-1} \left(\frac{z}{\bar{z}_0} \right) - \alpha y_0 \left(\frac{z}{z_0^2 - z^2} + \frac{z}{\bar{z}_0^2 - z^2} \right) \right] \quad (3.38)
\end{aligned}$$

Point shear force Q in Equation 3.37 and 3.38 is applied at coordinate $z_0 = x_0 + iy_0$ and is related to the bridging load by $Q = F_{brIIj} \cdot w_j$. For plane stress conditions α is defined as $\alpha = 0.5(1 + \nu)$ [20]. Similarly to the mode I case, the compliance for the bridging displacement is defined as

$$C_{uij} = \frac{u(x_i, b(x_i), x_j, b(x_j)) w_j}{Q t_j} \quad (3.39)$$

Prepreg Shear Deformation: δ_{ppII}

The prepreg shear deformation is similar to the longitudinal case with the distinction that the prepreg properties of the transverse direction should be taken. Adapting Equation 3.17 to the transverse case gives

$$\delta_{ppII} = F_{brII} C_b \frac{t_2}{G_{2x}} \sqrt{\frac{G_{2x}}{t_2} \left(\frac{1}{t_1 E_1} + \frac{1}{t_2 E_{2x}} \right)} \quad (3.40)$$

Doing the same for the compliance term yields

$$C_{\tau II ij} = C_b \frac{t_j}{G_{jx}} \sqrt{\frac{G_{jx}}{t_j} \left(\frac{1}{t_i E_i} + \frac{1}{t_j E_{jx}} \right)} \quad (3.41)$$

Bridging Material Elongation: δ_{brII}

Similar to the bridging material elongation in longitudinal direction, the bridging material elongation in transverse direction consists of two parts, being the elongation caused by the far field strain and the elongation originating from the bridging loads

$$\begin{aligned}
\delta_{brII} &= \epsilon b(x, n) \\
&= (\epsilon_\infty + \epsilon_{brII}) b(x, n) \quad (3.42)
\end{aligned}$$

The elongation due to far field strain (ϵ_∞) is in the mode II case equal to ϵ_{xy_∞} . The mechanical shear strain is inhibited by clamping as discussed in Section 3.2.3, however, a residual shear strain can be present. To find an expression for ϵ_{br} the bridging material for every segment must be determined. This is done by making use of the CLT

$$\begin{bmatrix} N_x \\ N_y \\ N_{xy} \\ M_x \\ M_y \\ M_{xy} \end{bmatrix} = \begin{bmatrix} A_{br11} & A_{br12} & A_{br16} & B_{br11} & B_{br12} & B_{br16} \\ A_{br12} & A_{br22} & A_{br26} & B_{br12} & B_{br22} & B_{br26} \\ A_{br16} & A_{br26} & A_{br66} & B_{br16} & B_{br26} & B_{br66} \\ B_{br11} & B_{br12} & B_{br16} & D_{br11} & D_{br12} & D_{br16} \\ B_{br12} & B_{br22} & B_{br26} & D_{br12} & D_{br22} & D_{br26} \\ B_{br16} & B_{br26} & B_{br66} & D_{br16} & D_{br26} & D_{br66} \end{bmatrix} \cdot \begin{bmatrix} \epsilon_x \\ \epsilon_y \\ \epsilon_{xy} \\ \kappa_x \\ \kappa_y \\ \kappa_{xy} \end{bmatrix} \quad (3.43)$$

Note that the reference frames of the CLT and this model are different. The transverse bridging load can be seen as the applied load at the interface, thus

$$N_{xy} = F_{brII} \quad (3.44)$$

and

$$M_{xy} = F_{brII} z_{int} \quad (3.45)$$

As a result of treating the two modes independently, all other forces and moments are zero. Solving Equation 3.43 for ϵ_{brII} while using Equation 3.44 and 3.45, gives

$$\begin{aligned} \epsilon_{brII} &= \epsilon_{xy} + \kappa_{xy} z_{int} \\ &= a_{br66} N_{xy} + b_{br66} M_{xy} + z_{int} (b_{br66} N_{xy} + d_{br66} M_{xy}) \\ &= F_{brII} (a_{br66} + 2b_{br66} z_{int} + d_{br66} z_{int}^2) \end{aligned} \quad (3.46)$$

Equation 3.46 can be generalised for the case where the strain and the line load to which the strain is subjected do not share the same interface

$$\epsilon_{Snm} = F_{brII,m} (a_{Sbr66} + b_{Sbr66} (z_n + z_m) + d_{Sbr66} z_n z_m) \quad (3.47)$$

Substituting Equation 3.47 into Equation 3.42 gives an equation in the same form as Equation 3.21

$$\delta_{brII}(x, b(x, n), z_n) = \epsilon_{\infty}(z_n) b(x, n) + \sum_{m: b(x, m) \geq b(x, n)} F_{brII,m} C_{brII} \quad (3.48)$$

with

$$C_{brII} = \sum_{S: y(S) \leq b(x, n)} \Delta b_S (a_{Sbr66} + b_{Sbr66} (z_n + z_m) + d_{Sbr66} z_n z_m) \quad (3.49)$$

Bridging load: F_{brII}

The transverse fibre bridging vector (\mathbf{F}_{II}), the transverse displacement vector (\mathbf{Q}_{II}) and the transverse compliance matrix (\mathbf{H}_{II}) have the same dimensions as their longitudinal counterparts. The transverse bridging force is computed in the manner

$$\mathbf{F}_{II} = \mathbf{H}_{II}^{-1} \mathbf{Q}_{II} \quad (3.50)$$

where

$$F_{II} = F_{brII,i,p}; \quad i = 1, \dots, N_p; \quad p = 1, \dots, D \quad (3.51)$$

$$\mathbf{Q}_{II} = u_{\infty,i,p} - \epsilon_{\infty,p} b_{i,p}; \quad i = 1, \dots, N_p; \quad p = 1, \dots, D \quad (3.52)$$

$$\mathbf{H}_{II} = \delta_{pq} C_{u_{i,j,p}} + (\delta_{k_p k_q} - \delta_{pq}) C_{u_{i,j,q}} + \delta_{ij} C_{brII} + \delta_{mn} C_{\tau_{II,p}}; \quad i, j = 1, \dots, N_p; \quad p, q = 1, \dots, D \quad (3.53)$$

3.3.3. Bridging Angle

The bridging angle is the angle under which the fibres are oriented when bridging the metal layers. This angle is not necessarily the same angle as defined in the lay-up since the fibres can move once delaminated. It is assumed that the resulting fibre bridging load is always in fibre direction, which defines the bridging angle to be

$$\theta_{br} = \tan^{-1} \left(\frac{F_{brII}}{F_{brI}} \right) \quad (3.54)$$

The bridging angle is different at the minimum and maximum applied load, resulting in a double computation of the bridging terms in Equation 3.22 and 3.49. Since this is a computationally expensive process, it is assumed that the maximum bridging angle is also valid for the minimum bridging angles. This reduces the computational time since the bridging terms in Equation 3.22 and 3.49 are only computed once. The maximum bridging angle is chosen since fibre bridging is more pronounced at higher loads.

3.4. Strain Energy Release Rate

Equation 2.11 shows that delamination growth is a function of the change in the strain energy release rate and that the growth is perpendicular to the crack. In non-conventional FMLs, the off-axis fibres cause the crack to grow under a certain fracture angle as described in Section 2.4.5, while the delamination still grows perpendicular to the crack and thereby creating a mode III delamination. However, by inspecting the delaminations from the off-axis GLARE tests performed by Gonesh [34, 40] it is discovered that the mode III component in cross-ply FMLs is small in comparison to the mode II delamination. It is therefore decided to ignore the mode III delamination, resulting in modelling the delamination assuming the crack grows under a zero fracture angle. This implicates that the SERR derivation by Wilson [17] only requires minor adaptations.

The derivation of the strain energy release rate is done as general as possible, such that the equations can be applied to arbitrary lay-ups and arbitrary damage sizes. The approach taken to derive the SERR starts with the energy balance

$$G = -\frac{dW}{db} = \frac{d}{db} (F - U_{bot} + U_{top}) \quad (3.55)$$

in which F is the work causing an additional elongation of the laminate due to a growing delamination and U_{bot} and U_{top} represent the strain energy in a cross section below and above the delamination, respectively. Equation 3.55 is evaluated for every bar element at every delamination i

$$G_i = F_i^d - U_{bot,i}^d + U_{top,i}^d \quad (3.56)$$

where the superscript d indicates that the derivative with respect to b , the delamination height, has been taken. Wilson [17] derives the terms of Equation 3.56 to be

$$F_i^d = \sum_{k:k \in \mathbf{B}_{bot}} E_{y,k} t_k [\psi_3^2 - \psi_3 \psi_1 + \frac{1}{12} (\psi_4^2 - \psi_4 \psi_2) t_k^2 + \bar{z}_k (2\psi_3 \psi_4 - \psi_4 \psi_1 - \psi_3 \psi_2) + \bar{z}_k^2 (\psi_4^2 - \psi_4 \psi_2)] \quad (3.57)$$

$$U_{bot,i}^d = \sum_{k:k \in \mathbf{B}_{bot}} \frac{E_{y,k} t_k}{2} \left[\psi_3^2 + 2\psi_3 \psi_4 \bar{z}_k + \psi_4^2 \bar{z}_k^2 + \frac{1}{12} \psi_4^2 t_k^2 \right] \quad (3.58)$$

$$U_{top,i}^d = \sum_{k:k \in \mathbf{B}_{top}} \frac{E_{y,k} t_k}{2} \left[\psi_1^2 + 2\psi_1 \psi_2 \bar{z}_k + \psi_2^2 \bar{z}_k^2 + \frac{1}{12} \psi_2^2 t_k^2 \right] \quad (3.59)$$

where

$$\psi_1 = \epsilon_{k,\infty} + a_{br_{11},top} \sum_{n:b_n > b_i} F_{br_{tot},n} + M_{top} b_{br_{11},top} \quad (3.60)$$

$$\psi_2 = \kappa_\infty + M_{top} d_{br_{11},top} \quad (3.61)$$

$$\psi_3 = \epsilon_{k,\infty} + a_{br_{11},bot} \sum_{n:b_n \geq b_i} F_{br_{tot},n} + M_{bot} b_{br_{11},bot} \quad (3.62)$$

$$\psi_4 = \kappa_\infty + M_{bot} d_{br_{11},bot} \quad (3.63)$$

The summation over k in Equations 3.57 - 3.59 only includes the plies which are seen as bridging material (denoted by \mathbf{B}). The compliance terms of the ABD-matrix ($a_{br_{11}}$, $b_{br_{11}}$ and $d_{br_{11}}$) are determined by the same procedure to evaluate whether a material is considered to be bridging material as explained in Section 3.3.1 and by Figure 3.7. $E_{y,k}$ represents the stiffness of ply k in loading direction (defined in Figure 3.1) and t_k the thickness of that same ply. Finally, $F_{br_{tot}}$ represents the vector product of F_{br_I} and $F_{br_{II}}$ and M the moment created by a shift in the neutral axis.

Since the delamination sizes can vary over the different interfaces, the neutral axis can locally move. This causes secondary bending and thus introduces additional stresses into the laminate. Also, in asymmetric laminates secondary bending is observed as the neutral axis does not coincide with the mid-plane of the laminate. To account for this effect, Wilson [17] derived an adapted Neutral Line Model (NLM) after Schijve [41].

The NLM yielded better predictions concerning delamination growth in simple asymmetric delamination test cases. However, when comparing the results for the crack growth rate between the model with and without the NLM, no major improvement was discovered by Wilson [17], while the computational time increased considerably whereupon Wilson decided to disregard the NLM in his model. This means that M_{top} in Equation 3.60 and 3.61 and M_{bot} in Equation 3.62 and 3.63 are set to zero. The curvature (κ_∞) in asymmetric laminates is not disregarded.

As a consequence of discretising the delamination growth into finite bar elements per cycle, a phenomenon called leapfrogging can arise. Leapfrogging occurs when in the same bar element a short delamination with a high SERR and a large delamination with a low SERR are present. After the first iteration the shorter delamination grows fast due to the high SERR and becomes larger than the slow growing, initially larger delamination. In the next iteration, the behaviour is opposite, resulting in an overestimation of the delamination growth. In an actual delamination, the SERR decreases immediately once the faster-growing delamination begins to extend. For more information concerning this phenomenon and its mitigation, there is referred to [17].

3.5. Damage Growth

The damage is divided into two parts, cracks in the metal plies (Section 3.5.1) and delamination at the ply interfaces (Section 3.5.2). Albeit being two different damage types, they are related to each other, as explained in Section 2.1. The size of the delamination affects the bridging load and thus the crack growth rate.

3.5.1. Crack Growth

As stated in one of the assumptions, the crack growth rate is determined by making use of the Paris relation

$$\frac{da}{dN} = C_{cg} \Delta K_{eff_{total}}^{n_{cg}} \quad (3.64)$$

in which C_{cg} and n_{cg} are the Paris crack growth coefficient and exponent respectively. The first step in determining $\Delta K_{eff_{total}}$ is to evaluate Equation 2.1 (for clarity repeated here) for the maximum and minimum applied load for both mode I and II.

$$K_{tip} = K_\infty - K_{br} \quad (2.1)$$

The test specimen used to validate the model have a finite width and in order to account for this, a Finite Width Correction Factor (FWCF) is applied to Equation 2.1, even though most tests do not have crack length such that the FWCF is of major influence. For GLARE grades the FWCF by Zhao et al. [42] is used, for the other FMLs the Dixon correction factor is applied [5].

The SIF due to far field loading (K_{∞}) is computed similarly as for monolithic metals

$$K_{\infty I, k} = \sigma_{y, k} \sqrt{\pi a_k} \quad (3.65)$$

$$K_{\infty II, k} = \tau_{xy, k} \sqrt{\pi a_k} \quad (3.66)$$

The SIF due to fibre bridging (K_{br}) is the summation of the discretised bridging loads per delamination [17, 20]

for mode I:

$$K_{brIk} = \frac{1}{t_k} \sum_j C_{K_{brI}j} w_j F_{brIk, j} \quad (3.67)$$

with

$$C_{K_{brI}j} = \frac{1}{\sqrt{\pi a_k}} \left[\frac{a_k}{\sqrt{a_k^2 - z_0^2}} + \frac{a_k}{\sqrt{a_k^2 - \bar{z}_0^2}} - \frac{1}{2}(1 + \nu) y_0 a_k i \left(z_0 (a_k^2 - z_0^2)^{\frac{-3}{2}} - \bar{z}_0 (a_k^2 - \bar{z}_0^2)^{\frac{-3}{2}} \right) \right] \quad (3.68)$$

and for mode II:

$$K_{brIIk} = \frac{1}{t_k} \sum_j C_{K_{brII}j} w_j F_{brIIk, j} \quad (3.69)$$

with

$$C_{K_{brII}j} = \frac{1}{\sqrt{\pi a_k}} \left[\frac{a_k}{\sqrt{a_k^2 - z_0^2}} + \frac{a_k}{\sqrt{a_k^2 - \bar{z}_0^2}} + \frac{1}{2}(1 + \nu) y_0 a_k i \left(z_0 (a_k^2 - z_0^2)^{\frac{-3}{2}} - \bar{z}_0 (a_k^2 - \bar{z}_0^2)^{\frac{-3}{2}} \right) \right] \quad (3.70)$$

The two modes are combined according to Tada et al. [20] by

$$K_{tipTotalk} = \sqrt{K_{tipIk}^2 + K_{tipIIk}^2} \quad (3.71)$$

Finally, the SIF is corrected to the effective SIF to take crack closing into account during the load cycle. Schijve [43] empirically determined this correction to be

$$\Delta K_{effTotalk} = (0.55 + 0.35R_{K_k} + 0.1R_{K_k}^2)(1 - R_{K_k})K_{tipTotal, maxk} \quad (3.72)$$

where R is not the stress ratio of the applied stress, but of the stress experienced by the cracks [44]

$$R_{K_k} = \frac{K_{tipTotal, mink}}{K_{tipTotal, maxk}} \quad (3.73)$$

3.5.2. Delamination Growth

The delamination growth rate is determined in a similar manner as the crack growth rate. The SERR as derived in Section 3.4 is evaluated at the minimum and maximum load and used as input for a Paris-like equation

$$\frac{db}{dN} = C_d \left(\sqrt{G_{d,max}} - \sqrt{G_{d,min}} \right)^{n_d} \quad (2.11)$$

The square roots in Equation 2.11, as identified by Rans et al. [22], are necessary to keep similitude under different loading conditions. As mentioned in Section 3.1.2, the delamination is modelled as if there is no mode III delamination present. Figure 3.9 illustrates the rotation of the actual delamination and the modelled delamination.

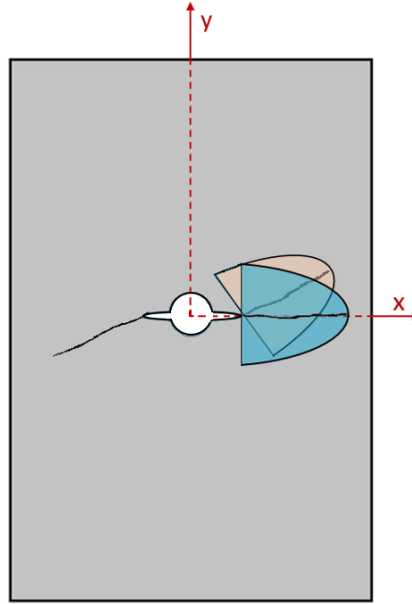


Figure 3.9: Visualisation of the actual damage growth (orange) and the modelled damage growth (blue). Dimensions are for illustration purposes.

3.6. Fracture Angle

Section 3.2 to 3.5 discuss the different steps to determine the crack growth rate; however, it is not yet computed in which direction the crack grows. It is assumed that the fracture angle is small and therefore has minimal influence on the accuracy of Equation 3.14, 3.15, 3.37 and 3.38 since these equations are only valid for cracks without a fracture angle.

Gupta [31] demonstrates that the fracture angle under mixed-mode loading is calculated by the following equation from Erdogan and Sih [32]

$$\cos \frac{\phi}{2} [K_{effI} \sin \phi + K_{effII} (3 \cos \phi - 1)] = 0 \quad (2.14)$$

From Equation 2.14 it is noted that when there is no mode II (i.e. $K_{effII} = 0$), as is the case for in-axis GLARE, the fracture angle equals 0 and π . However, in non-conventional laminates a mode II is likely to be present and thus Equation 2.14 is rewritten to ϕ . Mathematically this gives two solutions indicated by ' \pm '; however, tests have shown that Equation 3.74 with the minus sign is the one which predicts the fracture angle correctly

$$\phi = 2 \frac{180}{\pi} \tan^{-1} \left(\frac{K_{effI} \pm \sqrt{K_{effI}^2 + 8K_{effII}^2}}{4K_{effII}} \right) \quad (3.74)$$

3.7. Differences between CA and VA Loading

The model discussed in Section 3.2 - 3.6 focused on constant amplitude loading. Differences exist compared to variable amplitude loading and are addressed in this section. These differences comprise additional assumptions (Section 3.7.1), additional inputs (Section 3.7.2) and different computations for VA loading (Section 3.7.3). Two of the three VA models discussed in Section 2.4.3 are coupled to the model by Spronk [13], being the LDA and YZ model. The former for its short computational time and the latter because of the most accurate predictions it provides. Section 3.7.4 contains a flow diagram similar to Figure 3.3.

3.7.1. Assumptions

The VA module has one more assumption compared to CA loading, being:

1. It is assumed that a value of 2 for the Wheeler model exponent (m) is also valid for non-conventional FMLs. Khan [8] states that the Wheeler model exponent is experimentally determined and depends on the load spectrum, stress level and the crack shape. However, Khan himself used a value of 2 for m for in-axis tested GLARE specimens, which results in accurate predictions, without clearly stated what the origin of this value is.

3.7.2. Inputs

The VA module allows different types of loading (e.g.: overload, block and flight spectra) to be inserted as input. Lay-up and material properties do not require any additions to the parameters listed in Table 3.1. In the calculation parameters it must be indicated which method must be used, the LDA or YZ model. In case the YZ model is chosen, an additional calculation parameter is needed: the Wheeler model exponent (m), which is experimentally determined.

3.7.3. Computations

Depending on the model (LDA or YZ) the difference in computations compared to CA loading lies within the crack growth rate. The LDA model shows no difference since it is a summation of the damage caused by individual cycles

$$a = a_0 + \sum_{i=1}^n \Delta a_i \quad (3.75)$$

Equation 3.75 demonstrates that the crack growth is not influenced by what has preceded. This results in a conservative prediction, since load history effects slow down the crack growth rate [33].

The YZ model on the other hand takes history effects into account and is based on the location of the crack in a larger created yield zone caused by an overload compared to the yield zone under CA loading. The yield zone comprises compressive stresses which reduce the crack-opening stress field, resulting in a smaller crack growth rate.

An adapted version of Equation 2.13 is presented here, in which the transverse SIF has been included

$$\frac{da}{dN} = C_p C_{cg} \Delta K_{eff_{total}}^{n_{cg}} \quad (3.76)$$

The value of C_p depends on the location of the crack tip in the plastic zone of the overload ($r_{p,OL}$) and the plastic zone of the current cycle ($r_{p,i}$). C_p factorises the crack growth rate to take the history effects into account by having a value between 0 and 1 and is determined by

$$C_p = \left[\frac{r_{p,i}}{a_{OL} + r_{p,OL} - a_i} \right]^m \quad \text{when } a_i + r_{p,i} < a_{OL} + r_{p,OL} \quad (3.77)$$

or

$$C_p = 1 \quad \text{when } a_{OL} + r_{p,OL} \leq a_i + r_{p,i} \quad (3.78)$$

in which a_{OL} represents the crack length at the overload and a_i the current crack length. Figure 3.10 supports to visualise Equation 3.77 and 3.78.

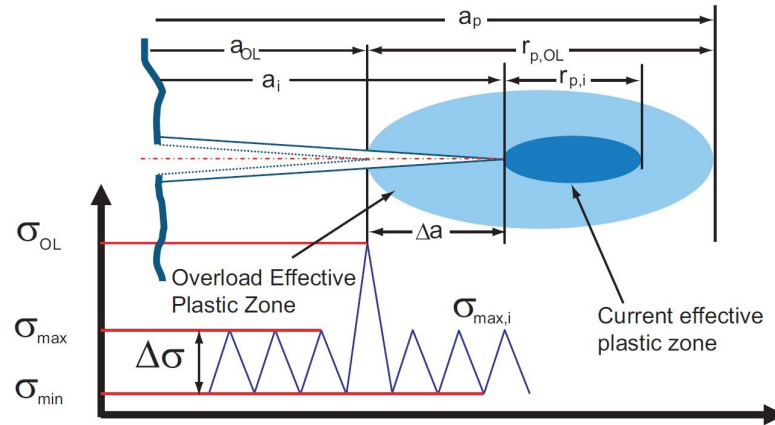


Figure 3.10: Plastic zone sizes used in YZ model [8]

The size of the plastic zone in Equation 3.77 is assumed to be determined by the transition from plastic to elastic material which happens when the stresses in the vicinity of a crack satisfy a yield criterion [45]. An often used criterion is the von Mises yield criterion [46]

$$(\sigma_{xx} - \sigma_{yy})^2 + (\sigma_{yy} - \sigma_{zz})^2 + (\sigma_{zz} - \sigma_{xx})^2 + 6(\tau_{xy}^2 + \tau_{yz}^2 + \tau_{zx}^2) = 2\sigma_Y^2 \quad (3.79)$$

Tada et al. [20] define the stress field in the vicinity of a crack to be

for mode I:

$$\begin{bmatrix} \sigma_{xx} \\ \sigma_{yy} \\ \tau_{xy} \end{bmatrix} = \frac{K_I}{\sqrt{2\pi r}} \cos \frac{\theta}{2} \begin{bmatrix} 1 - \sin \frac{\theta}{2} \sin \frac{3\theta}{2} \\ 1 + \sin \frac{\theta}{2} \sin \frac{3\theta}{2} \\ \sin \frac{\theta}{2} \cos \frac{3\theta}{2} \end{bmatrix} \quad (3.80)$$

and for mode II:

$$\begin{bmatrix} \sigma_{xx} \\ \sigma_{yy} \\ \tau_{xy} \end{bmatrix} = \frac{K_{II}}{\sqrt{2\pi r}} \begin{bmatrix} -\sin \frac{\theta}{2} \left(2 + \cos \frac{\theta}{2} \cos \frac{3\theta}{2} \right) \\ \sin \frac{\theta}{2} \cos \frac{\theta}{2} \cos \frac{3\theta}{2} \\ \cos \frac{\theta}{2} \left(1 - \sin \frac{\theta}{2} \sin \frac{3\theta}{2} \right) \end{bmatrix} \quad (3.81)$$

in which θ is the angle with respect to the x -axis and r the radius as depicted in Figure 3.11.

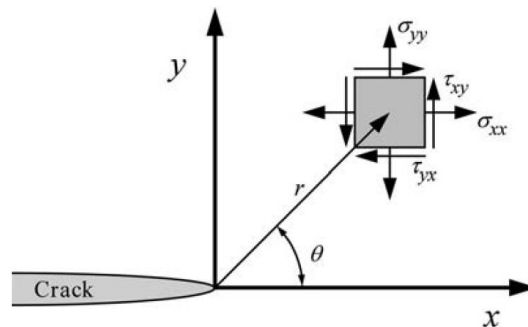


Figure 3.11: Coordinate and parameter definition ahead of the crack tip [45]

Due to the dissection of modes as depicted in Figure 2.7, only σ_y is present for mode I and only τ_{xy} for mode II [46]. Substituting the relevant terms from Equations 3.80 and 3.81 into Equation 3.79 and modelling the crack straight, resulting in $\theta = 0$, gives

$$r_y = \frac{1}{2\pi} \frac{K_I^2 + 3K_{II}^2}{\sigma_Y^2} \quad (3.82)$$

Equation 3.82 is not entirely correct since the derivation is based on elastic crack-tip solutions and stresses redistribute when yielding occurs in order to satisfy equilibrium [46]. The stresses exceeding the yield stress (σ_Y), as seen in Figure 3.10, cannot be carried by the elastic-plastic material causing the plastic zone to enlarge to accommodate for these stresses. Irwin [45] proposes a second-order estimate of r_p

$$\sigma_Y r_p = \int_0^{r_y} \sqrt{\frac{K_I^2 + 3K_{II}^2}{2\pi r}} dr \quad (3.83)$$

Solving for r_p gives

$$r_p = \frac{1}{\pi} \frac{K_I^2 + 3K_{II}^2}{\sigma_Y^2} \quad (3.84)$$

3.7.4. Flow Diagram

The flow diagram for the VA model is shown in Figure 3.12, where again the blue boxes indicate the additions to the existing model. Different to the model for CA loading is that the number of cycles cannot be calculated by dividing the crack increment by the crack growth rate, because the load might change within the aforementioned number of cycles and thus creating different crack growth rates. Instead, every load is evaluated and the delamination shape is not updated until the desired increment has been reached. In order to limit the number of calculation loops, the spectrum is searched for unique load levels and given a load identification number. At the end of a calculation loop, the result is stored in a database which is checked before a new loop starts to see whether the results already exists for the current load. The database is emptied and the delamination shape is updated once the desired crack growth increment has been reached since the calculated values are no longer valid. Spronk [13] states that by this method, the computational time is 10 times shorter for the same load spectrum.

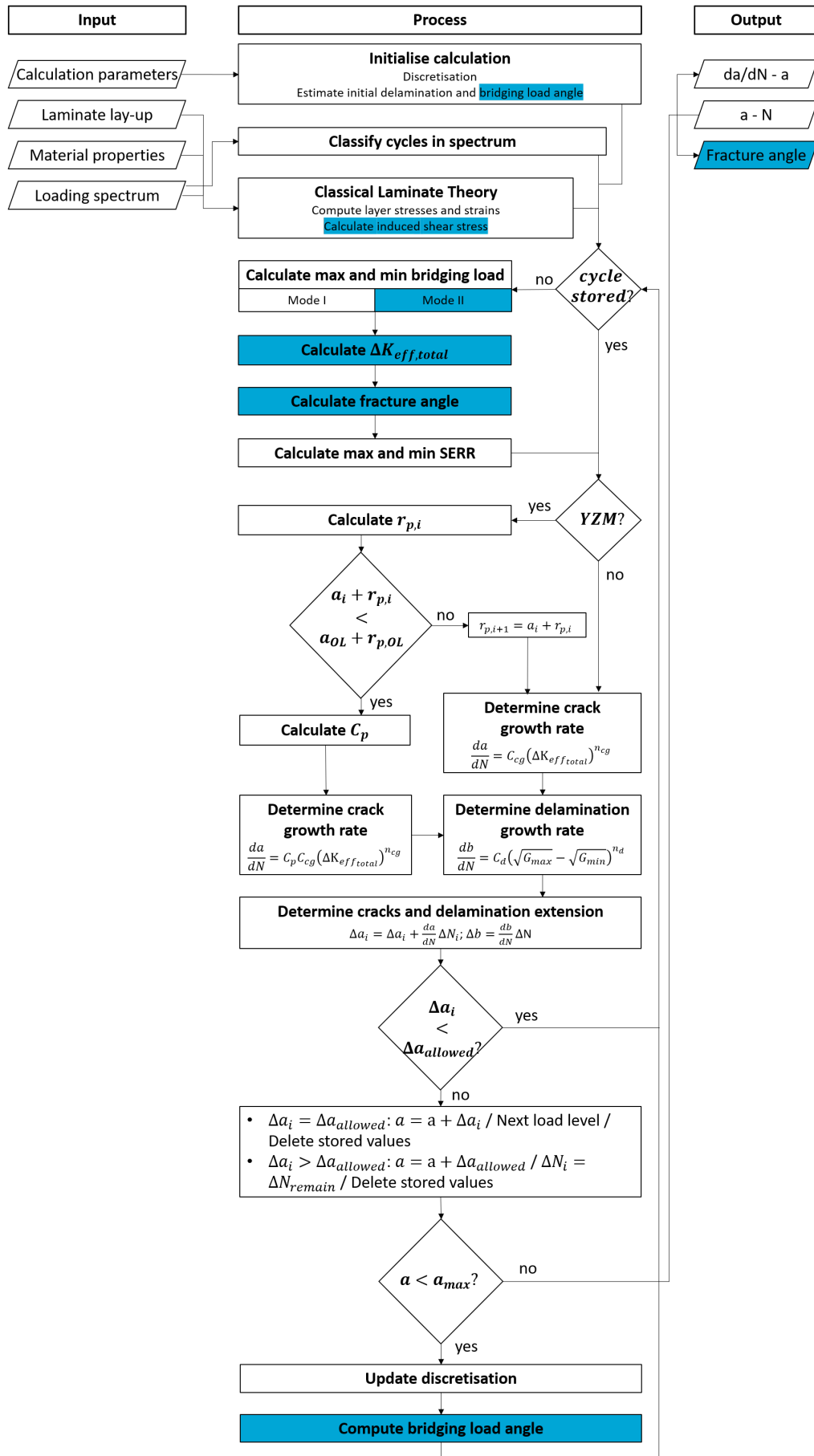
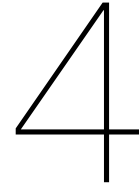


Figure 3.12: Model flow diagram for variable amplitude loading



Testing and Results

Fatigue crack growth tests are performed to validate the model and define its limit of validity. Section 4.1 explains which tests are performed and motivates how these tests contribute to the validation of the model. Section 4.2 provides insight into the manufacturing process of the specimens. The test set-up is discussed in Section 4.3 and post-test inspection procedures in Section 4.4. The test results are presented in Section 4.5.

4.1. Design of Test

In total six tests were carried out to validate certain aspects of non-conventional FMLs which cannot be validated by legacy test data. The test parameters are listed in Table 4.1 and further explained in Section 4.1.1 to 4.1.3. The possibility exists that the actual geometrical values are slightly different from the values stated in Table 4.1 due to manufacturing inaccuracies. The actual geometrical values are stated in the test reports in Appendix A. Furthermore, laminate 1 and 2 from Table 4.1 are defined as:

- Laminate 1¹: [Al2524-T3 (1.3 mm) / 2 C_{15°} / GLARE 3-3/2-0.4 / 2 C_{15°} / Al2524-T3 (1.3 mm)]
- Laminate 2¹: [Al2524-T3 (1.3 mm) / 2 C_{15°} / GLARE 3-3/2-0.4 / 2 C_{15°} / Al2524-T3 (1.3 mm) / 2 C_{0°} / Al2524-T3 (1.3 mm)]

Table 4.1: Geometrical and loading parameters of test specimens

Test ID	Laminate	Off-axis angle [deg]	Length x Width [mm x mm]	t [mm]	2s [mm]	CA / VA	S _{max} [MPa]	R [mm]
1	GLARE 2A-4/3-0.3	10	365 x 140	2.00	5	CA	100	0.05
2	GLARE 2A-4/3-0.4	80	365 x 140	2.40	5	CA	100	0.05
3	GLARE 3-4/3-0.5	22.5	350 x 140	2.40	5	VA	160	0.05
4	Laminate 1	0	365 x 140	4.86	5	CA	100	0.05
5	Laminate 1	0	365 x 140	4.86	5	CA	140	0.05
6	Laminate 2	0	360 x 140	6.43	5	CA	140	0.05

4.1.1. Fracture Angle

The variation of the fracture angle over the Off-Axis Angle (OAA), as presented in Figures 5.5 - 5.7, shows a similar trend between Gupta's prediction and the prediction of the discussed model for GLARE 3 and GLARE 4B. However, for GLARE 2A the two predictions vary. Therefore, a GLARE 2A specimen at an off-axis angle of 10° is tested, as this is the angle where the two predictions vary most. Furthermore, test data at off-axis angles of 67,5° and 70° indicate that the fracture angle decreases

¹The 'C' denotes a carbon fibre ply. In general, it is not advised to use carbon fibres and aluminium as adjacent plies in a laminate because of galvanic corrosion [9]. However, this laminate is built purely for the validation of the model.

rapidly; something the model does not capture accurately. Hence, it is interesting to test a GLARE 2A specimen at an off-axis angle of 80° to confirm this trend.

4.1.2. Variable Amplitude Loading

Test 3 comprises a GLARE 3 specimen tested at an off-axis angle of 22.5° and is chosen to check whether the prediction model from Khan [8] for in-axis GLARE is also valid for off-axis GLARE. The type of VA loading selected is a spectrum with multiple overloads such that the crack growth retardation can be measured multiple times, something which is harder to detect in for example a flight spectrum. In total 3 overloads were applied of 160 MPa at 80, 120 and 160 kcycles. The base loading has a maximum stress level of $S_{max} = 100$ MPa with stress ratio $R = 0.05$.

The first overload is applied after 80 kcycles such that the test data from the first 80 kcycles can be compared to a similar test performed by Gonesh [40] under CA loading (See Figure B.3). For that specific test, the test data and prediction deviate and thus test 3 will also verify the test data from Gonesh. In contrary to the GLARE 3-4/3-0.4 from Gonesh, a GLARE 3-4/3-0.5 is tested due to the unavailability of the former lay-up. Despite the different lay-up, it can still be checked whether a gap between test data and prediction is present for test 3.

4.1.3. Unbalanced and Asymmetric Laminates

Gonesh [34, 40] performed crack growth tests on GLARE 2A, GLARE 3, GLARE 4B, GLARE 5 and metal sheets bonded by an adhesive under various off-axis angles and various stress amplitudes. Some tests are performed with balanced laminates, such as GLARE 3 under an off-axis angle of 45°, and are categorised here as type 1 in Table 4.2. However, the majority of the test specimen tested by Gonesh are unbalanced and are indicated by type 2. Two tests are done with adhesively bonded aluminium sheets and are called type 3.

Rensma [44] performed crack growth tests on non-conventional FMLs consisting of glass fibres, carbon fibres, aluminium sheets and stainless steel sheets. The tested laminates are all balanced and symmetric; however, some only contained fibres in loading direction (type 1) and some in other directions (type 2).

Table 4.2: Overview relating (legacy) test data to the characteristics of non-conventional FMLs

Characteristic	Gonesh			Rensma		Own tests	
	Type 1	Type 2	Type 3	Type 1	Type 2	Test 4 & 5	Test 6
Fibre orientation other than 0° or 90°	yes	yes	NA	no	yes	yes	yes
Multiple fibre types	no	no	NA	yes	yes	yes	yes
Multiple metal types	no	no	no	yes	yes	yes	yes
Multiple metal thicknesses	no	no	no	yes	yes	yes	yes
Unbalanced laminate	no	yes	no	no	no	yes	yes
Asymmetric laminate	no	no	no	no	no	no	yes
Metal-metal interface	no	no	yes	no	no	no	no

When summarising the tested laminates from legacy data in Table 4.2 and relating them to the characteristics of a non-conventional FML, it becomes clear which criteria need to be tested and validated. Test 4 and 5 are done with a laminate which combines 5 out of 7 characteristics. Test 6 adds asymmetry into the laminate to validate whether the crack grows faster on one side than the crack on the other side due to the secondary bending moment caused by the offset in the laminate's neutral axis and mid-plane.

4.2. Laminate Manufacturing

The Al2524-T3 sheets in laminate 1 and 2 are first anodised by a chromic-acid and subsequently coated by BR127 primer, to enhance the durability of the bond between aluminium and epoxy and to protect the aluminium from corrosion [4]. This is the same primer as used on the aluminium sheets of GLARE [4]. The carbon fibre reinforced polymer used is DT120 from DeltaTech [47] which is placed on the prefabricated GLARE laminate by hand. To ensure minimal voids are present, a precompacting machine is used to eliminate the air between the different layers. The laminate is built by stacking the different layers and is subsequently placed under vacuum into an autoclave. The curing cycle is set at a temperature of 120°C with a pressure of 6 bar, according to the specifications provided in the data sheet of the carbon fibre prepreg [47]. It is assumed that the additional curing cycle does not have any effect on the properties of the GLARE core, as it is common practice to manufacture (sub)structures in multiple curing cycles [4].

Figure 4.1 illustrates the final specimen geometry. Once the laminate is cured, it is cut to specimen size as defined in Table 4.1. Next, tabs are adhesively bonded to the clamping area to prevent crack growth at one of the holes drilled for clamping. Subsequently, the holes for clamping are drilled and a small hole is drilled (1.5 mm) in the middle of the specimen from which the saw-cuts are made to initiate the crack.

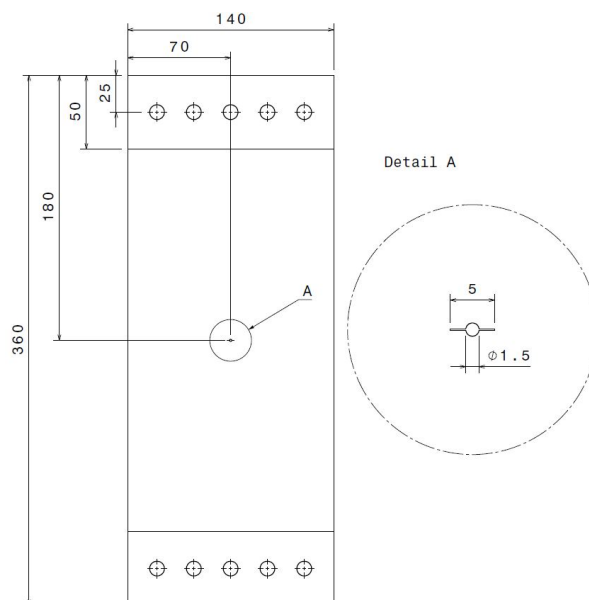


Figure 4.1: Test specimen geometry (all dimension in mm)

4.3. Test Set-Up

The fatigue crack growth tests were performed on the MTS 250 kN, shown in Figure 4.2, at the Delft Aerospace Structures and Materials Laboratory (DASML) at a frequency of 10 Hz. The crack on one side is measured by a digital camera, which makes a picture every 2500 cycles². From this picture, in which measuring tape is included, the crack length is determined. The crack length on the other side of the specimen is measured by making use of Digital Image Correlation (DIC). The advantage of using DIC is that, in addition to the crack length, the delamination is also measured. Rodi et al. [48] describe that the delamination shape becomes visible when comparing the strain field of the specimen under static tension at 0 cycles (reference image) to the strain field of the specimen after a certain amount of cycles. The delaminated area does not carry any load and the positive residual strain in the metal layers is released, yielding a negative strain when comparing it to the reference image.

²For test 2 every 1000 cycles a picture is taken due to the small amount of cycles until failure. For test 3 every 1000 cycles a picture is taken after an overload is applied. 5000 cycles after the overload, the measurement interval is set again to 2500 cycles.

The digital camera and the DIC cameras are linked to each other and triggered at the same time to make measurements. When the pictures are taken, the maximum load is held for several seconds in order to have sharp pictures when the crack is best visible. A sketch of the entire test set-up is presented in Figure 4.3.

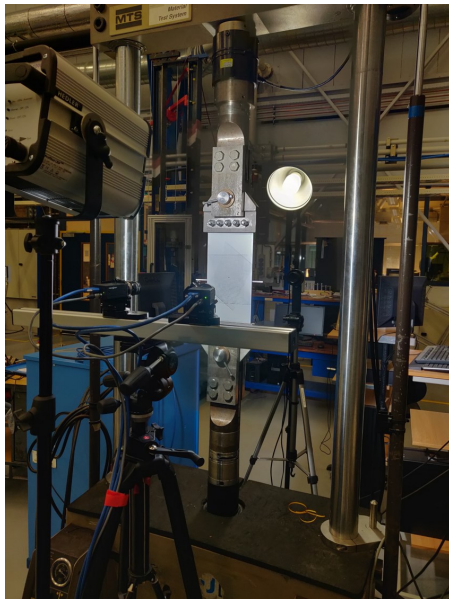


Figure 4.2: Test set-up (front view)

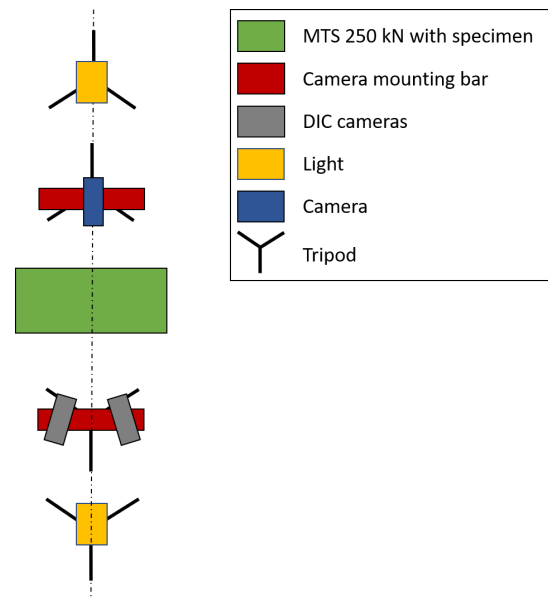


Figure 4.3: Test set-up sketch (top view)

The use of DIC requires additional preparation steps before testing can be done. The specimen is painted white and a black speckle pattern is applied. This process is illustrated in Figure 4.4, where the most left specimen is the end result of the specimen manufacturing as described in Section 4.2; the one to the right has the base paint layer sprayed on it; the next one is 'stamped' to apply the speckle pattern and the most right specimen shows how the specimen is bolted to the grips of the machine. From the deformation of the speckles, the strains in the specimen are computed.

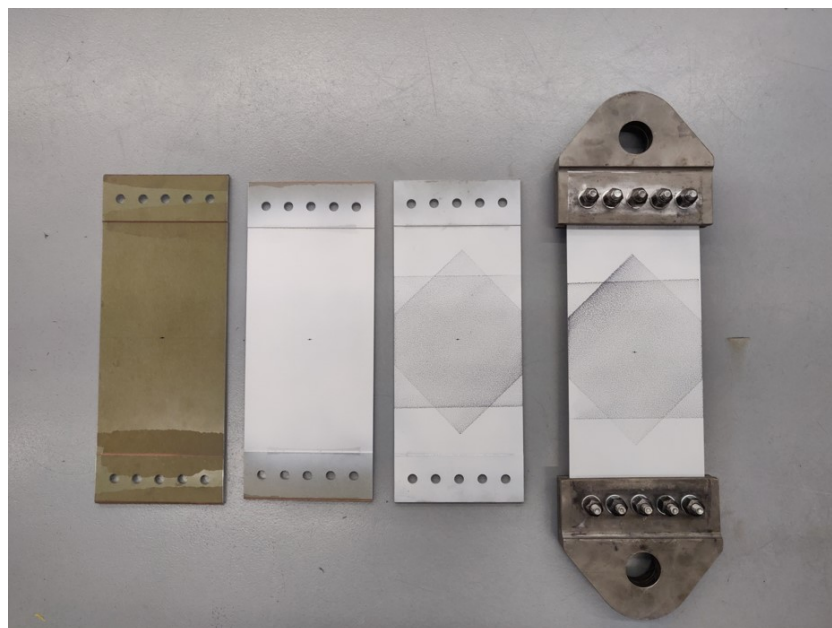


Figure 4.4: Different steps in specimen preparation for DIC

4.4. Post-Test Inspection

After testing, the outer aluminium layers are chemically etched in order to verify the DIC method described in Section 4.3. By removing the aluminium layers, which is done by submerging the specimen in a NaOH (sodium hydroxide) bath, the delaminations become visible. Voegesang [49] mentions that the speed at which the aluminium is removed, depends on multiple variable such as the concentration and temperature of the NaOH and the amount of dissolved aluminium. In order to speed up the process, only the damaged area of the test specimen is etched.

4.5. Results

This section presents the test results by evaluating the fracture angle and the crack growth curve at the front and rear side of the specimens and the delamination size and shape at the interface adjacent to the front side. The measured fracture angles of the different tests are summarised in Table 4.3. Due to the waviness of the crack, it is difficult to define one fracture angle, therefore the average of the largest and smallest fracture angle is stated in Table 4.3.

Table 4.3: Measured fracture angles of test specimens

Test ID	Front side		Rear side	
	Left	Right	Left	Right
Test 1	8°	7°	NA	NA
Test 2	0°	0°	0° (7°)*	0° (6°)*
Test 3	7°	8°	8°	7°
Test 4	7°	8°	7°	9°
Test 5	6°	5°	6°	7°
Test 6	0°	1°	2°	2°

*Crack does not have a constant fracture angle. Just before failure the crack curves. The magnitude of created angle is given between brackets.

The crack and delamination growth of each test are discussed separately in Section 4.5.1 to 4.5.4. Since the crack at the front side is evaluated with Vic3D, the post-processing tool of the DIC system, the crack length measurements are precise to the nearest 0.01 mm, while the crack length at the rear side, determined using measuring tape, is precise to the nearest 0.25 mm.

Important to note is that the horizontal length of the crack is measured as indicated in Figure 4.5. However, the model computes the actual crack length. To account for this difference the measured crack length is corrected by trigonometry such that a fair comparison can be made.

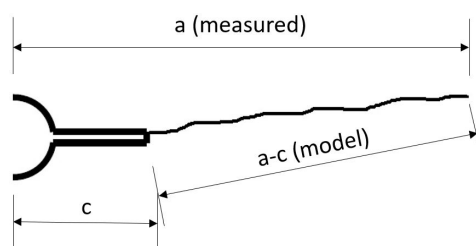


Figure 4.5: Crack length definitions

4.5.1. Test 1 & 2

The GLARE 2A tests are performed predominantly to measure the fracture angle. The specimen tested at an off-axis angle of 10° only showed a crack at one side of the specimen and none at the other side, even though 250 kcycles were applied. The reason why there is no crack present at the other side remains unclear.

Figure 4.6, which includes an infographic indicating the Point Of View (POV) with respect to the specimen, shows the cracks after 250 kcycles. A fracture angle of 8° and 7° is measured on the left and right side of the crack, respectively. The delamination around the crack is, due to the small crack length, not visible neither by the DIC method explained in Section 4.3 nor by the post-test inspection. The crack growth is depicted in Figure 4.7 showing a very slow crack growth, caused by the fibre bridging of the 6 prepreg plies oriented at a small off-axis angle.

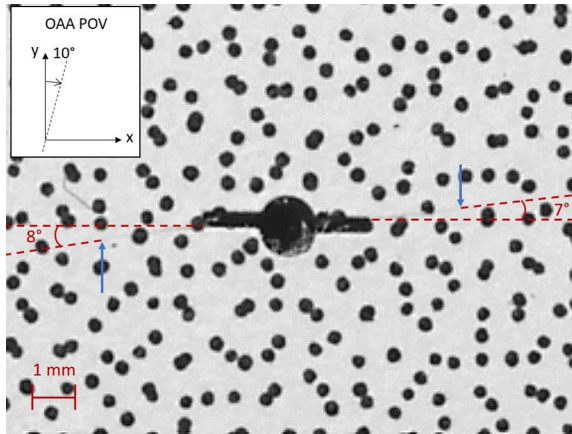


Figure 4.6: Test 1 crack size and orientation after 250 kcycles (blue arrows indicate crack tip)

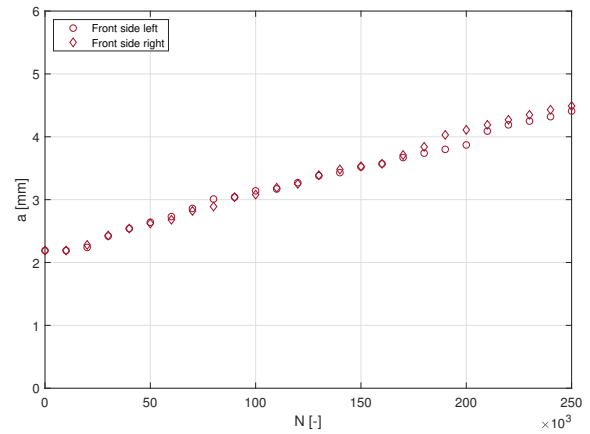


Figure 4.7: Test 1 crack growth data of specimen front side

The GLARE 2A specimen with an 80° off-axis angle failed after 28781 cycles. Figure 4.8 is taken at 28 kcycles and shows there is practically no fracture angle present, although the crack tips seem to curve after a certain crack length. The angles indicated in Figure 4.8 define the angle between the horizontal and the crack from the point the crack start to curve.

The crack growth presented in Figure 4.9 resembles the crack growth of a metal specimen, implying the fibre bridging at this off-axis angle is very limited or non-existing. This statement is substantiated with the absence of a delamination, as determined by both methods.

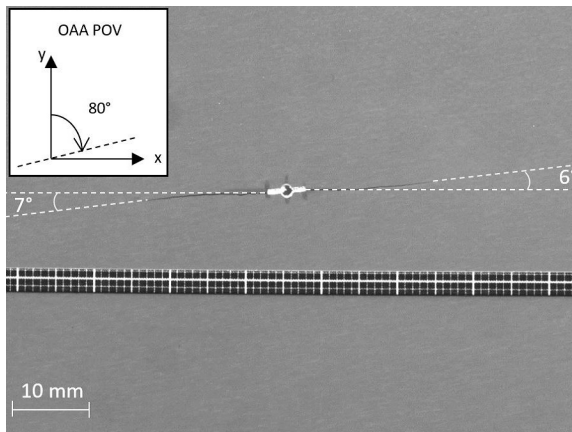


Figure 4.8: Test 2 crack size and orientation after 28 kcycles

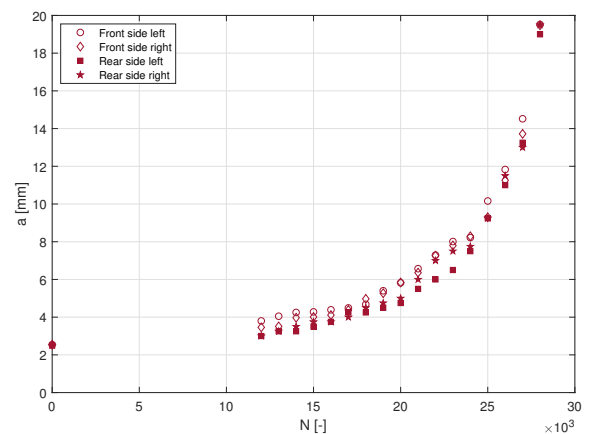


Figure 4.9: Test 2 crack growth data of specimen front and rear side

4.5.2. Test 3

Figure 4.10 shows the crack orientation and size of the GLARE 3 specimen, oriented at an off-axis angle of 22.5° and subjected to VA loading. The fracture angles at the front side are consistent with the fracture angles at the rear side, which also have a magnitude of 7° and 8° . The crack growth is presented in Figure 4.11 and the distinctive crack growth retardation after the application of the overloads (in Figure 4.11 indicated by OL) at 80, 120 and 160 kcycles is visible.

The delamination shape and size, determined by the DIC method, around the crack at the front side is visualised in Figure 4.12 by the white line. The theory stating that the delamination becomes visible when the positive residual strain in the metal layer is released (indicated by the negative strains), proves to be more difficult in practice. Not only the delaminated area shows negative strains, but also the areas above and below it, as observed in Figure 4.12. In order to locate the delamination boundary, the upper limit of the scale is set to 0 (only negative strains are made visible) and the lower limit of the scale is set at a low value and increased until a high gradient (made visible by the sequence of colours within a short distance) is noticed which indicates the delamination boundary.

The result after etching the metal layers is presented in Figure 4.13. At first sight, this figure shows a smaller delamination than presented in Figure 4.12. A comparison between these two figures is made in Section 5.2.2.

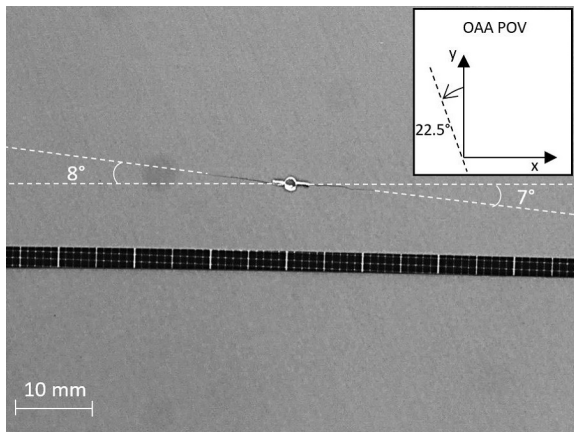


Figure 4.10: Test 3 crack size and orientation after 200 cycles

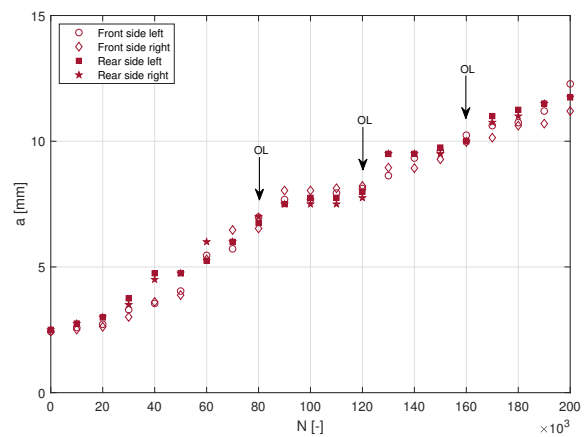


Figure 4.11: Test 3 crack growth data of specimen front and rear side

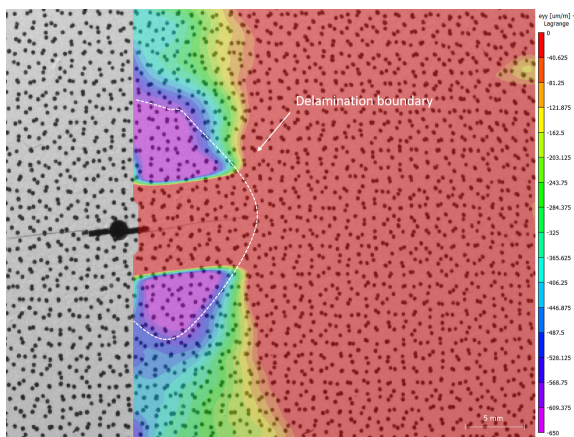


Figure 4.12: Test 3 strain field in longitudinal direction after 200 cycles

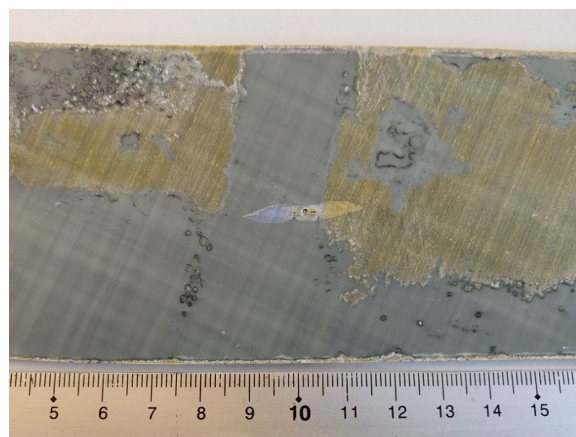


Figure 4.13: Test 3 delamination contour after 200 cycles (front side after etching)

4.5.3. Test 4 & 5

Two specimens were tested with the lay-up specified as Laminate 1 in Section 4.1: one with $S_{max} = 100$ MPa and the other with $S_{max} = 140$ MPa. The fracture angles of the two specimens are consistent as shown in Figure 4.14 and 4.15, albeit the magnitude in test 5 is somewhat smaller. The same method as discussed in Section 4.5.2 is used to locate the delamination boundary which is presented in Figure 4.16 and 4.17 for test 4 and 5, respectively. Both figures show that the delaminations around the crack seem to turn such that it grows transverse to the crack. A similar delamination shape is observed in Figure 4.18 and 4.19 for the two tests.

The crack growth curves of both tests are presented in Figure 4.20, where it can be noticed that the cracks at the front and rear side of test 4 have a different crack growth rate. This is peculiar since

the lay-up is symmetric. However, during testing the specimen was not located at the centre of the test machine and thereby created a small bending moment, causing a different stress in the front and rear metal layer. Test specimen 5 was properly aligned and shows an expected, equal crack growth behaviour. The cracks in test 5 evidently grow faster due to the higher applied load.

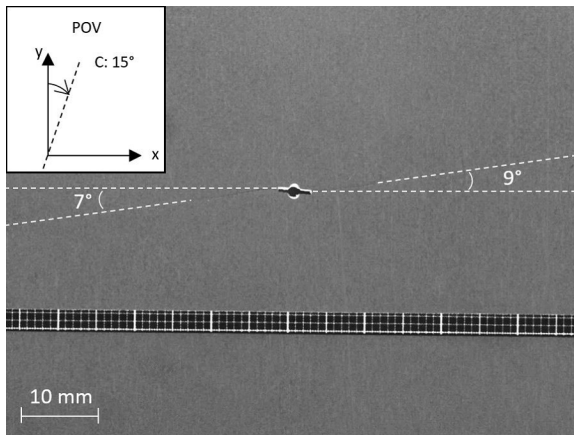


Figure 4.14: Test 4 crack size and orientation after 250 kcycles

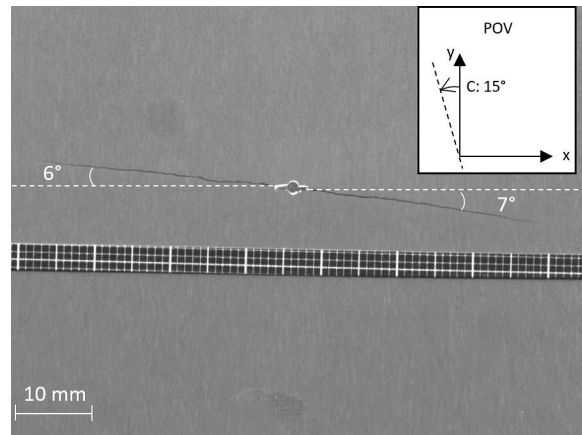


Figure 4.15: Test 5 crack size and orientation after 160 kcycles

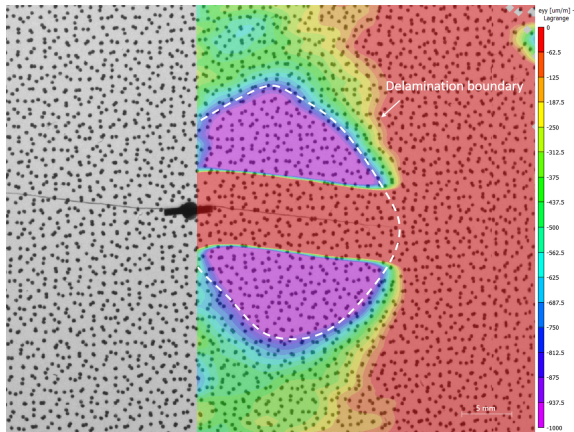


Figure 4.16: Test 4 strain field in longitudinal direction after 250 kcycles

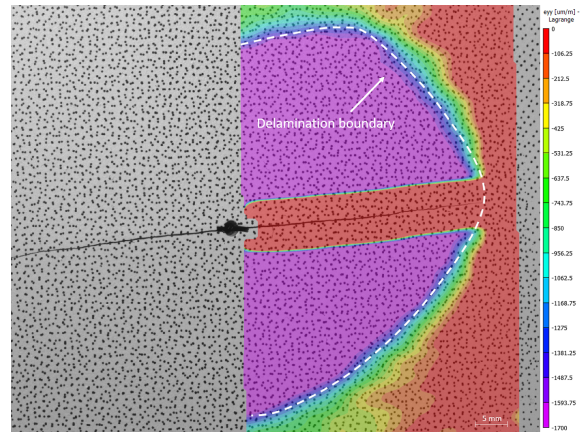


Figure 4.17: Test 5 strain field in longitudinal direction after 160 kcycles

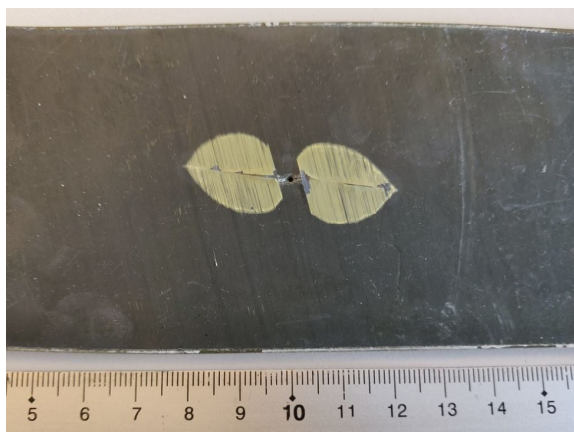


Figure 4.18: Test 4 delamination contour after 250 kcycles (front side after etching)



Figure 4.19: Test 5 delamination contour after 160 kcycles (front side after etching)

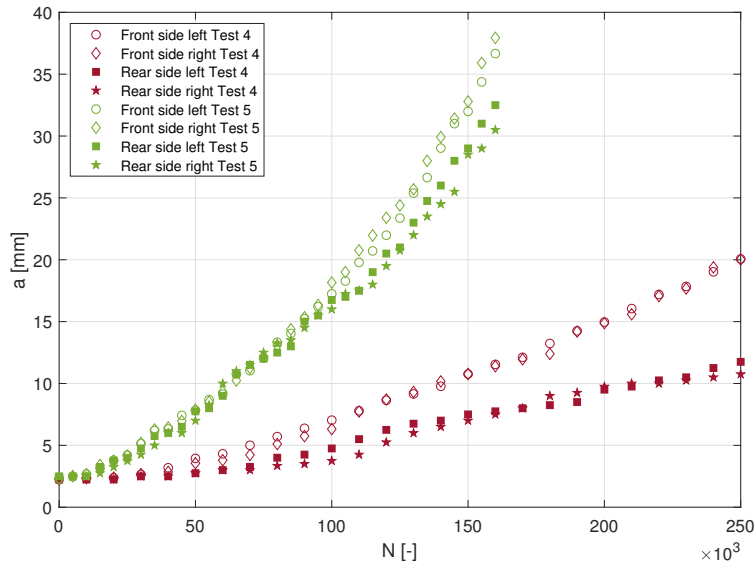


Figure 4.20: Test 4 and 5 crack growth data of specimen front and rear side

4.5.4. Test 6

Laminate 2 has an asymmetric lay-up as defined in Section 4.1. Figure 4.21 and 4.22 show the cracks at the front and rear side, respectively. From these figures it can be seen that the fracture angles are not equal. The cracks at the front side have (almost) no fracture angle (supported by the symmetric delamination shape in Figure 4.23 and 4.24), while the cracks at the rear side have a fracture angle of 2° .

The crack growth rate at the front side of the specimen is larger than at the rear side as depicted in Figure 4.25. There is expected to be a minor difference since the neutral axis does not coincide with the laminate’s mid-plane. The neutral axis is the through the thickness location in the laminate where the strain in x -direction is zero under the application of a moment M_x [17]. Using this assumption gives

$$\bar{z} = -\frac{b_{11}}{d_{11}} \tag{4.1}$$

Filling in Equation 4.1 for Laminate 2 gives a 0.06 mm offset between the NA and the laminate mid-plane towards the front side. This creates a (small) moment causing the stress in the rear metal layer to increase and the stress in the front metal layer to decrease. However, the opposite is noticed in the test data. The large difference and the opposite from expected crack lengths, suggests that this specimen, similar to test specimen 4, has been misaligned with the load cell in the test machine.

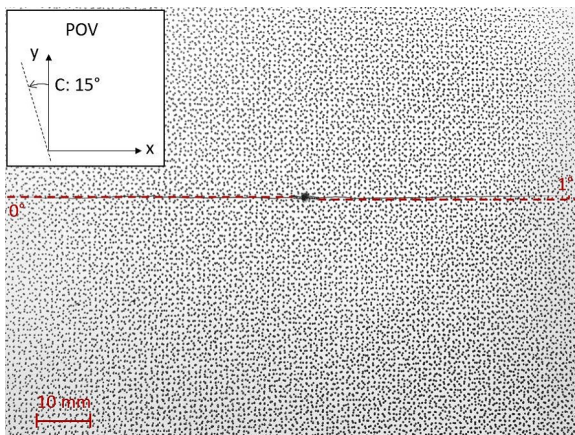


Figure 4.21: Test 6 crack size and orientation after 250 kcycles (front side)

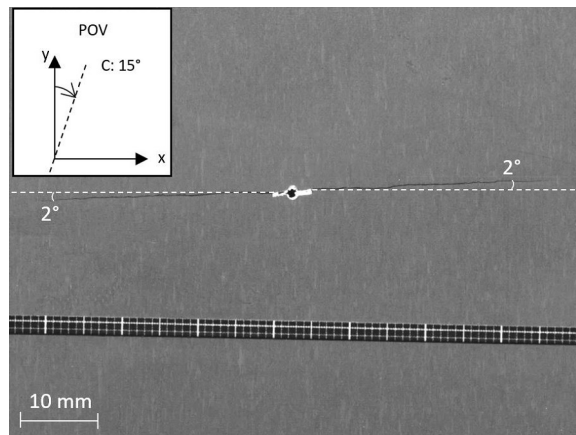


Figure 4.22: Test 6 crack size and orientation after 250 kcycles (rear side)

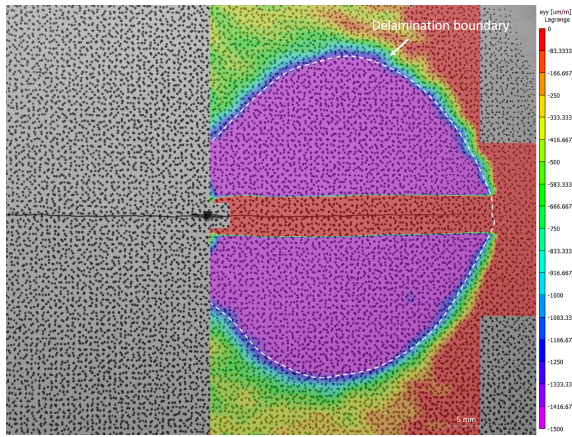


Figure 4.23: Test 6 strain field in longitudinal direction after 250 cycles

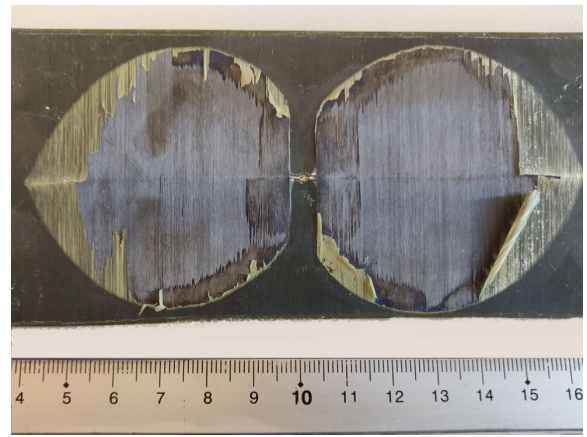


Figure 4.24: Test 6 delamination contour after 250 cycles (front side after etching)

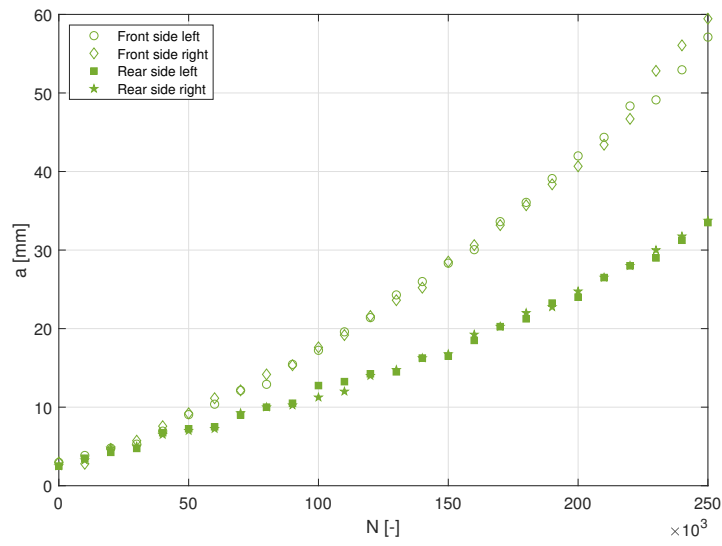


Figure 4.25: Test 6 crack growth data of specimen front and rear side

5

Verification and Validation

Two types of checks must be carried out before it can be stated that the model is capable of predicting fatigue crack growth and damage directionality in non-conventional FMLs. The first one is called verification, discussed in Section 5.1, and is performed to ensure the model is built correctly. The second check is called validation, as treated in Section 5.2, during which it is determined whether the model represents reality accurately enough.

5.1. Verification

Large parts of the model have already been verified by Wilson [17] and Spronk [13]. Therefore, only the newly added parts, i.e. the blue boxes in Figure 3.3 and 3.12, are verified. To check whether these individual parts function appropriately, so-called unit tests are performed which are described in Section 5.1.1. In Section 5.1.2 system tests are executed to check whether the new parts have been implemented correctly into the existing model.

5.1.1. Unit Tests

Since the code for mode II is built in analogy to mode I, meaning that the same initialisation applies, the vectors and matrices used for mode II are of the same size as the ones for mode I, thereby eliminating syntax errors. Furthermore, it is of utmost importance to check whether every addition to the original code is coded correctly, which is done by the following criteria:

1. Check if the correct variable is used in the equation.
 - (a) Check if changing parameters will give the expected change.
 - E.g.: Compare the induced shear stress for GLARE 3 at the off-axis angle of 10° and 20° . If programmed correctly, the induced shear stress should be higher at 20° than at 10° , which results in a larger mode II SIF.
 - (b) Check singularities.
 - E.g.: GLARE 3 at an off-axis angle of 45° (a balanced laminate) should have a zero mode II SIF and as a consequence, the fracture angle should be zero as well.
2. Check if the calculated parameters have the same units as their mode I counterpart.

5.1.2. System Tests

Two system tests concerning input processing are performed to check whether the off-axis angles and the angles in the laminate lay-up are correctly processed. In the first test a GLARE 3-4/3-0.4 laminate with a positive and negative off-axis angle of 10° is simulated. If modelled correctly, the number of cycles corresponding to a crack length of 10 mm, should be equal for both cases, while the fracture angle should be opposite.

The second test comprises the comparison between two GLARE 3-4/3-0.4 laminates: one where the angles in the lay-up definition are increased by 10° and no off-axis is added, and the other where

no angles are altered in the lay-up definition, but an off-axis angle of 10° is used. The output of both models should be equal, which is the case as shown in Table 5.1.

Table 5.1: Input system test verification

Test	$N_{a=10mm}$ [-]	Fracture angle [°]
Off-axis angle = + 10°	166294	3.1
Off-axis angle = - 10°	166294	-3.1
Lay-up angles + 10° and 0° off-axis angle	166294	3.1

As a last test, the original code from Wilson [17] and the modified code are compared by simulating the crack growth rate for the same laminate under the same conditions. The crack growth rate for the original model and for the modified model for GLARE 2A-4/3-0.4 is shown in Figure 5.1 and 5.2, respectively. The curves in these two figures show a similar behaviour concerning the crack growth rate. For a GLARE 4B-4/3-0.4 laminate, the crack growth rate simulated by the original model, seen in Figure 5.3, is slightly higher than the crack growth rate computed by the modified model as seen Figure 5.4. The reason for this discrepancy is because the 90° fibre layer in the modified model is treated as a fibre layer, whereas in the original model it is seen as an adhesive layer.

This test in conjunction with the unit tests and other system tests proves that the modified model is functioning as intended and thus is verified.

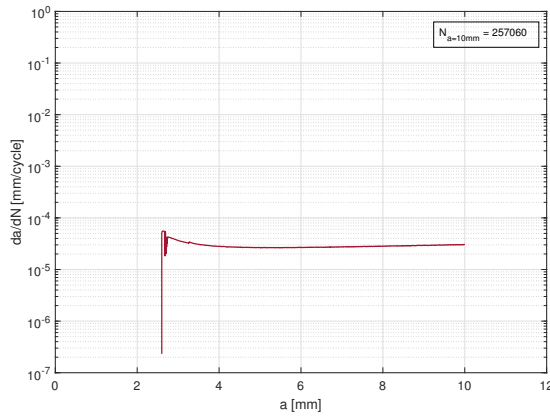


Figure 5.1: Crack growth rate prediction of the original model for GLARE 2A-4/3-0.4 under $S_{max} = 100$ MPa and $R = 0.05$ at $OAA = 0^\circ$

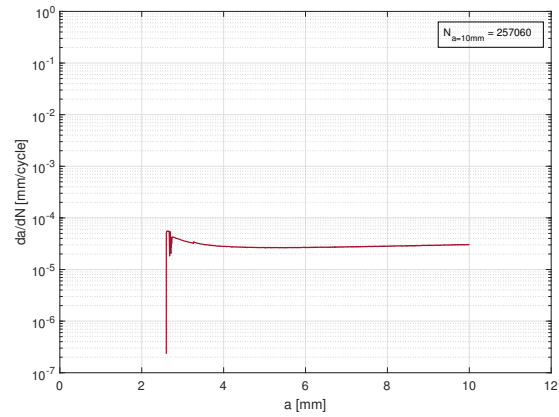


Figure 5.2: Crack growth rate prediction of the modified model for GLARE 2A-4/3-0.4 under $S_{max} = 100$ MPa and $R = 0.05$ at $OAA = 0^\circ$

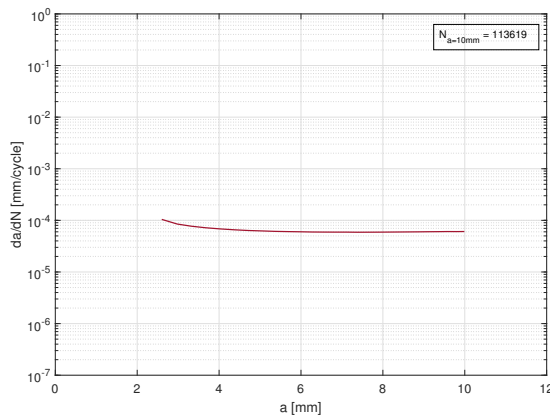


Figure 5.3: Crack growth rate prediction of the original model for GLARE 4B-4/3-0.4 under $S_{max} = 100$ MPa and $R = 0.05$ at $OAA = 0^\circ$

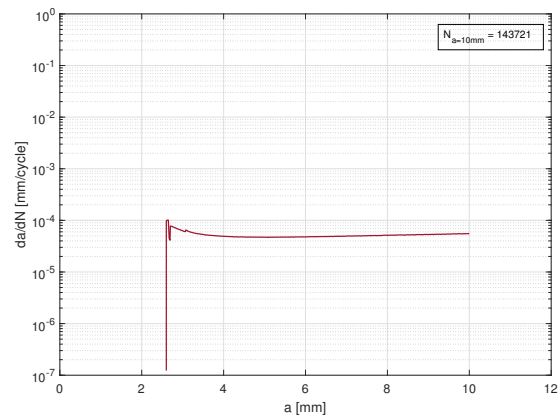


Figure 5.4: Crack growth rate prediction of the modified model for GLARE 4B-4/3-0.4 under $S_{max} = 100$ MPa and $R = 0.05$ at $OAA = 0^\circ$

5.2. Validation

The model, as described in Chapter 3, is evaluated by comparing test data with the model's prediction to check whether the model is capable of predicting fatigue crack propagation and directionality of damage in non-conventional FMLs. In Section 5.2.1 the outcome of the model is compared to test data from literature. The comparison between the data obtained from the tests discussed in Chapter 4 and the predictions of the model is presented in Section 5.2.2. The validation is treated in this order for the purpose of building up the number of non-conventional characteristics, as demonstrated in Table 4.2.

5.2.1. Legacy Test Data

Gupta

Gupta [31] validated his model concerning damage directionality by performing tests with various off-axis angles on GLARE 3, GLARE 4B and GLARE 2A at a maximum stress of $S_{max} = 100$ MPa and a stress ratio of $R = 0.05$. Gupta [31] observed that the crack first propagates without deflection for 0.5 mm which is solely attributed to the stress concentration factor. After this 0.5 mm, the crack deflects due to the off-axis fibres which start to bridge the crack. This process is modelled similarly by setting the starting crack 0.5 mm larger than the initial notch size. To eliminate the effect of initial conditions, the data point from the second iteration is taken.

Gupta [31] indicates it is difficult to measure the exact fracture angle due to the waviness of the crack, wherefore error bars are included in Figures 5.5 - 5.7. The fracture angles measured from the test specimens from Gonesh [34, 40] are also included in these figures.

Figure 5.5 presents the test results for GLARE 3-4/3-0.4 in conjunction with the prediction by Gupta's model and the prediction by the model described in Chapter 3. The fracture angle is zero at 45° which is logical since at 45° the laminate is balanced, resulting only in a mode I SIF. Furthermore, point symmetry around 45° is present, meaning that the fracture angles at for example 22.5° and 67.5° have the same magnitude but a different sign. The crack propagation in opposite direction is caused by the same amount of rotation of the fibres with respect to the loading, i.e. for GLARE 3 an off-axis angle of 67.5° is the same as -22.5° .

Comparing the two predictions in Figure 5.5 shows that they have the same shape, although the prediction by Gupta has larger absolute values. Gupta's prediction overestimates the fracture angles, whereas the current model's prediction lies closer to the measured values.

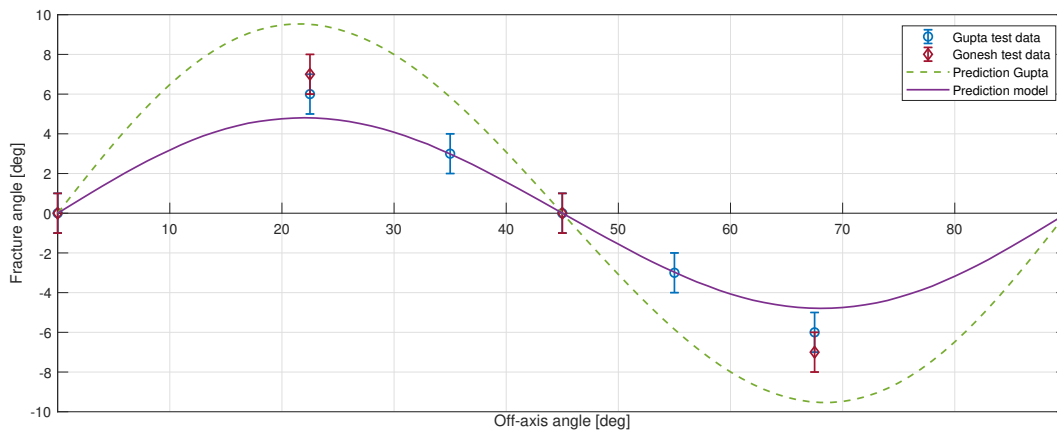


Figure 5.5: Fracture angle comparison between test data and prediction for GLARE 3-4/3-0.4 [31]

Where a fracture angle of 0° is observed at an off-axis angle of 45° for GLARE 3, GLARE 4B shows this at an off-axis angle of 60° as seen in Figure 5.6. This behaviour is explained by the fact that GLARE 4B has twice as many fibres oriented in a 60° direction with respect to the loading axis than in 30° direction.

A similar trend between the two predictions is observed in Figure 5.6, being the same shape, but having a different magnitude. The model of Gupta overestimates the fracture angle, while the current model's prediction lies within the error margin of most data points.

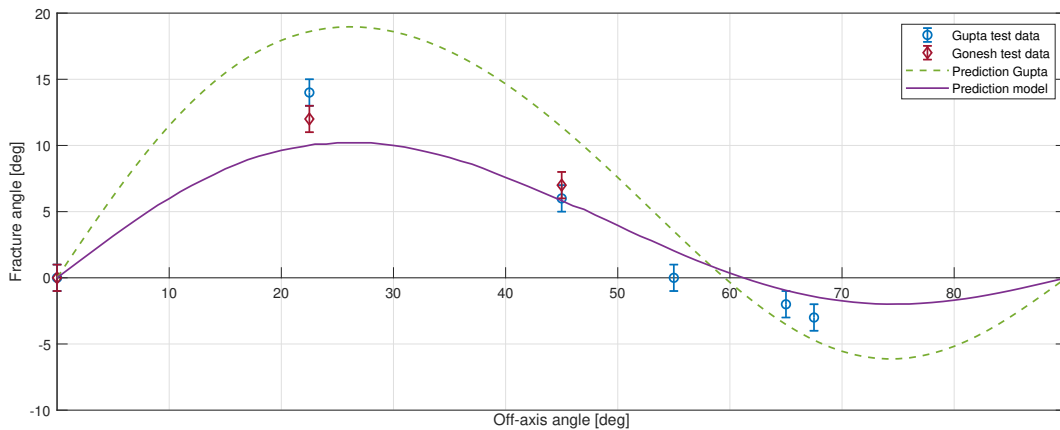


Figure 5.6: Fracture angle comparison between test data and prediction for GLARE 4B-4/3-0.4 [31]

Whereas the shape between the two predictions for GLARE 3 and GLARE 4B are similar, this is not true for GLARE 2A as shown in Figure 5.7. For both models, the prediction lines shown in Figure 5.7 are the negative values of the model's output. A justification for doing this, is that cracks grow in the direction giving the least resistance; however, it remains unclear why the model gives correct predictions for GLARE 3 and GLARE 4B, but not for GLARE 2A.

Despite this small tweak, the model by Gupta is outperformed by the current model since the latter lies closer to the test data. As mentioned in Section 4.1.2, the models seem to overestimate the fracture angle at large off-axis angles.

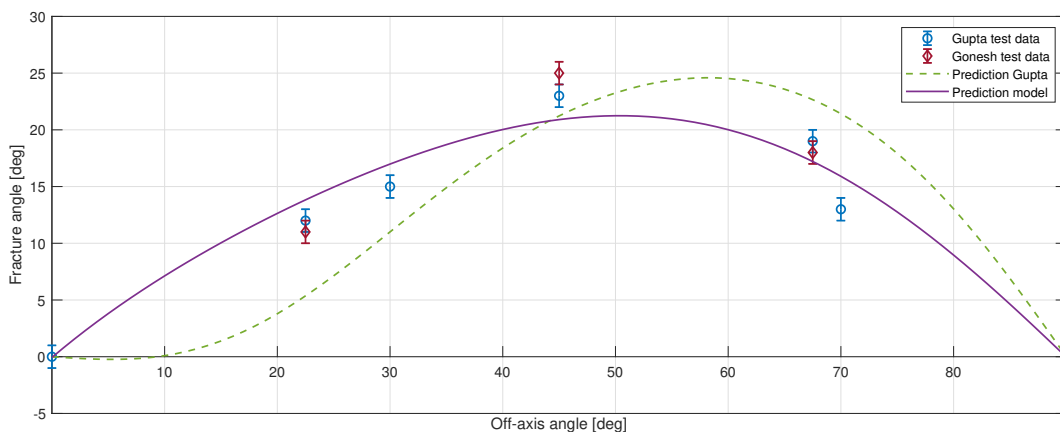


Figure 5.7: Fracture angle comparison between test data and prediction for GLARE 2A-4/3-0.4 [31]

The reason why this model's prediction is a 'damped' version of Gupta's prediction as shown in Figure 5.5 and 5.6, is the different method of calculating the induced shear stress. Equation 3.2 yields a larger shear stress than Equation 3.1, resulting in a larger K_{II} with the effect that the fracture angle increases as well.

Gonesh

Gonesh [34, 40] performed fatigue crack growth tests on GLARE specimens under various off-axis angles and multiple load spectra. The most interesting comparisons between test data and the model's prediction for multiple GLARE grades are presented here; however, more comparisons are included in Appendix B. Table B.1 in Appendix B relates the labels used by Gonesh [34, 40] to the data presented in this section to ensure data traceability.

The specimens used by Gonesh have two notches where cracks initiate from, as depicted in Figure 5.8 [34]. When presenting the test data from Gonesh [34, 40], the data are labelled as *upper crack* and *lower crack* to indicate the spread of the test data. Figure 5.8 also depicts how the crack length, being the horizontal distance between the two crack tips, is measured. Since the model assumes a

straight crack, but in fact calculates the actual length of the crack, the data points from Gonesh [34, 40] are corrected by trigonometry in same manner as explained in Section 4.5. In addition, it is assumed that the crack length ($2a$) has two equal parts, allowing the test data from Gonesh to be divided by two to obtain the half crack length.

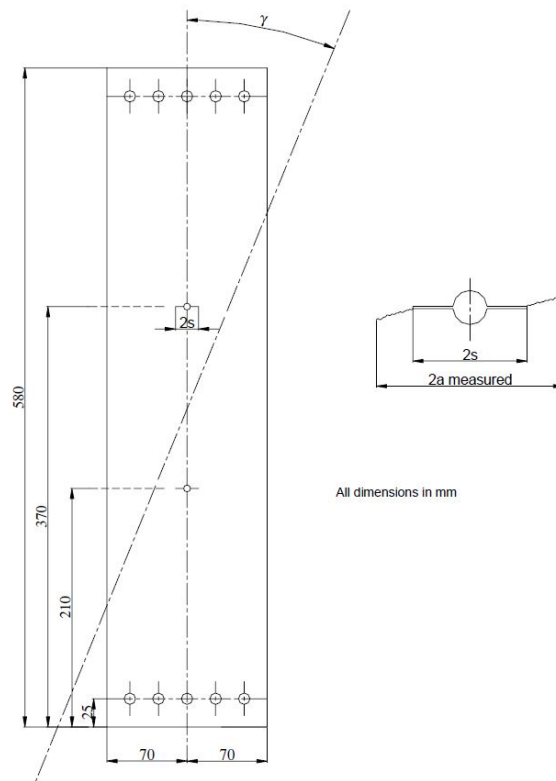


Figure 5.8: Specimen geometry tested by Gonesh [34]

GLARE 3-4/3-0.4 specimens under a 45° off-axis angle are balanced and therefore do not have an induced applied shear stress. Figure 5.9 and 5.10 present a comparison between test data and the model's prediction for the crack growth and the crack growth rate, respectively. The prediction for $S_{max} = 100$ MPa shows an excellent fit with the test data, while the prediction for the other two load conditions is somewhat on the conservative side. The kink in the $S_{max} = 120$ MPa prediction curve around 160 kcycles is caused by the FWCF.

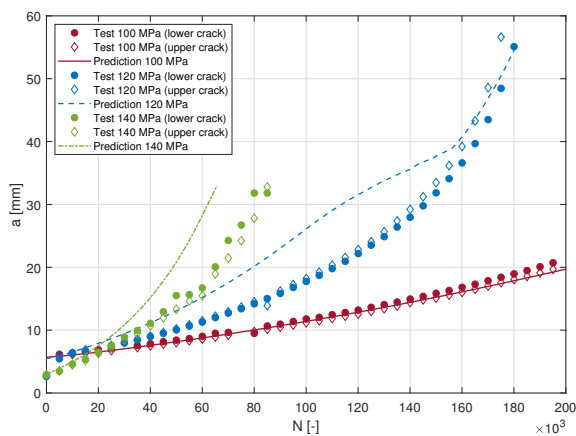


Figure 5.9: Comparison between crack growth test data and crack growth prediction for GLARE 3-4/3-0.4 at $OAA = 45^\circ$ [34, 40]

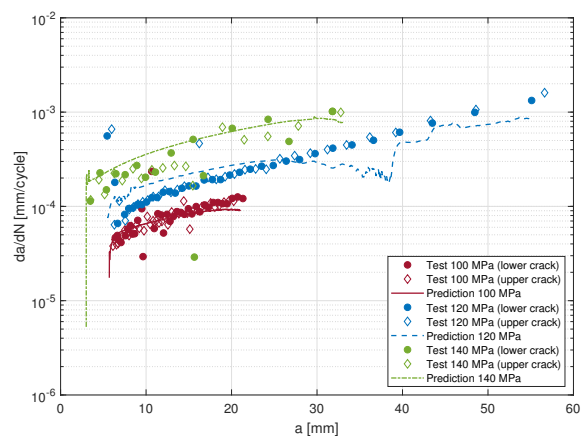


Figure 5.10: Comparison between crack growth rate test data and crack growth rate prediction for GLARE 3-4/3-0.4 at $OAA = 45^\circ$ [34, 40]

Contrary to a GLARE 3 specimen, a GLARE 4 specimen is not balanced at an off-axis angle of 45° , meaning that the induced shear stress is non-zero. Figure 5.11 and 5.12 show that this does not provide difficulties for the model since the predictions and test data match.

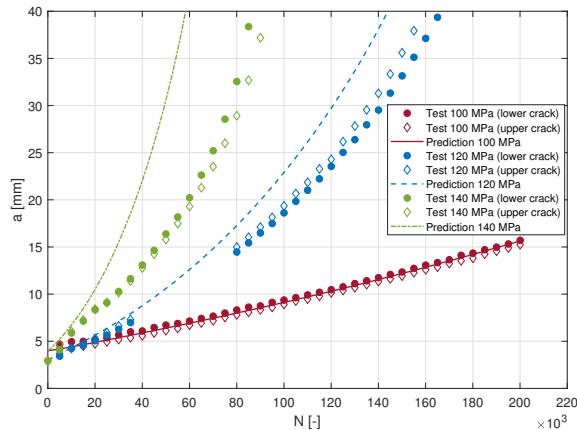


Figure 5.11: Comparison between crack growth test data and crack growth prediction for GLARE 4B-4/3-0.4 at $OAA = 45^\circ$ [34, 40]

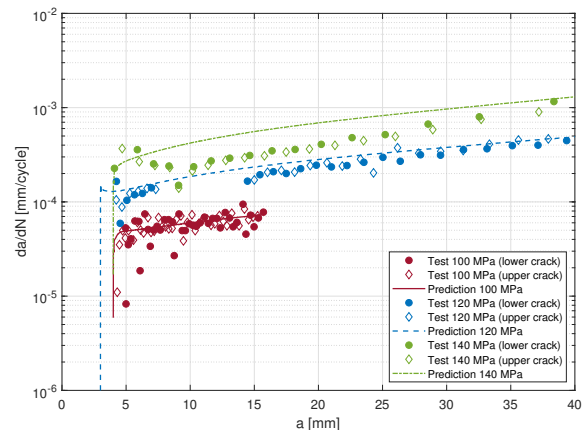


Figure 5.12: Comparison between crack growth rate test data and crack growth rate prediction for GLARE 4B-4/3-0.4 at $OAA = 45^\circ$ [34, 40]

Figure 5.13 and 5.14 present similar comparisons concerning GLARE 5. Where the same trend is followed between test data and predictions for GLARE 3 and GLARE 4B under a load of $S_{max} = 140$ MPa, this cannot be stated for GLARE 5. However, one can question whether the prediction or test data is incorrect, since the crack growth rate test data for $S_{max} = 120$ and 140 MPa are equal.

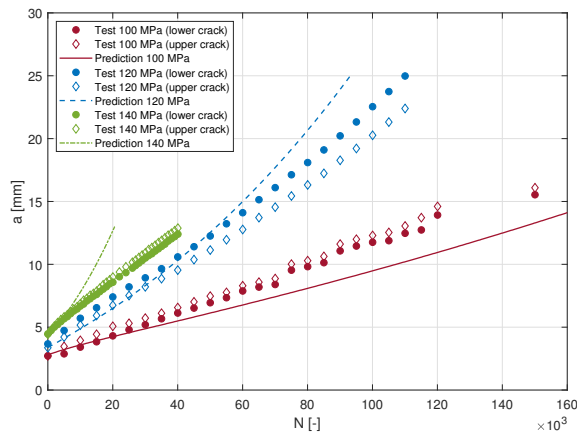


Figure 5.13: Comparison between crack growth test data and crack growth prediction for GLARE 5-4/3-0.4 at $OAA = 45^\circ$ [34]

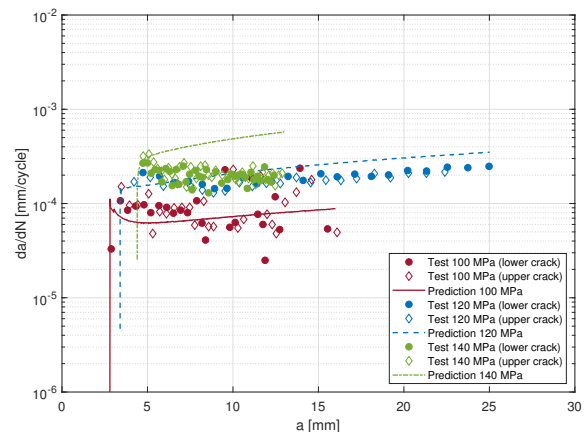


Figure 5.14: Comparison between crack growth rate test data and crack growth rate prediction for GLARE 5-4/3-0.4 at $OAA = 45^\circ$ [34]

Whereas the previously discussed GLARE grades all contained cross-ply, GLARE 2A only contains UD plies, which provides some difficulties. The model's prediction is inaccurate for such a lay-up under an off-axis angle of 45° , as presented in Figure 5.15. The inaccuracy is caused by an overestimation of the bridging load at large off-axis angles indicated by the small delamination size around the crack in Figure 5.16. To take this into account, the bridging load is factorised by the ratio of the stiffness of the fibre orientation in loading direction and its maximum stiffness. Down-scaling the bridging load results in a faster crack growth as observed in Figure 5.15.

In a second attempt to create a better fit between test data and prediction, the assumption concerning the bridging angle (assumption 14 in Section 3.1.2) is ignored. However, Figure 5.15 shows that this adaptation does not make a difference and is therefore disregarded in future predictions. Especially because the computational time doubles as the bridging terms from Equation 3.22 and 3.49 are computed twice: once for the bridging angle under minimum load and once for the bridging angle

under maximum load.

Applying this method to other load spectra gives similar results as presented in Figure 5.17. The remaining gap between the test data and prediction is presumably caused by the high fracture angles, making the Westergaard stress functions for horizontal cracks less valid to use.

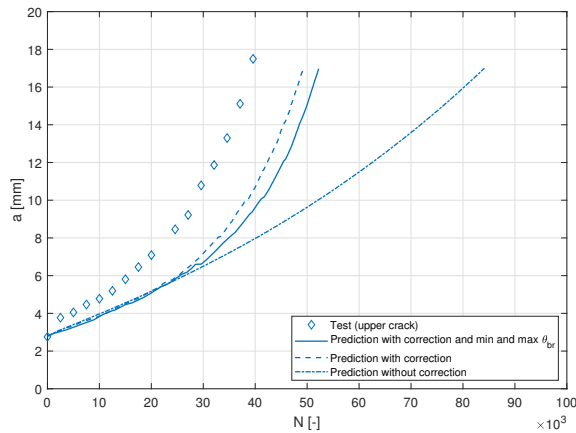


Figure 5.15: Comparison between crack growth test data and different methods to predict crack growth for GLARE 2A-4/3-0.4 under $S_{max} = 120$ MPa and $R = 0.05$ at $OAA = 45^\circ$ [34]



Figure 5.16: Delamination around the crack of a GLARE 2A specimen under $S_{max} = 140$ MPa and $R = 0.05$ at $OAA = 45^\circ$ [34]

Interesting to note is that when smaller off-axis angle are used ($OAA = 0^\circ - 22.5^\circ$), the correction factor is not necessary since the model already predicts the crack growth accurately as presented in Figure 5.18. This implies that within the practical range of FMLs with only UD plies (designing a UD FML which is not oriented in the main loading direction is not desirable), such as GLARE 2A, the model without correction factor is valid.

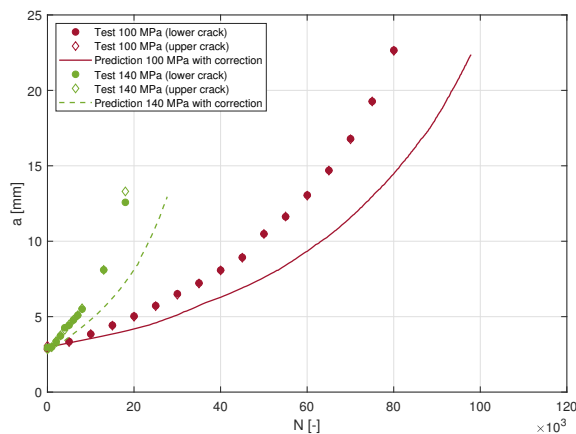


Figure 5.17: Comparison between crack growth test data and crack growth prediction for GLARE 2A-4/3-0.4 at $OAA = 45^\circ$ [34]

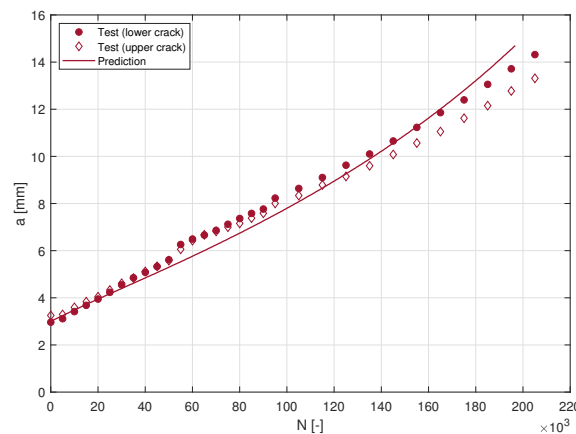


Figure 5.18: Comparison between crack growth test data and crack growth prediction for GLARE 2A-4/3-0.4 under $S_{max} = 100$ MPa and $R = 0.05$ at $OAA = 22.5^\circ$ [34]

Two tests with metal laminates under different off-axis angles are performed by Gonesh [34]. In Appendix C various methods to simulate MLs are outlined. Since the adhesive layers crack together with the metal layers, the method where the bridging load is set to 0 is deemed to be most suitable [34]. Figure 5.19 presents the test data of the two tests: one test performed at an off-axis angle of 22.5° and the other at an off-axis angle of 45° . Since no fibres are present, the only difference between the two tests is the orientation of the rolling direction of the aluminium with respect to the loading direction. However, judging by the test data of the two tests, the fatigue properties under $OAA = 22.5^\circ$ and $OAA = 45^\circ$ are

similar. As stated in assumption 3 (Section 3.1.2), the model ignores the effects of anisotropy of the metal layers on the mechanical and fatigue properties, resulting in identical predictions of the two tests.

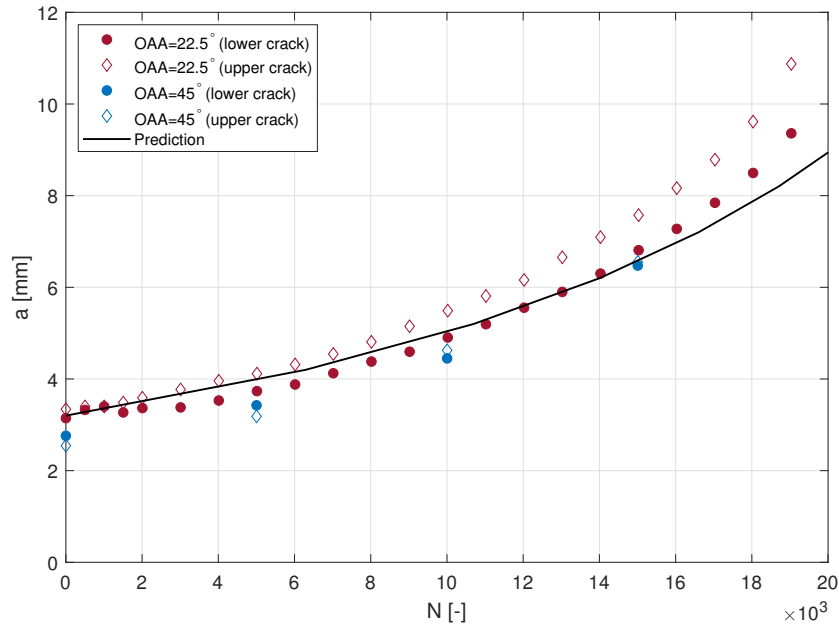


Figure 5.19: Comparison between crack growth test data and crack growth prediction for Al-4/0-0.4 under $S_{max} = 100$ MPa and $R = 0.05$ [34]

Rensma

Rensma [44] manufactured several non-conventional FMLs consisting of a steel-carbon core and aluminium outer layers attached to the core by the same glass fibre prepreg as in GLARE. As further specified in Figure 5.20, lay-up C, E and E2 have an additional FM94 adhesive layer between the aluminium and the glass fibre prepreg to improve delamination behaviour [44].

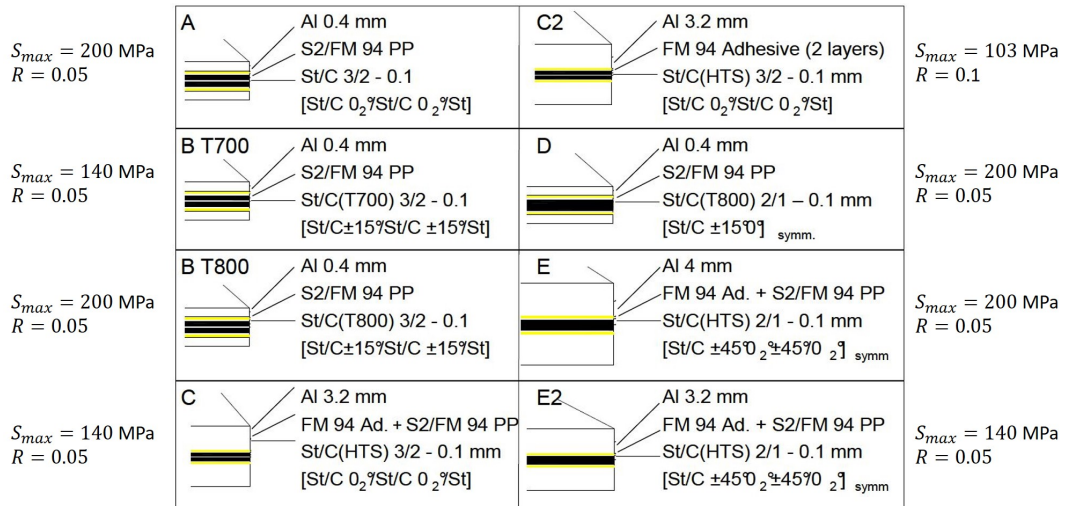


Figure 5.20: The specimen lay-ups used by Rensma [44]

The mechanical properties of the materials are provided by Rensma [44]; however, the crack growth parameters (C_{cg} and n_{cg}) are unknown for the type of Stainless Steel used (Sandvik 11R51). For that reason the values from a similar Stainless Steel type are used¹. The delamination parameters (C_d and

¹<https://www.efatigue.com/constantamplitude/crackgrowth/materials/>; AISI 316

n_d) of the carbon fibre prepreg, which are mostly defined by the resin type, are also unknown. The type of resin used is FM94 which is the same resin wherein the glass fibres are embedded in GLARE. Therefore, Rensma [44] used the same exponent (n_d), but changed the coefficient (C_d) to get a closer match with test data. The same procedure is applied here, with the following difference: for validation one value is selected ($C_d = 0.8$) while Rensma used a different value for C_d for each specimen.

The lay-ups are divided into thin (A, B-T700, B-T800 and D) and thick (C, C2, E and E2) laminates. The thin laminates contain some differences: laminate B-T700 and B-T800 have the same lay-up, but differ in the fibre type used. Laminate B-T700 is a variation of laminate A, where the fibres are oriented under a $\pm 15^\circ$ angle instead of under 0° . Finally, in laminate D the middle steel layer is replaced by 2 carbon plies oriented in the loading direction.

Figure 5.21 presents the comparison of the crack growth rate between the test data and the prediction for laminate A and B-T700. The crack growth rate prediction for laminate A is slightly higher than the test data, but the trend is the same. The prediction for laminate B-T700 is closer to the test data, although the higher crack growth rate for small crack lengths is not captured.

The crack growth rate test data for laminate B-T800 and D have an equal magnitude as depicted in Figure 5.22; however, their predictions vary. The steel layer in laminate B-T800 does not contribute to the bridging load in the model, while the two carbon fibre layers in laminate D do. It is therefore logical that a lower crack growth rate is predicted for laminate D; however this is not observed in test data.

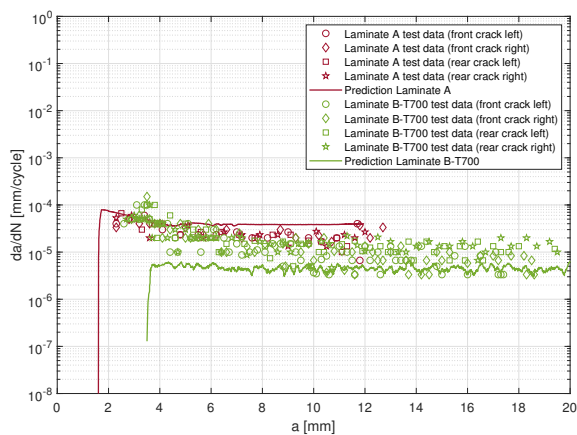


Figure 5.21: Comparison between crack growth rate test data and crack growth rate prediction (laminate A and B-T700) [44]

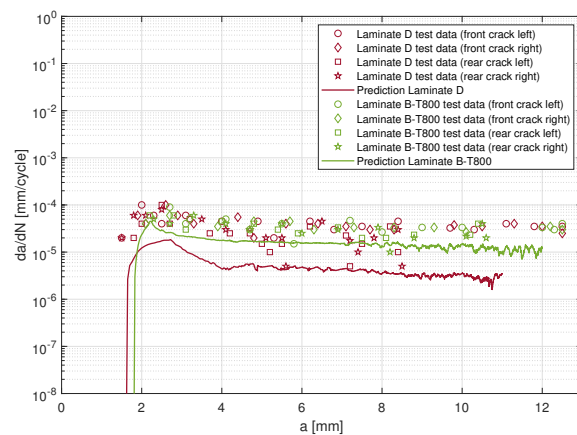


Figure 5.22: Comparison between crack growth rate test data and crack growth rate prediction (laminate B-T800 and D) [44]

In general, the thick laminates show a more metal-like behaviour concerning crack growth in the outer layer due to their relative thickness compared to the core. Laminate C, C2, E and E2 in Figure 5.20 are considered to be thick laminates, where laminate C2 is a variation of laminate C (the glass fibre prepreg has been replaced by an adhesive layer) and laminate E and E2 differ in the outer layer thickness.

The crack growth rate predictions for specimen C and C2 have the same trend as the test data, but a lower magnitude as observed in Figure 5.23. The error is explained by the large delaminations at the steel interfaces, depicted in Figure 5.25. These delaminations extend further than the crack tips; something the model is not capable of simulating which consequently means that the bridging load in reality is substantially smaller than calculated in the model, yielding a higher crack growth rate. Similar delamination behaviour is found in the C2 specimen, explaining the mismatch in test data and prediction.

The large delaminations, as seen in Figure 5.25, are not present in the specimens with lay-up E and E2 [44]. However, the model predicts very small crack length in the steel layers and as a consequence small delaminations around them, resulting in higher bridging loads than present in reality. It is believed that with the correct material inputs, the difference between the test data and prediction will be smaller than presented in Figure 5.24.

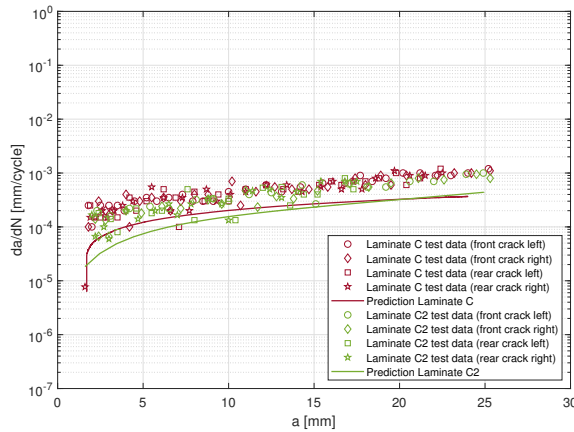


Figure 5.23: Comparison between crack growth rate test data and crack growth rate prediction (laminates C and C2) [44]

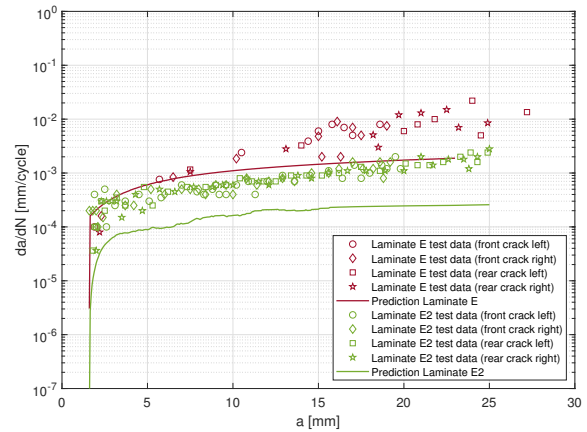


Figure 5.24: Comparison between crack growth rate test data and crack growth rate prediction (laminates E and E2) [44]

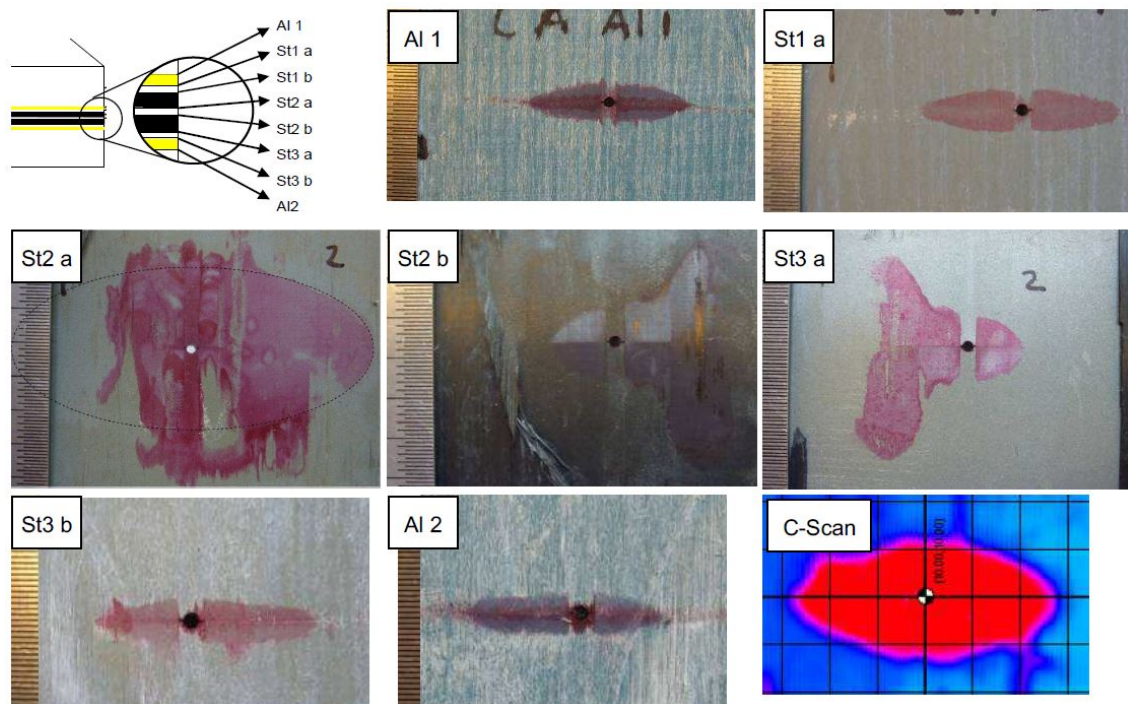


Figure 5.25: Delamination indicated in red for all interfaces in specimen C after 64 kcycles [44]

5.2.2. Current Test Data

In this section, the results from the performed tests discussed in Section 4.5 are compared to the model's prediction.

Test 1 and 2

The main purpose of performing test 1 and 2 is to measure the fracture angle. Test specimen 1 has a fracture angle of 7.5° on average, which is somewhat overpredicted by the model as can be seen in Table 5.2. However, the prediction of this model lies closer to the test data than the zero fracture angle predicted by Gupta's model (Figure 5.7).

In test specimen 2, the crack curves towards the orientation of the fibres just before failure. However, the fracture angle is measured to be zero for more than 90% of the fatigue life. This confirms the trend that the fracture angle rapidly decreases once the off-axis is higher than 70° as observed in Figure 5.7; something which is not captured by the model.

Table 5.2: Fracture angle comparison between data from test 1 and 2 test and prediction

Test ID	Front side		Rear side		Prediction
	Left	Right	Left	Right	
Test 1	8°	7°	NA	NA	8.8°
Test 2	0°	0°	0°	0°	8.9°

Note: The predicted angles are the opposite number from what the model predicts (similar to Figure 5.7)

The crack growth prediction for test 1 is on the conservative side as depicted in Figure 5.26. The slower crack growth in the test data is probably caused by the uncracked metal layer at the rear side of the specimen. During testing, the rear metal layer bridges the crack in the front metal layer, while in the model a crack in the rear metal layer is present as would be expected.

Test 2 indicates that the model does not provide an accurate prediction for a UD FML under an off-axis angle of 80°. The fracture angle prediction as well as the fatigue crack growth prediction, even with the correction factor proposed in Section 5.2.1, do not lie close to the test data. The presumption that the laminate behaves as a metal due to the high off-axis angle, is confirmed when setting the bridging load to zero as depicted in Figure 5.27.

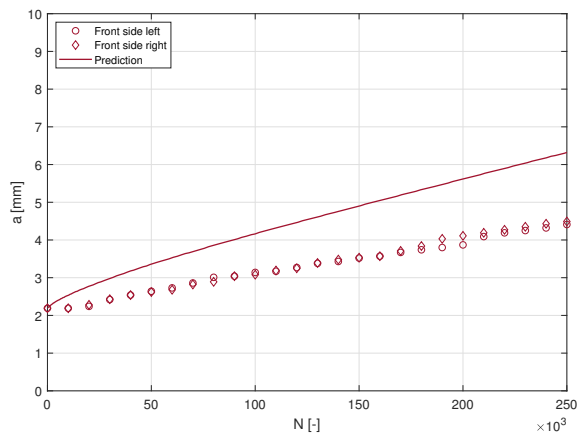


Figure 5.26: Crack growth comparison between test 1 data and prediction

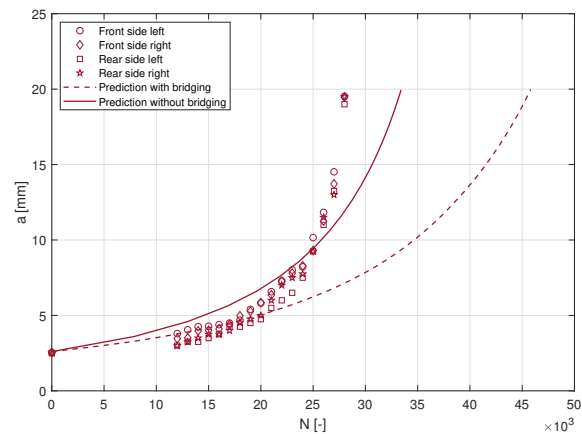


Figure 5.27: Crack growth comparison between test 2 data and prediction

Test 3

The plastic zone due to an overload is larger when, in addition to the mode I fracture, a mode II fracture is present than when only a mode I fracture is present, as demonstrated in Section 3.7.3. The larger plastic zone results in a longer period of crack growth retardation. However, when using the same Wheeler model exponent as Khan [8] ($m = 2$), the crack growth prediction is too conservative. Tweaking this exponent results in a better match between prediction and test data as observed in Figure 5.28.

Figure 5.29 presents the top right part of the delamination, including the initial starter notch in the bottom left corner. Both the modelled delamination size as the one determined by DIC overpredict the actual delamination size (etched) as depicted in Figure 5.29. Despite the much larger modelled delamination, the crack growth is predicted well.

From Figure 5.29 it can be concluded that the location of the delamination boundary cannot be accurately obtained by the DIC method for small delaminations. The delamination is not larger than the plastic zone around the crack (see Figure 4.12) and therefore the method described in Section 4.5.2 becomes inaccurate.

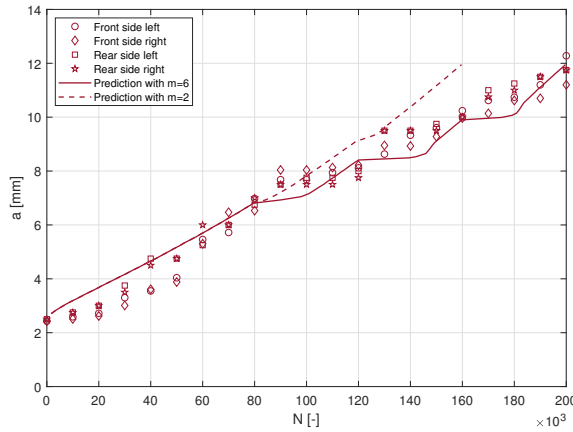


Figure 5.28: Crack growth comparison between test 3 data and prediction

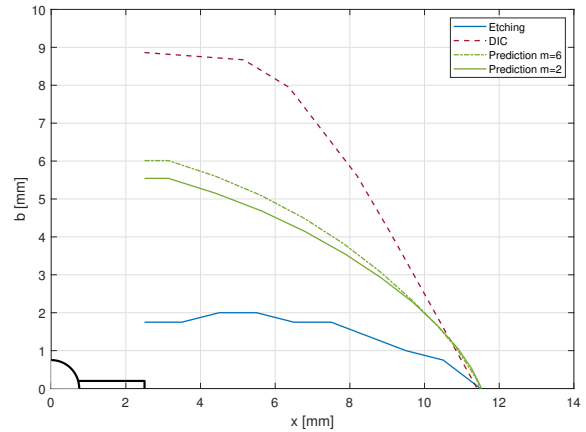


Figure 5.29: Delamination comparison between test 3 data and prediction

Table 5.3 presents the fracture angles measured on test specimen 3. Similar to the prediction shown in Figure 5.5, the fracture angle for GLARE 3 is underestimated.

Table 5.3: Fracture angle comparison between data from test 3 test and prediction

Test ID	Front side		Rear side		Prediction
	Left	Right	Left	Right	
Test 3	7°	8°	8°	7°	4.2°

Test 4 and 5

Test 4 and 5 are performed with the same laminate lay-up, but differ in the applied loading. As explained in Section 4.5.3, the longer crack length at the front side of the specimen in test 4 is caused by the misalignment of the test specimen in the test machine. Since the stress in the metal layer at the rear side is lower compared to when no bending moment is present, it is expected that the prediction, presented in Figure 5.30, would be in between the test data from the front and rear side. The prediction and test data concerning the crack growth of test specimen 5 show a good resemblance as displayed in Figure 5.31.

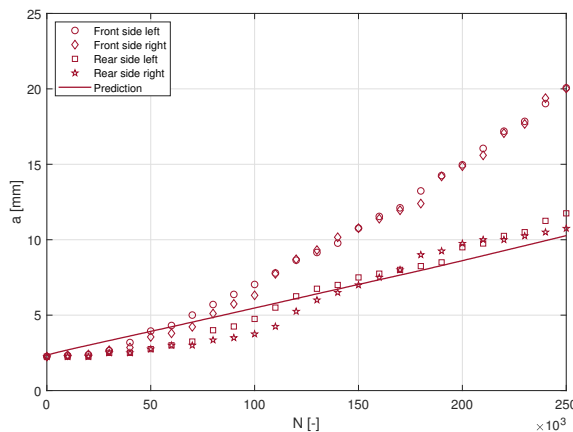


Figure 5.30: Crack growth comparison between test 4 data and prediction

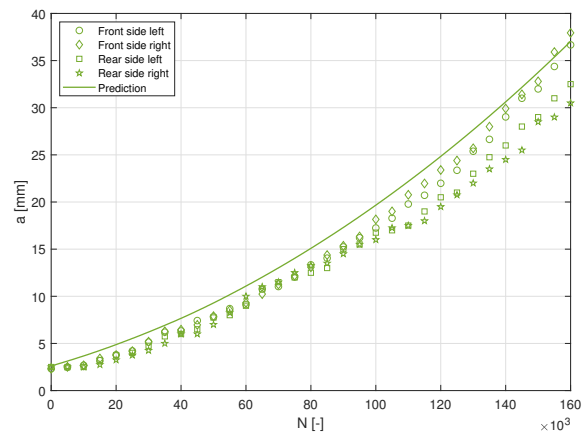


Figure 5.31: Crack growth comparison between test 5 data and prediction

In Figure 5.32 the delamination shape and size between the test data of test specimen 4 and the model's prediction are compared. In the region towards the initial notch, a difference in delamination size is noticed; however, a difference in delamination size in this region is of less influence since the

magnitude of the bridging load located near the crack tip is larger than at the starter notch [5]. The delamination determined by DIC is slightly overpredicted.

Figure 5.33 makes a similar comparison for test 5, where a near perfect fit is noticed between the DIC method and the actual delamination. Again, a small difference in delamination size at the starter notch is present between model and reality, but is of marginal influence as mentioned before.

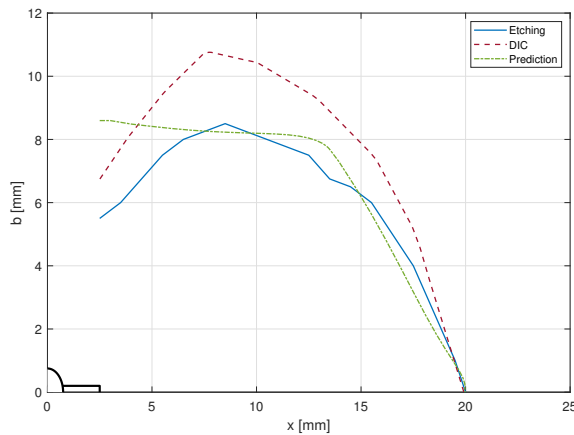


Figure 5.32: Delamination comparison between test 4 data and prediction

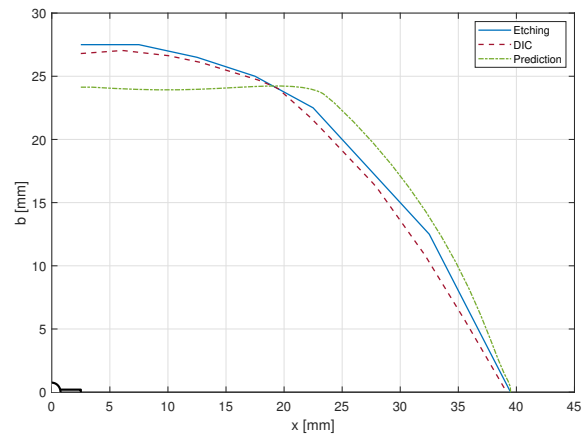


Figure 5.33: Delamination comparison between test 5 data and prediction

Tests by Maretti [50] have shown that testing the same laminate under the same off-axis angle with a higher S_{max} , yields a lower fracture angle. This trend is captured by the model since the fracture angle for the test under $S_{max} = 100$ MPa is predicted to be 8.8° and 6.7° for $S_{max} = 140$ MPa. Table 5.4 presents the fracture angles for both tests measured for each half crack length individually. It can be concluded that the prediction fracture angle lies close to the test data.

Table 5.4: Fracture angle comparison between data from test 4 and 5 test and prediction

Test ID	Front side		Rear side		Prediction
	Left	Right	Left	Right	
Test 4	7°	8°	7°	9°	8.8°
Test 5	6°	5°	6°	7°	6.7°

Note: The predicted angles are the opposite number from what to model predicts (similar to Figure 5.7)

Test 6

Figure 5.34 presents the crack growth of test 6, where a similar crack growth behaviour as in test 4 is observed. It is expected that the crack length at the front and rear side of the specimen have a different value since the neutral axis does not coincide with the mid-plane of the laminate as is the case with all earlier discussed symmetric lay-ups. However, the difference between the two crack length in the test data is large (almost twice as large at 160 kcycles) and the largest crack is located at the rear side, which is opposite from what is expected. These concerns suggest that, similar to test 4, a misalignment between the load axis and the specimen was present during testing; albeit this was not noticed during testing.

The delamination comparison between test and prediction is presented in Figure 5.35. The actual delamination and the delamination determined by DIC nearly coincide, while the model exhibits a divergent shape at the crack length between 2.5 and 28 mm. The shape of this delamination seems to be influenced by the delaminations of the GLARE core as depicted in Figure 5.36.

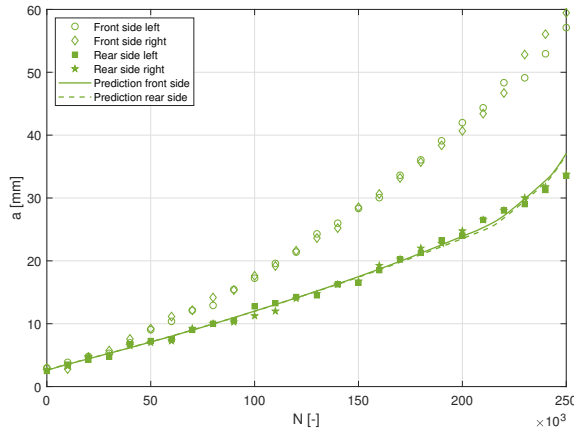


Figure 5.34: Crack growth comparison between test 6 data and prediction

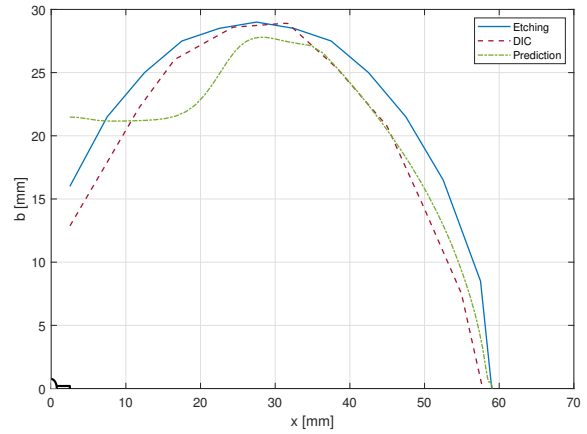


Figure 5.35: Delamination comparison between test 6 data and prediction (front side)

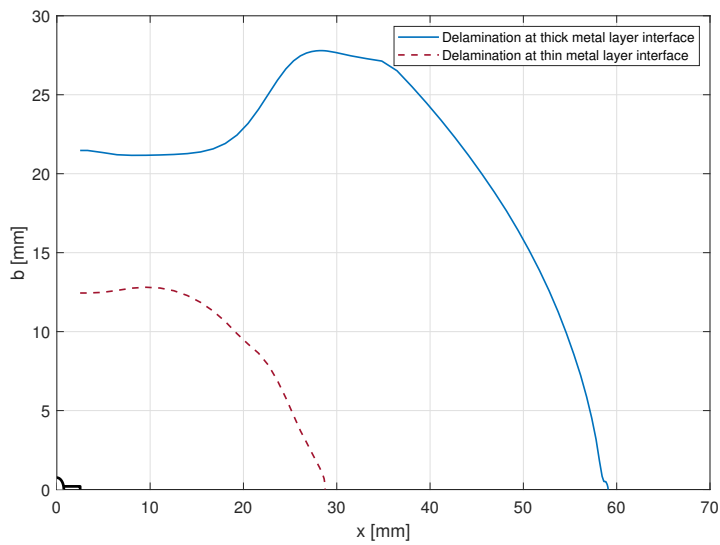


Figure 5.36: Delaminations test specimen 6

The prediction of the fracture angle at the rear side of the specimen, presented in Table 5.5, lies close to the test data. The prediction at the front side fracture angle, however, misses the mark. The conclusion from Maretti [50] that the crack of the surface layer is most influenced by the adjacent fibre layer is not captured by the model.

Table 5.5: Fracture angle comparison between data from test 6 test and prediction

Test ID	Front side		Rear side		Prediction	
	Left	Right	Left	Right	Left	Right
Test 6	0°	1°	2°	3°	3.7°	3.9°

Note: The predicted angles are the opposite number from what to model predicts (similar to Figure 5.7)

6

Discussion

This chapter evaluates the model by, amongst others, answering the research questions in Section 6.1. Furthermore, the model's limit of validity (Section 6.2) is discussed, as well as its capabilities (Section 6.3). In Section 6.4, suggestions are made to further extend the model such that its applicability becomes larger and its functionality better.

6.1. Model Discussion

A detailed answer to the main research question, *How to predict the fatigue crack growth rate and damage directionality for non-conventional FMLs under CA and VA loading?*, is given in Chapter 3. However, a concise answer is given by providing answers to the sub-questions, which for clarification are repeated here:

1. To what extent is the model of Wilson valid for FMLs with multiple fibre types?
2. How to add off-axis loading to the current model?
 - (a) To what extent is it valid to use the SIF in transverse direction, as proposed by Gupta, into the model of Wilson to predict fatigue crack growth under off-axis loading?
 - (b) Under what conditions can a mode III delamination be neglected?
3. How to model a metal-adhesive-metal interface?
4. To what extent is the VA loading module of Khan valid for non-conventional FMLs?

In theory Wilson's model should be applicable to any combination of materials since it is based on mechanical principles and uses only material properties to calculate the damage in the FML. The model validation by test specimen A, C and C2 from Rensma [44] substantiate this statement. These three specimens all contain multiple fibre types (glass and carbon) which are solely oriented in loading direction and therefore, the computation only makes use of Wilson's code. In general, the prediction lies close to the test data (the cause for the difference between test data and prediction is elaborated on in Section 5.2.1). It is therefore stated that, as long as the material properties are known, the model developed by Wilson [17] is also valid for FMLs in which multiple fibre types are present.

The answer to the second research sub-question is threefold: the implementation of the transverse SIF to accommodate the use of off-axis fibres is validated by the numerous examples given in Section 5.2.1. One important parameter in combining the mode I and II SIF is the bridging angle, which ensures that the bridging load is always in line with the fibre orientation. Also, ignoring the mode III delamination proved to be a valid assumption considering the accurate crack growth and fracture angle predictions.

The good correspondence in test data and prediction for test 4, 5 and 6, described in Section 5.2.2, further substantiates the answers on research question 1 and 2 since the lay-ups used in these tests combine the components of the two individual questions, i.e. multiple fibre types and off-axis loading.

In non-conventional FMLs two metal layers can be bonded with an adhesive instead of with a prepreg layer. Tests have shown that no delamination is present and that the crack will propagate in the adhesive layer as well [34]. A short study on how to model this behaviour is given in Appendix C. The proposed method to model a metal laminate is to set the bridging load to zero; thereby also eliminating delamination growth. This solution yields good results as shown in Figure 5.19.

The last research question concerns VA loading of which only one test has been performed with a non-conventional FML. After tweaking the Wheeler model exponent, a good match between test data and prediction is found. Due to the good result, one is inclined to state that the VA module developed by Khan [8] is also valid for non-conventional FMLs. However, since only one test has been performed, it is premature to make such a statement and therefore additional testing and validation is recommended. Furthermore, the value of the Wheeler model exponent (m) must be investigated.

6.2. Limit of Validity

The limit of validity of the model is determined by the validation tests. This section discusses three different aspects concerning the limit of validity: the laminate (Section 6.2.1), the initial damage size (Section 6.2.2) and the applied loading (Section 6.2.3).

6.2.1. Laminate

Certain characteristics relate to non-conventional FMLs, such as the choice in fibre type and orientation, the use of multiple metal types and thicknesses, and the stacking sequence of the different plies, which can result in (un)balanced and (a)symmetric laminates. In order to determine the limit of validity concerning these characteristics, a distinction is made between laminates with a lay-up containing only UD plies (e.g. GLARE 2A) and laminates containing cross-ply.

The majority of tested specimens contains cross-ply. In general, the model predicted the crack growth and fracture angle accurately regardless of the off-axis angle. All aspects characterising a non-conventional FML have been validated extensively, apart from FMLs having an asymmetric lay-up of which only one test is performed.

The predicting capabilities of the model concerning UD FMLs which are placed under an off-axis angle, are validated from off-axis angle 0° till 22.5° . At larger off-axis angles ($22.5^\circ - 45^\circ$) a correction factor can be applied to get a reasonable prediction, but for off-axis angles larger than 45° , the model is not able to predict the crack growth, nor the fracture angle, accurately. However, since such laminates are mostly oriented in the main loading direction in real life applications, this limitation in the predicting capability of the model is irrelevant. Although not validated by test data, it is reasonable that these remarks can be extended to laminates which contain fibres with a small angle orientation such as lay-ups B-T700, B-T800 and D in Figure 5.20.

6.2.2. Initial Damage Size

The initial damage size ($2s$) is regularly chosen to be 5 mm in tests, yet Gonesh [34] performed two tests with a larger initial damage size ($2s = 30$ mm). Results from these test are given in Figure B.1 and B.2.

Figure B.1 presents the comparison between the crack growth data and prediction of a GLARE 3-4/3-0.4 laminate. The FWCF does not seem to influence the crack growth curve, while the test data have an increasing crack growth rate after $\alpha = 45$. However, until a half crack length of 40 mm, the prediction is accurate.

The trend between the prediction for the GLARE 4B specimen and the test data is the same as presented in Figure B.2; however, the prediction has a slightly lower crack growth rate. Despite these small errors, it is concluded that the model is also capable of predicting crack growth for larger initial damage sizes.

6.2.3. Loading

The model has been validated for both CA as VA loading. All test are performed in the tension-tension regime with R varying from 0.05 to 0.1 and the maximum stresses varying from 80 till 200 MPa.

The base model (Wilson's model [17]) is validated from $S_{max} = 80$ to 160 and $R = -0.3$ to 0.5. In addition, the model is validated with legacy test data from Randell [51] for a tension-bending load case with bending ratios (the ratio of the surface stress to the stress at the NA) varying from 2 till 2.77. Although these load types have not been validated for non-conventional FMLs, it is assumed that the current model is able to make accurate crack growth predictions within these load conditions since the damage mechanisms to describe off-axis loading are similar to the damage mechanisms for in-axis loading. Whether the fracture angle predictions are still reliable under these load cases is unknown, since Equation 2.14 is only validated for tension loads.

6.3. Practical Use of Model

This section presents useful information when first using the model. Various topics such as convergence (Section 6.3.1), the influence of computational parameters (Section 6.3.2) and shortcomings in the model (Section 6.3.3) are discussed.

6.3.1. Convergence

Rensma [44] discovered that Alderliesten's [5] model, which has an equal discretisation (Figure 2.4), does not converge. Wilson [17] solves this problem by making use of a Chebyshev distribution. This means that, in general, the rule *the smaller the mesh size, the more accurate the prediction will be* holds.

In practice, the more 'simple' laminates such as GLARE, do not require a very small maximum mesh size (w_{max}). Figure 6.1 presents the crack growth prediction of a GLARE 3-4/3-0.4 specimen with an off-axis angle of 45° and a load of $S_{max} = 100$ MPa and $R = 0.05$ for varying mesh sizes. From Figure 6.1 it can be seen that all predictions lie close to each other. The influence of the mesh size is more clear to observe in the crack growth data, as depicted in Figure 6.2. More noise is present when a large maximum mesh size is chosen. Mesh size of 0.05 and smaller do not show noise and therefore mesh sizes smaller than 0.05 are not shown in Figure 6.2.

A similar convergence is noticed at the fracture angle prediction as can be seen in Figure 6.3. The fracture angle becomes larger when the mesh size is smaller, however, the influence of the mesh size on the fracture angle is marginal.

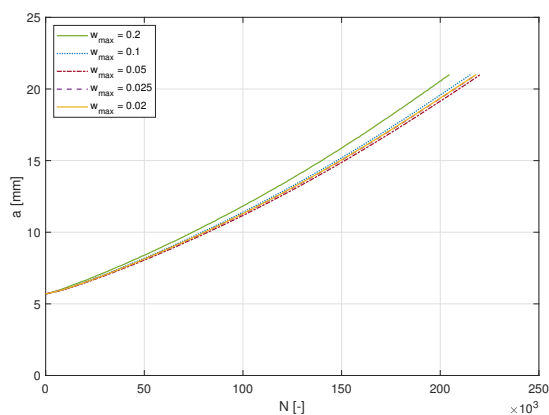


Figure 6.1: Crack growth prediction for GLARE 3-4/3-0.4 under $S_{max} = 100$ MPa and $R = 0.05$ at $OAA = 45^\circ$ for various mesh sizes

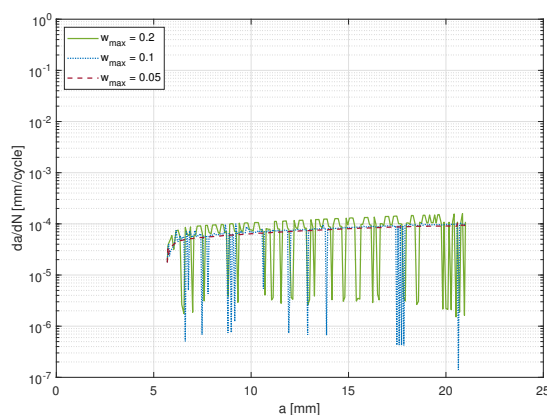


Figure 6.2: Crack growth rate prediction for GLARE 3-4/3-0.4 under $S_{max} = 100$ MPa and $R = 0.05$ at $OAA = 45^\circ$ for various mesh sizes

The mesh size has a major influence on the computational time. In Table 6.1 the computational times for the different mesh sizes are shown. Table 6.1 also lists the absolute and relative error with respect to the solution with the smallest mesh size. Reducing the mesh size reduces the relative error, proving convergence. This table shows that a prediction with an error smaller than 2% is computed in an order of magnitude smaller than the solution with a mesh size of 0.02.

Similar convergence is found for Laminate 1, a laminate which is unbalanced and contains multiple alloy types and fibre types, as presented in Figure 6.4. For Laminate 2, an asymmetric laminate, no convergence is seen as depicted in Figure 6.5.

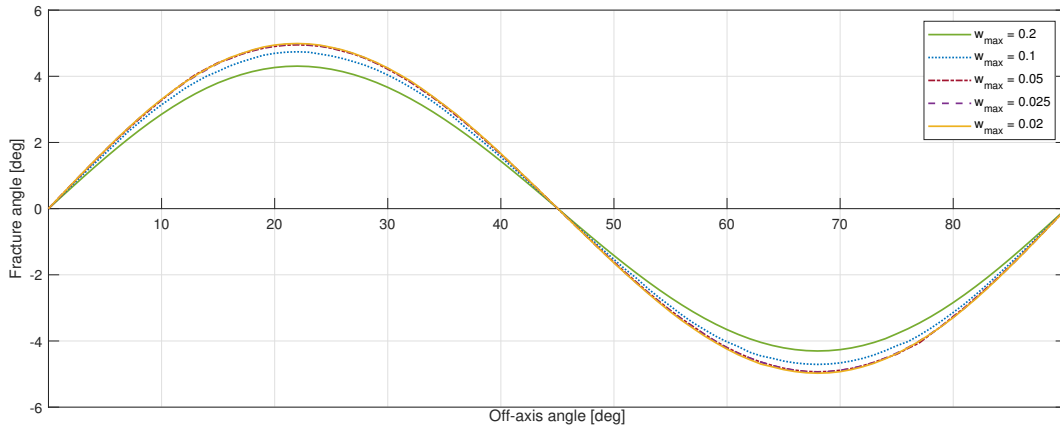


Figure 6.3: Fracture angle prediction for GLARE 3-4/3-0.4 under $S_{max} = 100$ MPa and $R = 0.05$ at $OAA = 45^\circ$ for various mesh sizes

Table 6.1: Mesh size comparison for GLARE 3-4/3-0.4 under $S_{max} = 100$ MPa and $R = 0.05$ at $OAA = 45^\circ$

w_{max}	Computational time [s]	Absolute error [# cycles]	Relative error [%]
0.200	16	13473	6.18
0.100	54	2899	1.33
0.050	173	-1955	-0.90
0.025	909	-205	-0.09
0.020	1560	0	0.00

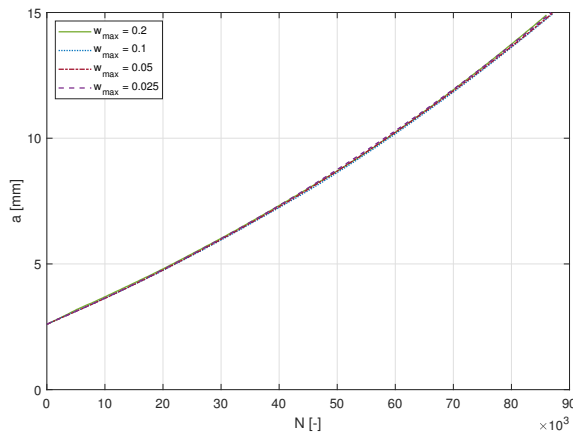


Figure 6.4: Crack growth prediction for Laminate 1 under $S_{max} = 140$ MPa and $R = 0.05$ at $OAA = 0^\circ$ for various mesh sizes

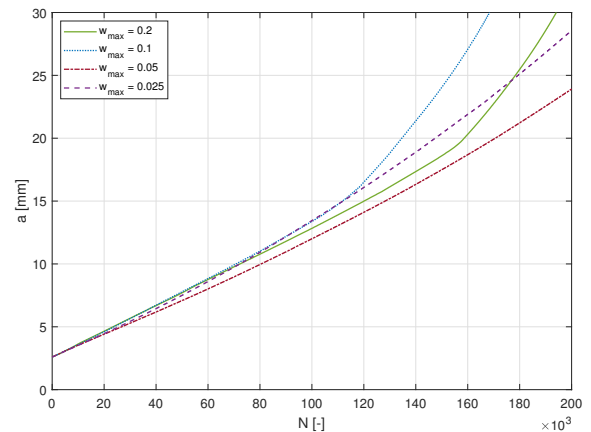


Figure 6.5: Crack growth prediction for Laminate 2 under $S_{max} = 140$ MPa and $R = 0.05$ at $OAA = 0^\circ$ for various mesh sizes

6.3.2. Computational Parameters

The parameters listed in Table 3.1 are not the complete set of inputs. Additional parameters are built in by Spronk [13] to define certain settings. The parameters relevant for the practical use of the model are discussed in this section; for others reference is made to the code manual [52].

N_x -factor and M_x -factor

The input loading can be factorised by the N_x -factor and M_x -factor. The inputs in Spronk's [13] model follow the reference system as defined in the CLT, i.e. the x -direction is the main loading direction. The following load and moment are applied to the model

$$\begin{bmatrix} N_x \\ N_y \\ N_{xy} \\ M_x \\ M_y \\ M_{xy} \end{bmatrix} = F \cdot \begin{bmatrix} N_x\text{-factor} \\ 0 \\ 0 \\ M_x\text{-factor} \\ 0 \\ 0 \end{bmatrix} \quad (6.1)$$

in which F is the load given by the spectrum input.

APW

The number of updates per w_{max} is labelled APW. The bar element width can have a maximum width defined by w_{max} , however, w_{max} is also used for defining the crack increase Δa . The crack increase is tuned by APW in order to decrease Δa and therefore increasing the number of computations and accuracy.

CPF

Cycles Per Flight (CPF) is a parameter to be set when VA loading is applied. By default, the model assumes the input spectrum to represent one flight. When a similar analysis is desired as when CA loading is applied, CPF is set to 1 such that the model predicts after how many flights (and in this case cycles) the maximum crack length has been reached.

6.3.3. Shortcomings

The manner in which the delamination parameters, C_d and n_d , are used, constitutes an interesting shortcoming of the model, which will be discussed here. These parameters are assigned to prepreg or adhesive layers, while in reality the parameters describe the delamination behaviour at the interface between two materials. The following example illustrates the inconsistencies this can create: in case an adhesive is in contact with a prepreg layer, it has a certain value for C_d and n_d (which is also dependent on the adhesive's thickness [17]). However, when using the same adhesive in contact with a metal layer, no delamination is present when the metal layer cracks and thus the values for C_d and n_d are incorrect.

This behaviour urges the model to select C_d and n_d values depending on the interface, requiring a different pre-processing module. A database of C_d and n_d from which the correct values are taken depending on the interfaces instead of giving them as a material property.

6.4. Extensibility

The code is built in a modular manner such that extensions can be made and coupled to the existing code. This section suggests several additions to the model which are deemed useful.

6.4.1. Fatigue Crack Initiation

The additions made to the model are written in the complete tool created by Spronk [13], meaning that the FCI module can be coupled to the FCP module to give an estimate regarding the entire life of a structure. Homan [28] tested off-axis GLARE specimens and concluded that his FCI model is able to predict the initiation life of such specimens and therefore no modification for off-axis loaded specimens is needed.

In GLARE the stress in each metal layer is equal, resulting in a similar FCI life. However, in non-conventional FMLs the metal layers can be of a different type and thickness. These two parameters influence the FCI life of a metal layer, resulting in different FCI instances. The FCP model is able to handle different crack lengths; however, no verification or validation, other than those by Spronk [13], are carried out concerning the coupling of these two modules.

6.4.2. Residual Strength

In order to make a complete analysis of a structure, a residual strength module can be added. Wilson [17] suggests the residual strength model developed by Rodi [29]. However, the model developed by Rodi uses the model of Alderliesten [11] as a basis and thereby limits its applicability to GLARE.

Wilson [17] indicates that fibre breakage and crack tip plasticity are damage modes which are more difficult to model in FMLs wherein the crack length and crack growth rate in the metal layers differ from each other. In addition, the off-axis fibres cause a shear stress which in the case of a quasi-static load creates a large amount of plastic deformation. Alderliesten [9] points out that in order to model quasi-static off-axis loading, an extension of the linear elastic methodology is required.

Although net section approaches such as those of Müller [53] and De Rijck [54] do not model the fracture mechanics, Van der Linden [55] concluded that these approaches give a reasonable residual strength estimate. The residual strength in net section approaches is determined by subtracting the strength provided by the portion of cracked aluminium layers from the laminate strength. The advantage of De Rijck's method is that use is made of the blunt notch strength of the different constituents rather than an experimentally determined blunt notch strength per laminate configuration as is done by Müller.

6.4.3. Crack Configurations

The current model is suitable for Centre Cracked Tension (CCT) specimens, which is related to real life applications by the example of cracks originating from a fastener hole. However, in order to make the model as widely applicable as possible, other crack configurations should be implemented. These other crack configurations require different stress functions (equivalent equations for Equation 3.10, 3.11, 3.33 and 3.34), from which the bridging load can be determined after compatibility is enforced.

In CCT specimens, the delamination sizes at both sides of the crack are approximately the same. However, Thibault-Liboiron [56] observed that the delamination is not evenly distributed around the crack in Double-Edge-Notched Tension (DENT) specimens. Therefore, a re-evaluation of the delamination growth for other configuration types is recommended. Thibault-Liboiron [56] also discovered that Equation 2.14 to compute the fracture angle is not valid for DENT specimens since the fibres above the notch are unloaded and thus influence the crack path. Not only the fracture angles differ, the trajectory itself is different. Whereas the cracks in CCT specimens have a straight trajectory after the initial deflection, the cracks in DENT specimens curve in a continuous manner.

6.4.4. Fracture Angle

Test specimen 6 showed different fracture angles at front and rear side. At the front side, which is attached to the 0° fibre layer, no fracture angle was measured, while at the rear side, which is attached to the 15° fibre layer, small fracture angles are measured. This suggests that the adjacent fibre layer influences the crack path, an aspect that has not been incorporated in the model. A similar conclusion is drawn by Maretti [50] for surface cracks. In non-conventional laminates, the difference in crack length between the metal layers can create 'surface cracks' when the crack length difference is large, confirming the conclusion from Maretti [50].

6.4.5. Applied Shear Stress

The model is able to incorporate the crack growth contribution due to the shear stress unbalanced laminates create. This means that, after adapting the input format and the pre-processing module, a shear stress can be provided as input.

6.4.6. Smearred Properties

Calculating the bridging terms of the individual fibre layers is computationally expensive. In order to decrease the computational time, it is proposed to treat adjacent fibre layers as one material. Lay-up E and E2 in Figure 5.20 are good examples where replacing the 16 plies by one 'dummy' layer will decrease the computational time significantly. During pre-processing, the properties of the 'dummy' are calculated with the CLT. Verification with respect to the original code is recommended.

Conclusions and Recommendations

7.1. Conclusions

The model presented in this thesis is able to predict fatigue crack growth and damage directionality in non-conventional FMLs, solely based on mechanical principles and without the need for fitting parameters. The required inputs consist of a load spectrum, lay-up definition, material properties (including experimentally determined crack growth and delamination parameters), initial damage information and various computational parameters which influence the accuracy and the computational time.

The prediction of fatigue crack growth in FMLs in previous research is based on the superposition of the Stress Intensity Factors (SIFs), meaning that the SIF at the crack tip is the summation of the SIF in the metal layer (crack opening) and the reduction of the SIF due to fibre bridging (crack closing). Since previous research focused on FMLs with fibres oriented in 0° and 90° with respect to the loading direction, only a mode I fracture was investigated.

In non-conventional FMLs, an induced shear stress can arise when an unbalanced laminate with clamped constraints is subjected to a tension stress. This shear stress creates a mode II fracture in the metal layers of the FML. The fibres, which can be oriented under angles other than 0° and 90° with respect to the loading direction, do not only bridge in longitudinal direction, but also in transverse direction. A similar derivation to determine the bridging stress for the mode I fracture is made for a mode II fracture. The mode I and mode II SIF enables the computation of the fracture angle, while combining the two SIFs facilitates the computation of the crack growth rate.

The delamination between the metal and fibre layer, which accommodates the bridging stress, often has a mode III component in non-conventional FMLs in addition to the mode II delamination. It is assumed that the mode III component is negligible due to the small fracture angles, thereby simplifying the delamination growth computation.

The model has been verified and validated with a wide range of test data, acquired from performed tests as well as from literature. The validation has shown that the model is able to predict the fracture angle and the fatigue crack growth rate accurately in most cases. In addition, convergence is demonstrated when computing the damage parameters with smaller step sizes defined by the computational parameters.

Inaccuracies in the crack growth rate and in the fracture angle arise with FMLs containing plies that are all oriented in the same direction and loaded at a large off-axis angle. However, designing such an FML with fibres not oriented in the main loading direction is not desirable; therefore the model is regarded to be valid for relevant cases.

7.2. Recommendations

Certain matters need further attention to increase the model's limit of validity. Firstly, more tests should be performed with asymmetric specimens and with specimens subjected to VA loading. Only one test is insufficient to validate the model for that type of laminate and loading, respectively. In addition to

more tests, the convergence behaviour of asymmetric laminates need to be further reviewed. Lastly, it is recommended to investigate why the negative fracture angle from the model output has to be taken for UD FMLs and not for FMLs containing cross-plyes.

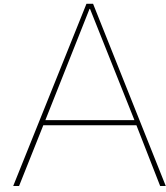
In Section 6.4 multiple suggestions are made to extend the model in order to enlarge the model's applicability and to improve its functionality. The first suggestion concerns the validation of the coupling between the FCI module from Spronk [13] and FCG module discussed in this thesis. Moreover, a module able to calculate the residual strength after a certain amount of cycles is advised in order to be able to make a full analysis (FCI, FCG and RS). Although not being based on fracture mechanics as the other parts of the model, the net section method developed by De Rijck [54] is proposed. Furthermore, crack configurations other than Centre Cracked Tension (CCT) specimens, such as a Double-Edge-Notched Tension (DENT) specimen, can be implemented by adapting the stress functions to make the model more versatile. In addition, a study on the influence of the orientation of adjacent fibre layers on the fracture angle as suggested by Maretti [50] is recommended. Another aspect to improve functionality is to provide a shear stress as input. The model is already able to account for an induced shear stress, leaving only the pre-processing module to be adapted and verified. Finally, the computational time can be reduced by replacing adjacent fibre layers by one 'dummy' material layer. Verification is required to check whether this is a valid approach.

Bibliography

- [1] R.F.H. van Maris. Prediction of Fatigue Crack Growth and Damage Directionality in Non-Conventional Fibre Metal Laminates, 2018. Literature Study.
- [2] R.C. Alderliesten. Personal communication on November 29, 2018.
- [3] R.C. Alderliesten and R. Benedictus. Aircraft wing and fiber metal laminate forming part of such an aircraft wing, 2014. Patent EP2627505B1.
- [4] A. Vlot and J.W. Gunnink. *Fibre Metal Laminates an introduction*. Kluwer Academic Publishers, 2001.
- [5] R.C. Alderliesten. *Fatigue crack propagation and delamination in GLARE*. PhD thesis, TU Delft, 2005.
- [6] J. Schijve, H.T.M. van Lipzig, F.G.J.A. van Gestel, and A.H.W. Hoeymakers. Fatigue properties of adhesive-bonded laminated sheet material of aluminium alloys. *Engineering Fracture Mechanics*, 12:561–579, 1979.
- [7] J.F. Laliberté, C. Poon, P.V. Straznicky, and A. Fahr. Applications of Fiber-Metal Laminates. *Polymer Composites*, 21:558–567, 2000.
- [8] S. Khan. *Fatigue Crack & Delamination Growth in Fibre Metal Laminates under Variable Amplitude Loading*. PhD thesis, TU Delft, 2013.
- [9] R.C. Alderliesten. *Fatigue and Fracture of Fibre Metal Laminates*. Springer, 2017.
- [10] G.S. Wilson, R.C. Alderliesten, and R. Benedictus. A generalized solution to the crack bridging problem of fiber metal laminates. *Engineering Fracture Mechanics*, 105:65–85, 2013.
- [11] R.C. Alderliesten. Analytical prediction model for fatigue crack propagation and delamination growth in GLARE. *International Journal of Fatigue*, 29:628–646, 2007.
- [12] R. Marissen. *Fatigue crack growth in ARALL. A hybrid aluminium-aramid composite material: Crack growth mechanisms and quantitative predictions of the crack growth rates*. PhD thesis, TU Delft, 1988.
- [13] S.W.F. Spronk. Predicting fatigue crack initiation and propagation in Glare reinforced frames. Master's thesis, TU Delft, 2013.
- [14] V.V. Silberschmidt. *Dynamic Deformation, Damage and Fracture in Composite Materials and Structures*. Woodhead Publishing, 2016.
- [15] R.C. Alderliesten. On the available relevant approaches for fatigue crack propagation prediction in Glare. *International Journal of Fatigue*, 29(2):289–304, 2007.
- [16] G.H.J.J. Roebroeks, P.A. Hooijmeijer, E.J. Kroon, and M.B. Heinimann. The Development of Central. In *First International Conference on Damage Tolerance of Aircraft Structures*, 2007. Sept 25 – 28, 2007 Delft, The Netherland.
- [17] G.S. Wilson. *Fatigue Crack Growth Prediction for generalized fiber metal laminates and hybrid materials*. PhD thesis, TU Delft, 2013.
- [18] Y.-J. Guo and X.-R. Wu. A theoretical model for predicting fatigue crack growth rates in fibre-reinforced metal laminates. *Fatigue & Fracture of Engineering Materials & Structures*, 21:1133–1145, 1998.

- [19] Y.-J. Guo and X.-R. Wu. Bridging stress distribution in center-cracked fiber reinforced metal laminates: modeling and experiment. *Engineering Fracture Mechanics*, 63:147–163, 1999.
- [20] H. Tada, P.C. Paris, and G.R. Irwin. *The stress analysis of cracks handbook*. ASME Press, 2000.
- [21] H.L. Ewalds and R.J.H. Wanhill. *Fracture Mechanics*. Delft University Press, 1989.
- [22] C.D. Rans, R.C. Alderliesten, and R. Benedictus. Misinterpreting the results: How similitude can improve our understanding of fatigue delamination growth. *Composites Science and Technology*, 71:230–238, 2011.
- [23] R.C. Alderliesten. Application of the energy release rate approach for delamination growth in Glare. *Engineering Fracture Mechanics*, 73:697–709, 2006.
- [24] G.S. Wilsen, R.C. Alderliesten, R. Rodi, and H.J.K. Lemmen. Practical Applications of Improvements in FML Crack Bridging Theory. *25th ICAF Symposium, Rotterdam*, pages 539–558, 2009.
- [25] H.M. Plokker, S.U. Khan, R.C. Alderliesten, and R. Benedictus. Fatigue crack growth in fibre metal laminates under selective variable-amplitude loading. *Fatigue and Fracture of Engineering Materials and Structures*, 32:233–248, 2009.
- [26] O. Wheeler. Spectrum loading and crack growth. Technical report, 1970. ASMR 72 MetX also G.D. Report FZM 5602.
- [27] A.U. De Koning and H.H. van der Linder. Prediction of fatigue crack growth rates under variable amplitude loading. Technical report, NLR, 1981. NLR MP 81023U.
- [28] J.J. Homan. Fatigue initiation in fibre metal laminates. *International Journal of Fatigue*, 28:366–374, 2006.
- [29] R. Rodi. *The Residual Strength Failure Sequence in Fibre Metal Laminates*. PhD thesis, TU Delft, 2012.
- [30] M. Gupta, R.C. Alderliesten, and R. Benedictus. Crack paths in fibre metal laminates: Role of fibre bridging. *Engineering Fracture Mechanics*, 108:183–194, 2013.
- [31] M. Gupta. *Directionality of damage growth in fibre metal laminates and hybrid structures*. PhD thesis, TU Delft, 2017.
- [32] F. Erdogan and G.C. Sih. On the crack extension in plates under plane loading and transverse shear. *Journal of Basic Engineering*, pages 519–527, 1963.
- [33] J. Schijve. *Fatigue of Structures and Materials*. Springer, 2009.
- [34] K. Gonesh. Additional test results and evaluation of crack propagation in off-axis GLARE. Technical report, Delft University of Technology, 2002. B2V-02-02.
- [35] A.S.J. Suiker and N.A. Fleck. Crack tunneling and plane-strain delamination in layered solids. *International Journal of Fatigue*, 125:1–32, 2004.
- [36] C. Kassapoglou. *Design and Analysis of Composite Structures with applications to aerospace structures*. Wiley, 2010.
- [37] N.J. Pagano and J.C. Halpin. Influence of End Constraint in the Testing of Anisotropic Bodies. *Journal of Composite Materials*, 2:18–31, 1968.
- [38] M.-J. Pindera and C.T. Herakovich. Shear Characterization of Unidirectional Composites with the Off-axis Tension Test. *Experimental Mechanics*, pages 103–112, 1986.
- [39] C.T. Sun and T.N. Farris. On the completeness of the Westergaard stress functions. *International Journal of Fracture*, 40:73–77, 1989.
- [40] K. Gonesh. Test results and evaluation of crack propagation in off-axis GLARE. Technical report, Delft University of Technology, 2001. Report B2V-01-24.

- [41] J. Schijve, G. Campoli, and A. Monaco. Fatigue of structures and secondary bending in structural elements. *International Journal of Fatigue*, 31:1111–1123, 2009.
- [42] Y. Zhao, R.C. Alderliesten, Z. Wu, Z. Zhou, G. Fang, J. Zhang, and R. Benedictus. Finite-width-correction factor in fatigue crack growth prediction of GLARE by equivalent compliance method. Not published yet.
- [43] J. Schijve. Some formulas for the crack opening stress level. *Engineering Fracture Mechanics*, 14:461–465, 1981.
- [44] E. Rensma. Investigation of Innovative Concepts for Hybrid Structures. Master's thesis, TU Delft, 2007.
- [45] T.L. Anderson. *Fracture Mechanics: Fundamentals and Applications*. Taylor & Francis Group, 2005.
- [46] N. Perez. *Fracture Mechanics*. Kluwer Academic Publishers, 2004.
- [47] Delta Tech. Dt120 versatile high toughness epoxy matrix - technical data sheet. Issue 10: February 2015.
- [48] R. Rodi, R. Alderliesten, and R. Benedictus. An experimental approach to investigate detailed failure mechanisms in fibre metal laminates. In M. Bos, editor, *ICAF 2009, Bridging the Gap between Theory and Operational Practise*, pages 493 – 512. Springer Science, 2009. 25th ICAF Symposium - Rotterdam, 27 - 29 May 2009.
- [49] L.B. Vogelesang. *Handleiding voor het diepetsen*. Technische Hogeschool Delft, 1968.
- [50] V. Maretti. Surface crack path in FML: off-axis propagation under fatigue loading. Master's thesis, Politecnico di Milano, 2015.
- [51] C.E. Randell. *Subsurface Fatigue Crack Growth in Glare Fibre Metal Laminates*. PhD thesis, TU Delft, 2005.
- [52] S.W.F. Spronk. *FML Fatigue Code Documentation*. Faculty of Aerospace Engineering, TU Delft, June 2013.
- [53] R.P.G. Müller. *An Experimental and Analytical Investigation on the Fatigue Behaviour of Fuselage Riveted Lap Joints*. PhD thesis, TU Delft, 1995.
- [54] J.J.M. de Rijck. *Stress Analysis of Fatigue Crack in Mechanically Fastened Joints*. PhD thesis, TU Delft, 2005.
- [55] A. van der Linden. Residual strength of a FML reinforced frame member. Master's thesis, TU Delft, 2015.
- [56] K. Thibault-Liboiron. Off-Axis Edge-Crack Propagation and Delamination in Fibre Metal Laminate GLARE. Technical report, TU Delft and Université du Québec, 2010.



Test Reports

This appendix includes the test reports in a chronological order. As mentioned in Chapter 4, every 2500 cycles¹ a picture is taken to measure the crack length. However, due to the long process time, not every data point is used. This does not influence the results since the general trend is still captured. As a benefit, less noise is present in the crack growth rate data. All test data is stored at <https://data.4tu.nl/repository/uuid:1445988c-f0da-4c5f-bdfd-11467168b251>.

Test ID	2	Start date & time	20/05/2019 - 12:04
Laminate	GLARE 2A-4/3-0.4	Machine	MTS 250 kN DASML TU Delft
Off-axis angle [deg]	80	Test frequency [Hz]	10
Length [mm]	365.00	S_{max} [MPa]	100.00
Width [mm]	139.34	P_{max} [kN]	34.00
Thickness [mm]	2.44	S_{min} [MPa]	5.00
Saw-cut length [mm]	5.00	P_{min} [kN]	1.70

N	Crack length [mm]				N	Crack length [mm]			
	Front left	Front right	Rear left	Rear right		Front left	Front right	Rear left	Rear right
0	2.54	2.54	2.50	2.50	21000	6.57	6.36	5.50	6.00
12000	3.80	3.46	3.00	3.00	22000	7.29	7.26	6.00	7.00
13000	4.05	3.51	3.25	3.25	23000	8.01	7.80	6.50	7.50
14000	4.25	3.97	3.25	3.50	24000	8.22	8.29	7.50	7.75
15000	4.28	4.01	3.50	3.75	25000	10.16	9.30	9.25	9.25
16000	4.39	4.11	3.75	3.75	26000	11.83	11.26	11.00	11.50
17000	4.49	4.38	4.25	4.00	27000	14.52	13.72	13.25	13.00
18000	4.68	4.97	4.25	4.50	28000	19.52	19.48	19.00	19.50
19000	5.40	5.27	4.50	4.75	28781	Failure			
20000	5.82	5.84	4.75	5.00					

¹For test 2 every 1000 cycles a picture is taken due to the small amount of cycles until failure. For test 3 every 1000 cycles a picture is taken after an overload is applied. 5000 cycles after the overload, the measurement interval is set again to 2500 cycles.

Test ID	4	Start date & time	20/05/2019 - 15:08
Laminate	Laminate 1	Machine	MTS 250 kN DASML TU Delft
Off-axis angle [deg]	0	Test frequency [Hz]	10
Length [mm]	365.00	S_{max} [MPa]	100.00
Width [mm]	139.97	P_{max} [kN]	69.85
Thickness [mm]	4.99	S_{min} [MPa]	5.00
Saw-cut length [mm]	5.00	P_{min} [kN]	3.49

N	Crack length [mm]			
	Front left	Front right	Rear left	Rear right
0	2.26	2.26	2.25	2.25
10000	2.33	2.35	2.25	2.25
20000	2.38	2.40	2.25	2.25
30000	2.65	2.68	2.50	2.50
40000	3.19	2.86	2.50	2.50
50000	3.95	3.56	2.75	2.75
60000	4.32	3.80	3.00	3.00
70000	5.01	4.23	3.25	3.00
80000	5.71	5.11	4.00	3.35
90000	6.38	5.75	4.25	3.50
100000	7.04	6.32	4.75	3.75
110000	7.80	7.74	5.50	4.25
120000	8.65	8.71	6.25	5.25
130000	9.16	9.32	6.75	6.00
140000	9.78	10.17	7.00	6.50
150000	10.77	10.77	7.50	7.00
160000	11.55	11.40	7.75	7.50
170000	12.12	11.96	8.00	8.00
180000	13.24	12.40	8.25	9.00
190000	14.26	14.20	8.50	9.25
200000	14.97	14.88	9.50	9.75
210000	16.06	15.60	9.75	10.00
220000	17.20	17.07	10.25	10.00
230000	17.85	17.68	10.50	10.25
240000	19.03	19.39	11.25	10.50
250000	20.07	20.03	11.75	10.75

Note: The specimen was not aligned with the machine's load cell.

Test ID	5	Start date & time	21/05/2019 - 8:49
Laminate	Laminate 1	Machine	MTS 250 kN DASML TU Delft
Off-axis angle [deg]	0	Test frequency [Hz]	10
Length [mm]	365.00	S_{max} [MPa]	140.00
Width [mm]	139.80	P_{max} [kN]	96.88
Thickness [mm]	4.95	S_{min} [MPa]	7.00
Saw-cut length [mm]	5.00	P_{min} [kN]	4.84

N	Crack length [mm]			
	Front left	Front right	Rear left	Rear right
0	2.32	2.32	2.50	2.50
5000	2.48	2.52	2.50	2.50
10000	2.69	2.68	2.50	2.50
15000	3.17	3.41	3.25	2.75
20000	3.80	3.77	3.75	3.25
25000	4.21	4.19	4.00	3.75
30000	5.15	5.19	4.75	4.25
35000	6.20	6.29	5.75	5.00
40000	6.33	6.46	6.00	6.00
45000	7.43	6.97	6.50	6.00
50000	7.82	7.90	7.75	7.00
55000	8.70	8.52	8.00	8.25
60000	9.13	9.32	9.00	10.00
65000	10.78	10.24	10.75	11.00
70000	11.04	11.26	11.50	11.50
75000	12.05	12.20	12.00	12.50
80000	13.34	13.09	12.50	13.25
85000	14.05	14.38	13.00	13.50
90000	15.24	15.36	15.00	14.50
95000	16.21	16.35	15.50	15.50
100000	17.25	18.16	16.75	16.00
105000	18.29	19.01	17.00	17.25
110000	19.79	20.77	17.50	17.50
115000	20.72	21.97	19.00	18.00
120000	21.99	23.40	20.50	19.50
125000	23.37	24.40	21.00	20.75
130000	25.39	25.70	23.00	22.00
135000	26.65	28.00	24.75	23.50
140000	29.03	29.92	26.00	24.50
145000	31.01	31.42	28.00	25.50
150000	32.00	32.80	29.00	28.50
155000	34.38	35.91	31.00	29.00
160000	36.67	37.94	32.50	30.50

Test ID	6	Start date & time	21/05/2019 - 16:24
Laminate	Laminate 2	Machine	MTS 250 kN DASML TU Delft
Off-axis angle [deg]	0	Test frequency [Hz]	10
Length [mm]	360.00	S_{max} [MPa]	140.00
Width [mm]	139.04	P_{max} [kN]	121.08
Thickness [mm]	6.22	S_{min} [MPa]	7.00
Saw-cut length [mm]	5.00	P_{min} [kN]	6.05

N	Crack length [mm]			
	Front left	Front right	Rear left	Rear right
0	2.97	2.97	2.50	2.50
10000	3.85	2.79	3.50	3.25
20000	4.79	4.68	4.25	4.75
30000	5.29	5.73	4.75	5.00
40000	6.95	7.58	6.75	6.50
50000	9.05	9.22	7.25	7.00
60000	10.38	11.14	7.50	7.25
70000	12.13	12.14	9.00	9.25
80000	12.91	14.17	10.00	10.00
90000	15.45	15.34	10.50	10.25
100000	17.24	17.62	12.75	11.25
110000	19.59	19.18	13.25	12.00
120000	21.40	21.60	14.25	14.00
130000	24.29	23.62	14.50	14.75
140000	25.99	25.21	16.25	16.25
150000	28.33	28.53	16.50	16.75
160000	30.05	30.63	18.50	19.25
170000	33.62	33.18	20.25	20.25
180000	36.07	35.71	21.25	22.00
190000	39.10	38.37	23.25	22.75
200000	41.99	40.67	24.00	24.75
210000	44.35	43.41	26.50	26.50
220000	48.34	46.70	28.00	28.00
230000	49.12	52.81	29.00	30.00
240000	52.95	56.06	31.25	31.75
250000	57.11	59.45	33.50	33.75

Note: Test results suggest the specimen was not aligned with the machine's load cell; however, not noticed during testing.

Test ID	3	Start date & time	22/05/2019 - 10:37
Laminate	GLARE 3-4/3-0.5	Machine	MTS 250 kN DASML TU Delft
Off-axis angle [deg]	22.5	Test frequency [Hz]	10
Length [mm]	350.00	$S_{max,base}$ [MPa]	140.00
Width [mm]	140.30	$P_{max,base}$ [kN]	39.28
Thickness [mm]	2.80	$S_{min,base}$ [MPa]	7.00
Saw-cut length [mm]	5.00	$P_{min,base}$ [kN]	1.96
		$S_{max,OL}$ [MPa]	160.00
		$P_{max,OL}$ [kN]	62.85

N	Crack length [mm]			
	Front left	Front right	Rear left	Rear right
0	2.50	2.50	2.43	2.43
10000	2.75	2.75	2.59	2.51
20000	3.00	3.00	2.72	2.62
30000	3.75	3.50	3.30	3.01
40000	4.75	4.50	3.55	3.61
50000	4.75	4.75	4.04	3.88
60000	5.25	6.00	5.46	5.30
70000	6.00	6.00	5.72	6.47
80000	6.75	7.00	6.98	6.53
90000	7.50	7.50	7.68	8.04
100000	7.75	7.50	7.68	8.04
110000	7.75	7.50	7.94	8.13
120000	8.00	7.75	8.12	8.22
130000	9.50	9.50	8.63	8.95
140000	9.50	9.50	9.33	8.93
150000	9.75	9.50	9.61	9.28
160000	10.00	10.00	10.24	9.97
170000	11.00	10.75	10.62	10.14
180000	11.25	11.00	10.74	10.62
190000	11.50	11.50	11.20	10.70
200000	11.75	11.75	12.28	11.20

Test ID	1	Start date & time	23/05/2019 - 14:21
Laminate	GLARE 2A-4/3-0.3	Machine	MTS 250 kN DASML TU Delft
Off-axis angle [deg]	10	Test frequency [Hz]	10
Length [mm]	350.00	S_{max} [MPa]	100.00
Width [mm]	140.17	P_{max} [kN]	27.61
Thickness [mm]	1.97	S_{min} [MPa]	5.00
Saw-cut length [mm]	5.00	P_{min} [kN]	1.38

N	Crack length [mm]			
	Front left	Front right	Rear left	Rear right
0	2.19	2.19	-	-
10000	2.19	2.19	-	-
20000	2.24	2.28	-	-
30000	2.42	2.43	-	-
40000	2.54	2.54	-	-
50000	2.64	2.62	-	-
60000	2.73	2.68	-	-
70000	2.86	2.82	-	-
80000	3.01	2.89	-	-
90000	3.04	3.04	-	-
100000	3.14	3.08	-	-
110000	3.17	3.19	-	-
120000	3.27	3.25	-	-
130000	3.38	3.39	-	-
140000	3.43	3.48	-	-
150000	3.52	3.53	-	-
160000	3.57	3.57	-	-
170000	3.67	3.71	-	-
180000	3.74	3.84	-	-
190000	3.8	4.03	-	-
200000	3.87	4.11	-	-
210000	4.09	4.19	-	-
220000	4.19	4.27	-	-
230000	4.25	4.35	-	-
240000	4.32	4.43	-	-
250000	4.41	4.49	-	-

B

Additional Validation on Gonesh Data

B.1. Gonesh Data References

Table B.1: Gonesh data reference

Label Gonesh	Lay-up	OAA [deg]	S _{max} [MPa]	2s [mm]	Figure number
OA4 (2001) [40]	GLARE 3-4/3-0.4	45.0	100.0	5.0	5.9 & 5.10
OA3 [40]	GLARE 3-4/3-0.4	45.0	120.0	5.0	5.9 & 5.10
OA14 [34]	GLARE 3-4/3-0.4	45.0	140.0	5.0	5.9 & 5.10
OA4 (2002) [34]	GLARE 3-4/3-0.4	45.0	100.0	30.0	B.1
OA2 [40]	GLARE 3-4/3-0.4	22.5	100.0	5.0	B.3
OA12 [34]	GLARE 3-4/3-0.4	35.0	140.0	5.0	B.4
OA8 (2001) [40]	GLARE 4B-4/3-0.4	45.0	100.0	5.0	5.11 & 5.12
OA11 (2001) [40]	GLARE 4B-4/3-0.4	45.0	120.0	5.0	5.11 & 5.12
OA15 [34]	GLARE 4B-4/3-0.4	45.0	140.0	5.0	5.11 & 5.12
OA9 (2002) [34]	GLARE 4B-4/3-0.4	45.0	80.0	30.0	B.2
OA6 [40]	GLARE 4B-4/3-0.4	22.5	100.0	5.0	B.5
OA7 [40]	GLARE 4B-4/3-0.4	67.5	100.0	5.0	B.5
OA13 [34]	GLARE 4B-4/3-0.4	35.0	140.0	5.0	B.6
OA21 [34]	GLARE 5-4/3-0.4	45.0	100.0	5.0	5.13 & 5.14
OA22 [34]	GLARE 5-4/3-0.4	45.0	120.0	5.0	5.13 & 5.14
OA23 [34]	GLARE 5-4/3-0.4	45.0	140.0	5.0	5.13 & 5.14
OA17 [34]	GLARE 2A-4/3-0.4	45.0	100.0	5.0	5.17
OA18 [34]	GLARE 2A-4/3-0.4	45.0	120.0	5.0	5.15
OA19 [34]	GLARE 2A-4/3-0.4	45.0	140.0	5.0	5.17
OA16 [34]	GLARE 2A-4/3-0.4	22.5	100.0	5.0	5.18
OA24 [34]	AI 4/0-0.4	22.5	100.0	5.0	5.19
OA25 [34]	AI 4/0-0.4	45.0	100.0	5.0	5.19

B.2. Initial Notch Size

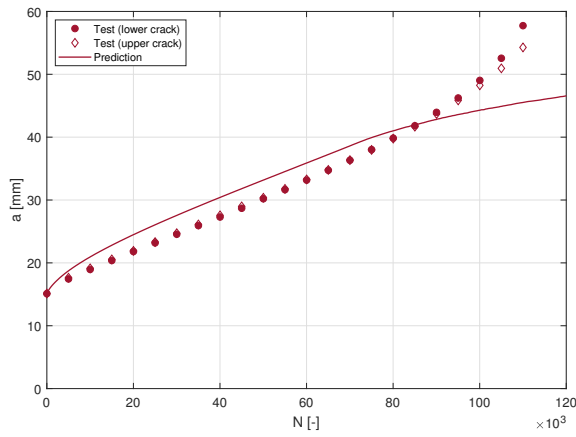


Figure B.1: Comparison between crack growth test data and crack growth prediction for GLARE 3-4/3-0.4 under $S_{max} = 100$ MPa and $R = 0.05$ at $OAA = 45^\circ$ [34]

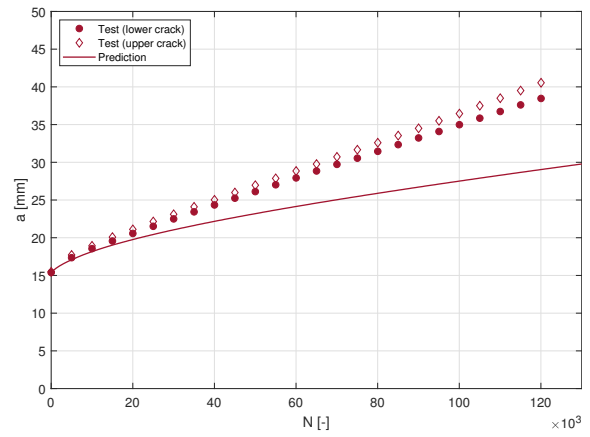


Figure B.2: Comparison between crack growth test data and crack growth prediction for GLARE 4B-4/3-0.4 under $S_{max} = 80$ MPa and $R = 0.05$ at $OAA = 45^\circ$ [34]

B.3. GLARE 3 and GLARE 4B - Other Angles

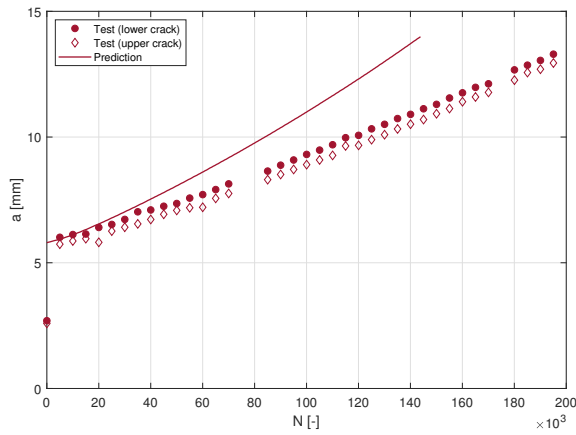


Figure B.3: Comparison between crack growth test data and crack growth prediction for GLARE 3-4/3-0.4 under $S_{max} = 100$ MPa and $R = 0.05$ at $OAA = 22.5^\circ$ [40]

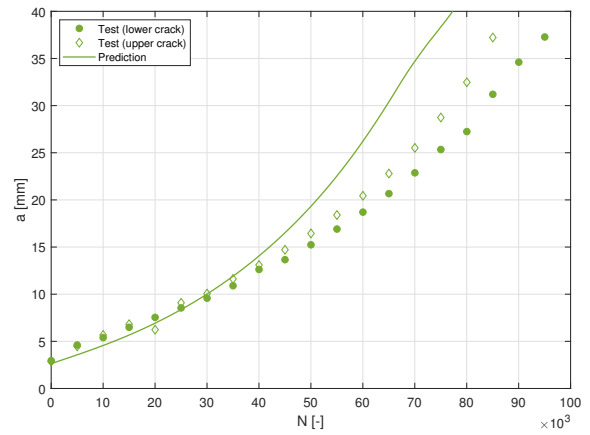


Figure B.4: Comparison between crack growth test data and crack growth prediction for GLARE 3-4/3-0.4 under $S_{max} = 140$ MPa and $R = 0.05$ at $OAA = 35^\circ$ [34]

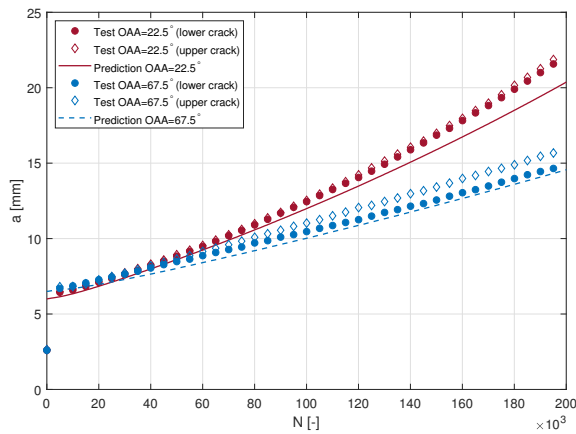


Figure B.5: Comparison between crack growth test data and crack growth prediction for GLARE 4B-4/3-0.4 under $S_{max} = 100$ MPa and $R = 0.05$ [40]

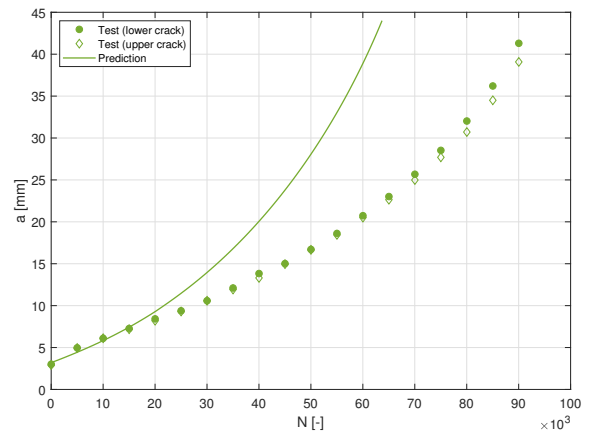
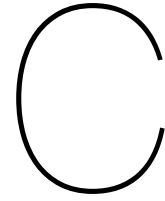


Figure B.6: Comparison between crack growth test data and crack growth prediction for GLARE 4B-4/3-0.4 under $S_{max} = 140$ MPa and $R = 0.05$ at $OAA = 35^\circ$ [34]



Metal Laminates

Running the model, as explained in Chapter 3, will underpredict the crack growth rate for metal-adhesive-metal interfaces caused by the required C_d and n_d inputs for adhesives. This creates a delamination at the interfaces, while in reality the adhesive cracks together with the metal layer [34]. As mentioned in Section 5.2.1 and 6.3.3, multiple ways exist to model this configuration and are present here by means of an example.

Four laminate configurations, in which the thicknesses of a Al-4/3-0.4 laminate are used, are simulated and listed in the first column of Table C.1 where M stands for metal, F for fibre and A for adhesive. The four different ways of modelling are compared by the number of cycles until a crack length of 12 mm is reached. Three variation on the model presented in Chapter 3 are suggested:

- Model 1: The model without any adaptation.
- Model 2: Since there occurs no delamination, the delamination parameters of the adhesive are set to zero ($C_d = n_d = 0$).
- Model 3: Almost no load is taken by the adhesive, therefore $E_{11} = E_{22} = G_{12} = 1$.
- Model 4: The bridging load at the metal-adhesive interface is set to zero.

Table C.1: Model comparison for various laminate configurations

Laminate configuration	Model 1 $N_{a=12mm}$ [-]	Model 2 $N_{a=12mm}$ [-]	Model 3 $N_{a=12mm}$ [-]	Model 4 $N_{a=12mm}$ [-]
MFMFMM	300789	300789	300789	300789
MFMMFM	207848	*2961835	176720	231759
MAMFMAM	85729	*104013	*24546	*27066
MAMAMAM	115452	*102625	20608	24093

*The inner metal plies have a smaller crack length

The results for model 1, presented in Table C.1, are inconsistent since the MAMFMAM-configuration needs fewer cycles to reach a crack length of 12 mm than when no fibre layers are present. In addition, the crack growth rate of the MAMAMAM-configuration is underpredicted when comparing it to test data. Finally, it is expected that the crack in the outer layers in the MAMFMAM-configuration grow faster than the inner ones which are bridged.

The second model shows inconsistencies in the MFMMFM and MAMAMAM-configuration. Firstly, both configurations should have an equal crack growth in all metal layers since they are bridged by an equal amount of fibre layers. Secondly, the number of cycles for the MFMMFM configuration is higher than the MFMFMM-configuration, which is unreasonable. Due to these inconsistencies this method is disregarded.

Model 3 and 4 show comparable results, although a large difference between the number of cycles of the MFMAMFM configurations exists. Tests will have to provide a definitive answer. Until then, model 4 is preferred since this model does not alter the material properties of the adhesive and simply eliminates the bridging load where none is present.